The Structure of Amorphous Semiconductor:Metal Thin-Films

by

Ann M. Edwards

Thesis submitted for the degree of

Doctor of Philosophy

University of Kent at Canterbury

November 1989

"Well, I'm shocked"

Sir Neville Mott

1988

"And all this science I don't understand,

It's just my job five days a week"

Rocket Man

1972

Abstract

A transition from semiconducting to extended state conduction may be induced in certain amorphous semiconductor:metal alloys by increasing the metal concentration above a critical limit. Descriptions of the processes involved in such a transition have generally been based around investigations on electronic properties. However, without a knowledge of the atomic-scale structure of the alloys, it is difficult to ascribe a mechanism to an observed transition.

In order to increase the understanding of such processes in semiconductor:metal systems, thin-film samples of three alloy systems (a-Si:Ni:H, a-Si:Sn:H and a-Ge:Au) have been prepared by rf co-sputtering over pertinent composition ranges, and micro-structural studies have been performed using extended X-ray absorption fine structure spectroscopy and other complementary techniques.

For low metal concentrations (<20at.%), both a-Si:Ni:H and a-Ge:Au appear to consist of two separate phases: regions of an amorphous Ni:Si or a partially crystalline Au:Ge alloy being embedded in the remaining, modified amorphous matrix provided by a-Si:H and a-Ge respectively. In contrast, Sn atoms appear to substitute randomly into the a-Si:H network. The implications of these results for the interpretation of electrical conductivity data is discussed.

Acknowledgements

Firstly I would like to thank Bob Newport for his supportive supervision during the past three years. Deep thanks also go to Mike Fairbanks for all his help and many hours of discussion. I am similarly grateful for the guidence provided by Steve Gurman during the EXAFS data analysis.

I am grateful to the Physics Department at the University of Kent and all members of the X-ray and neutron scattering team, especially Ashley, Dave, Lowel and Phil. I would particularly like to thank Geoff, Harry and Howie for their support and friendship. I would also like to acknowledge the help of Dot Finn (photography), the electronics workshop (computer maintenance) and the mechanical workshop.

I am indebted to Ted Davis for the use of equipment belonging to his group at the Physics Department, University of Leicester. I would also like to thank the members of this group for their hospitality, especially Hazel, Nik and Rasool for their help and Steve, Stuart, the mechanical and electonics workshops for their technical support. I acknowledge the help of Sue Bayliss (DSC work), Mekhaiel Manssor (conductivity measurements), George M^{c}Turk and Chris D'Lacy (Medical Sciences Department) for SEM and TEM results respectively.

Furthermore, I wish to extend my gratitude to Chris Jeynes (University of Surrey) for RBS data and to all staff at the Daresbury Laboratory, especially Wendy Myring. This research was funded by the SERC and I acknowledge the receipt of a grant from the University of Kent.

Contents

Chapter 1

Introduction

Non-crystalline semiconductors are of immense technological interest. Their freedom from the constraints of crystalline periodicity leads to the relatively low fabrication costs of large area devices in thin-film geometry, and also allows the materials to be deposited onto numerous different substrates. These useful qualities have resulted in many and varied applications of such materials, especially in the fields of energy and information technology. Here, their potential has been employed in such diverse products as solar cells, thermoelectric devices, batteries, large-area-flat-screen displays and thin-film transistors [1, 2].

Amongst the many non-crystalline semiconducting materials, the most revolutionary has undoubtedly been hydrogenated amorphous silicon (a-Si:H). The structure of this four-fold coordinated semiconductor and its group IV counterpart, a-Ge:H, has attracted numerous studies [3] which report, amongst their conclusions, that the basic a-Si/Ge framework is well characterized in terms of a tetrahedral random network (TRN).

Since the discovery that, like its crystalline analogue, a-Si:H could be doped [4],

much attention has been focussed on the properties of such alloys and, in particular, their associated electronic and optical qualities. Of great fundamental in this respect are the materials obtained from alloying a-Si:H (or a-Ge:H) with metals (M). By carefully controlling the composition of the materials formed (a-Si:M:H), it is possible to regulate the electrical conductivity and, for certain metal impurities, to induce a transition from semiconducting to metallic-type behaviour if the metal concentration is increased above a certain, critical limit. These, so-called, metal-insulator transitions (MITs) are by no means a new phenomenon. Many systems undergo such transitions as a function of temperature, pressure or composition. Mott [5] first described the metal-insulator transition and predicted that the number of impurity centres per unit volume (n_c) at which the transition would occur would be given by:

$$n_c^{\frac{1}{3}} a_H = 0.25 \tag{1}$$

where a_H is an empirical atomic radius of the impurity atom and slightly varying values have been obtained for the numerical constant.

The occurrence of a MIT in disordered systems was first suggested by Anderson [6] and explained in terms of localization of electron states. Hence, this type of MIT became known as an Anderson transition. Since this time there has been much interest in and much speculation on the exact nature of the MIT [7, 8, 9] leading to revised theories on localization and the Anderson transition [10, 11].

The advent of amorphous semiconductors, and the realization that hydrogenated group IV semiconductors could be doped with metals, encouraged a wealth of investigations devoted to the understanding of electrical transport phenomena in such systems [12, 11, 13, 14]. Of particular interest are dopants such as Mn, Fe, Co, Ni and Au which produce impurity levels deep in the intrinsic semiconductor band-gap

so that the MIT occurs at relatively high dopant concentrations (~14at.% from equation 1). Similar studies of deep level dopants in c-Si/Ge are not possible due to the low solubility of these metals in their crystalline hosts; while, in principle, such impurities can be incorporated into the amorphous network at any concentration. A review of the electronic-based experimental work on MITs in a-semiconductors until 1980 is given by Morigaki [15]. The MITs in such systems have generally been considered to be of Anderson-type as for the disorder effects created by dopants in c-semiconductors. Although disorder is inherent in a-semiconductors, the Anderson localization approach still relies on the assumption that the impurity atoms are incorporated into the structure in a random manner. If, however, clustering of metal atoms occurs, it may be more appropriate to describe the electrical conductivity of the system in terms of classical percolation theory [16].

While the structure of a-Si/Ge(:H) has been studied fairly thoroughly, the majority of experimental investigations into a-Si/Ge:M(:H) alloys have revolved round their electrical and optical properties. Yet it is clear that the way in which dopants are incorporated into the a-semiconducting matrix is of vital importance to the description of the electronic processes occurring in the alloy.

In this thesis, extended X-ray absorption fine structure spectroscopy and supporting techniques have been used to examine the structure of three amorphous semiconductor:metal systems over the composition range where a MIT may be expected to occur according to equation 1. The three metals chosen for investigation are very different in nature to enable comparison:

(a) Ni — a transition metal with an incomplete d-shell

(b) Sn — a group IV metal

(c) Au — a transition metal with a full d-shell.

All samples were prepared in the form of thin-films by rf co-sputtering in order to be characteristic of device quality materials. Electrical conductivity measurements are being extended in a parallel study at the University of Leicester. It is hoped that the structural work presented here will be able to identify the way in which the different impurity atoms are included in the TRN of the semiconducting host and subsequently be used to help clarify the processes describing the conductivity and MITs in such systems.

Chapter 2

Amorphous Materials

Despite the fact that people have been using amorphous materials in the form of a variety of so-called 'glasses' for a wide range of purposes throughout history, it is only relatively recently that detailed scientific studies have begun to emerge [17].

As with most science, interest escalated with the realization that some of these materials possess important technological properties and hence industrial potential, the consequent research resulting in a rapid increase in the understanding of such systems over the past three decades. Today, amorphous materials find an even wider scale of use, notably in the field of amorphous semiconductors and their alloys.

2.1 The Structure of Amorphous Materials

The atomic-scale structure of amorphous solids is one of the most important fundamental properties of this set of non-crystalline materials. Not only is it the basis by which such solids are characterized, but it is also directly responsible for many of the useful properties exhibited.

Consider the atomic arrangement of a crystal, such as the covalently bonded example represented in figure 2.1(a); the dots denote the equilibrium positions of atoms and it can be seen that all bond-lengths and bond-angles between these positions are exactly equal. This regular, periodic structure is characteristic of all crystalline solids, though real crystals may show departures from this *perfect* case due to defects.

Figure 2.1(c) represents a perfect gas, with the dots denoting a snap-shot of one configuration of instantaneous atomic positions. This is a truly random distribution of atoms and there is no correlation between atomic positions; though in a real gas interatomic potentials and atomic size give rise to small deviations from genuine randomness.

Non-crystalline materials (including both liquids and amorphous solids) are characterized by structures somewhere between these two extremes. In the case of the liquid, atoms can undergo translational motion as in the gas, but movement is constrained by the potentials of neighbouring atoms situated at similar interatomic distances to the crystalline case. For an amorphous solid, the nearest-neighbour distances are also comparable to analogous crystalline materials and, like the crystal case, atoms oscillate about equilibrium positions and cannot undergo the translational motion associated with the fluid state. However, amorphous solids are distinguishable from their crystalline counterparts by the absence of long-range order (LRO). Figure 2.1(b) shows a schematic representation of a covalently bonded amorphous solid and

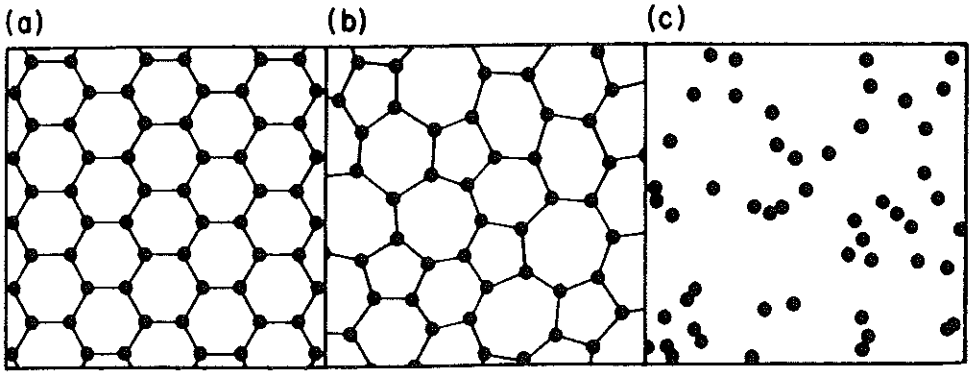

Figure 2.1: Schematic representation of the atomic arrangements in (a) a crystalline solid, (b) an amorphous solid and (c) a gas [18]

it is evident at a glance that despite the lack of LRO, there remains a high degree of local correlation. The type and degree of this short-range order (SRO) depends on the nature of the chemical bonding present in the system. In the example of covalently-bonded materials such as amorphous silicon and germanium (written a-Si and a-Ge), both near-neighbour interatomic distances and bond-angles are similar to those of their crystalline counterparts.

Information about the short range order of amorphous solids, derived from experiments such as X-ray, electron and neutron diffraction or extended X-ray absorption fine structure (as in this study) has led to the determination of various structural models, the most commonly used being:

(a) continuous random network (covalent bonding)

(b) random close packing (metallic, ionic, van der Waals bonding)

(c) random coil model (polymers).

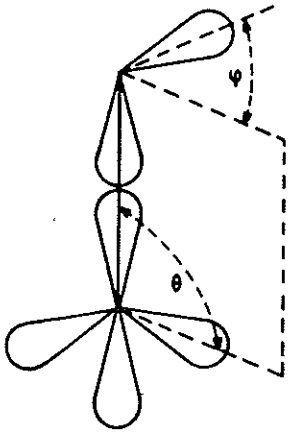

Figure 2.2: Definition of bond (θ) and dihedral (φ) angles [19]

Although all three include the term *random* in their names, they are not truly random as in the case of a perfect gas, but do show statistical distributions of quantities such as interatomic distances and bond-angles that would, in the crystal be represented by fixed values.

Amorphous solids having predominantly covalent bonding, such as a-Si and a-Ge, are best described by the 'continuous random network' (CRN) model [17]. In this model, nearest-neighbour bondlengths and coordination numbers are well defined (and similar to the crystal analogue), but the CRN achieves non-crystallinity by allowing some degree of near-neighbour bond-angle distortion and an even wider variation in the relative angle between second nearest neighbours. This so-called dihedral angle represents the relative orientation of the fundamental polyhedra formed by nearest-neighbours (see figure 2.2) and it is found that for most CRNs certain angles are favoured.

Simple metallic glasses such as a-Bi and a-Ga favour the random close packing (or dense random packing) model [20]. As implied by the name, this model is akin to the close-packed structures (fcc and hcp) of crystalline metals but with some degree of topological disorder producing non-crystallinity (randomness) while maintaining high density.

Polymeric organic glasses such as polystyrene are most satisfactorily described by the random coil model. In organic glasses, bulky sidegroups prevent the formation of small rings leading to polymer chains as the preferred configuration. Each chain can adopt a random coil configuration, most easily visualized as a 3-D random walk [21]. This amorphous model consists of many of these coils considerably interwoven to produce a homogeneous structure.

2.2 The Formation of Amorphous Materials

Formation of an amorphous solid is an almost universal ability of condensible matter, but the conditions necessary are not always easily attainable. Although the preparation of amorphous solids does not necessitate starting from the liquid state (see section 2.3), quenching from the melt provides an easily understandable description of their formation. When a liquid is cooled it may solidify in two ways:

1. discontinuously to a crystalline solid

2. continuously to an amorphous solid.

If we consider this in terms of the volume of the material and refer to figure 2.3, we see that crystallization takes place almost instantaneously at the melting temperature (T_m). This heterogeneous process, involving the sudden nucleation and

rapid growth of crystallites, results in a sharp decrease in volume at T_m; while for the homogeneous process of glass formation the liquid phase becomes supercooled before reaching the glass transition temperature (T_g), where the gradient of the V(T) plot changes to acquire the small slope characteristic of the low thermal expansion of a solid. The type of solidification process occurring depends on the quenching rate, though the specific rate needed to form an amorphous solid varies with the material. In general, crystallization will occur at low cooling rates; but, if the rate is sufficiently high to preclude crystal nucleation and growth, T_m will be bypassed without crystallization to form an amorphous material. Amorphous materials that can be prepared by quenching the melt in this way are conventionally known as 'glasses', though a variety of techniques exist for the preparation of amorphous solids in general.

2.3 Preparation of Amorphous Materials

Amorphous materials may be prepared by a great number of methods, the most common of which are outlined briefly here. The method of preparation is of prime importance since many properties of non-crystalline materials are dependent on it (see for example [23]).

(a) Quenching Techniques

A variety of quenching techniques exist, giving rise to a wide range of cooling rates. For materials with a high glass-forming tendency (such as SiO_2 or As_2S_3) the melt can simply be allowed to cool by removing the heat, resulting in cooling rates of 10^{-4} - $10^{-1}Ks^{-1}$. Cooling rates of 10^{1} - $10^{2}Ks^{-1}$ can be achieved by quenching

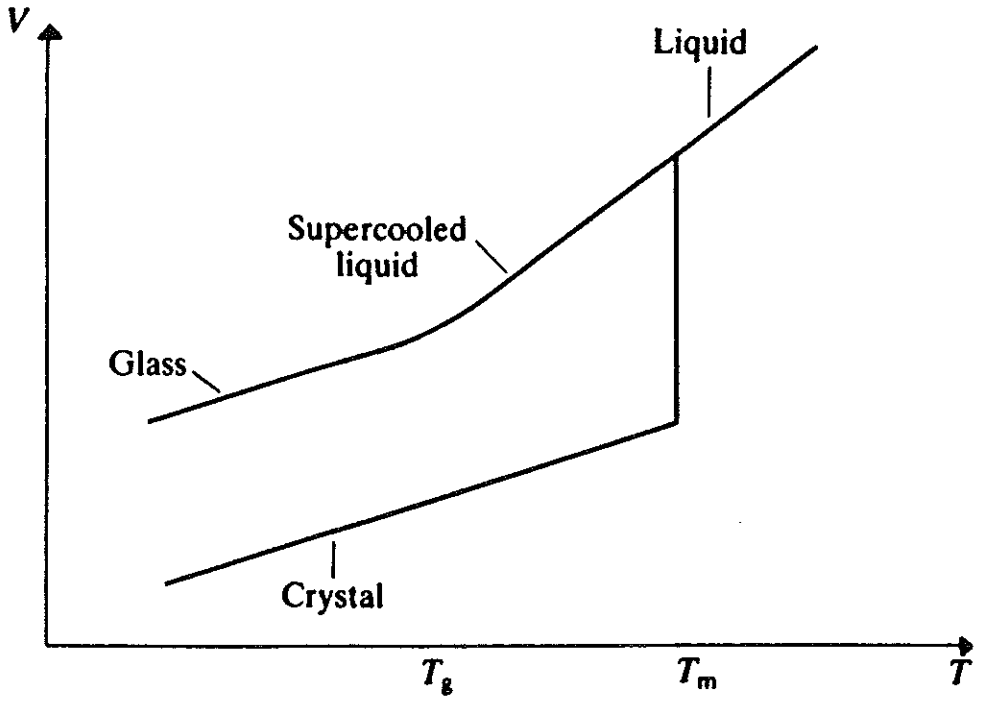

Figure 2.3: Schematic volume versus temperature plot illustrating the formation of a glass or crystalline material [22]

the melt in ice-water. The higher rates necessary for metallic glasses (typically 10^5 - $10^8 Ks^{-1}$) can be obtained by 'splat-quenching' techniques such as squashing a liquid metal droplet between a hammer and anvil or melt-spinning the metal/alloy off a cooled, rapidly rotating cylinder. Extremely high cooling rates (estimated at 10^{10} - $10^{12} Ks^{-1}$) are available by 'laser glazing' — melting a tiny volume on a crystal surface with an intense laser pulse and allowing it to be rapidly quenched by the surrounding crystal.

(b) Physical Vapour Condensation Techniques

These techniques involve atoms from a vapour condensing under such conditions that their thermal energy is extracted before they can migrate to their crystalline configuration. The source material can be vapourised in a vacuum by thermal evaporation, electron-beam or ion bombardment and condenses to form a thin-film. The relatively high cooling rates produced (up to $\sim 10^9 Ks^{-1}$) are sufficient for the formation of amorphous silicon, germanium, iron and cobalt; the main disadvantage of the technique being the inability to incorporate reactive gases such as hydrogen.

(c) Chemical Vapour Deposition Techniques

Chemical vapour deposition (CVD) involves constituents of the vapour phase reacting to form a solid film at some surface. CVD reactor systems have been constructed in a variety of configurations but all must transport, meter and time the diluent and reactant gases, provide and control heat to the reaction site (*i.e.* the substrate material being coated) and remove the by-product exhaust gases from the

deposition zone. Deposition conditions should be such that the reaction occurs only at, or near, the substrate surface and not in the gaseous phase.

CVD can be used for depositing a large variety of elements and compounds, including metallo-organics, at relatively low temperatures. Amorphous or crystalline layers can be deposited with a wide range of accurately controllable compositions and high purity.

(d) Glow-Discharge Techniques

This technique relies on the production of a plasma (or glow-discharge) in a low pressure gas ($\leq$0.1mbar) and the chemical decomposition of the gas itself, leading to deposition of a thin-film on a solid support. The decomposition of gases such as silane (SiH_4) to produce a-Si:H by this process have increased its use, and the principles of glow-discharge are incorporated into many other methods of film deposition.

Further details on preparation techniques for amorphous materials can be found elsewhere (see for example [18, 22, 19, 24]).

(e) Sputtering Techniques

Like glow-discharge, sputtering also relies on the production of a plasma, but the low-pressure gas is usually inert and its ions are used to eject material from a target which can then be condensed elsewhere. There are several methods of film deposition that use the principle of sputtering, and these will be summarized in Chapter 4, where the particular technique used in this study will be described in detail.

2.4 Thin-Film Technology

Amorphous solids are frequently encountered in the form of either bulk glasses or thin-films. A solid material is classified as being in *thin-film* form when it is created *ab initio* as a thin layer on a solid supporting substrate, even though films formed in this way may be tens of microns thick physically. This condensation of atomic, molecular or ionic species may result from a physical or chemical deposition process as outlined above and the hyphenated notation, thin-films, will be adopted throughout this thesis in referring to films synthesized in this manner. It should be noted that, films prepared by direct application of a material onto a substrate are called *thick films*, irrespective of their thickness and do not yield the characteristic properties provided by true thin-films; while any self-supporting materials of small physical thickness may be referred to as thin films (with no hyphenation).

The physical, electronic and optical properties of thin-films are often quite different from those of the bulk material. These deviations arise because of the small thickness, large surface-to-volume ratio and unique physical structure of thin-films, the latter being a direct consequence of the growth process (outlined in section 4.1.1). Some of the phenomena arising as a direct result of very small thicknesses are optical interference, electronic tunneling through an insulating layer and high resistivity. The high surface-to-volume ratio and microstructure can influence gas adsorption, diffusion and optical absorption. Properties such as these, together with the physical compactness and opportunities for electronic integration offered by thin-films have given them a high technological importance.

Chapter 3

Electronic Properties

Although polycrystalline semiconductors, and their associated useful electronic properties, had been acknowledged and researched for more than a century, it was not until the 1950's that certain chalcogenide glasses (amorphous materials containing one or more of the the chalcogen elements of group VI of the periodic table S, Se, Te) were discovered to behave like semiconductors also [25]. Although the electrical conductivity of the chalcogenide glasses could not be altered by doping, the later discovery that glow-discharge deposited a-Si:H *could* be doped both p-type and n-type [4] created enormous interest in amorphous group IV semiconductors.

Polycrystalline semiconductors are composed of grains, each containing a periodic array of atoms and the electronic theory of such materials is based on the band structure arising from this pseudo-long-range order. However, such theories do not hold for amorphous materials which, by definition, lack long-range order and hence new theories needed to be put forward to explain experimental observations.

3.1 Review of Electronic Properties of Crystalline Materials

Before approaching the case of amorphous materials, it is useful to review briefly the theories for electronic processes in crystalline materials in order that fundamental ideas and terminology may be introduced and comparisons between the two may be made later.

For crystalline materials, the characteristic long-range order results in a periodic potential and electron states can be written as plane waves which extend throughout the crystal with the Bloch form:

$$\psi_{\mathrm{k}}(\mathrm{r}) = \exp(i\mathrm{k}.\mathrm{r})u_{\mathrm{k}}(\mathrm{r}) \tag{2}$$

where $u_{\mathrm{k}}(\mathrm{r})$ has the periodicity of the Bravais lattice so that $u_{\mathrm{k}}(\mathrm{r}+\mathrm{R}) = u_{\mathrm{k}}(\mathrm{r})$ for all Bravais lattice vectors R, and k represents the allowed wavevectors of the electrons. These wavevector values represent quantum numbers for the electrons in the reciprocal lattice (k-space).

The energy of a free electron is considerably altered by the periodic potential of the crystal and the allowed energies of the electrons can be represented in terms of a 'band structure' in k-space. Each band can accomodate 2N electrons (where N is the number of unit cells per unit volume and the factor 2 arises from the spin degeneracy) and may be separated from other bands by a 'band-gap'.

The Fermi energy (E_f) of a system is the highest occupied electronic level *i.e.* the minimum energy required to contain all occupied electronic levels. At absolute zero (T=0K) this is known as the Fermi level. For a crystalline material in which

the number of electrons is sufficient to populate a non-integral number of bands, the Fermi energy will lie in the middle of a band. In order for electronic conduction to take place, some electrons must be able to make transitions to unoccupied states of slightly higher energy in the band, the increased energy being gained through application of an electric field. Such materials exhibit metallic electrical conduction. If, however, the highest occupied band is completely full, an electron must gain enough energy to raise it into the next band *i.e.* across the band-gap; so for small field stengths the substance is an insulator.

In between these two extremes lie materials for which the highest occupied band is full at absolute zero, but at non-zero temperatures a few electrons have sufficient energy to be thermally excited across a relatively small band-gap into the lowest 'unoccupied' band (the conduction band) leaving holes in the highest 'occupied' band (the valence band). When a field is applied, this gives a small electrical conductivity whose magnitude depends on the width of the band-gap and increases with increasing temperature. This 'intrinsic conductivity' is characteristic of pure semiconductors such as c-Si or c-Ge.

The electronic properties of a crystalline semiconductor can be modified by defects in the lattice such as the presence of impurity or dopant atoms. In very low concentrations such dopants produce discrete, localized energy levels; an electron being regarded as localized if its mean free path (L) is shorter than the atomic spacing (a) so it is loosely bound to the atom. However, at slightly higher dopant densities (*e.g.* one atom of As in 10^5 atoms of Ge or Si), these levels spread into narrow bands as the impurity atoms become close enough for their wavefunctions to overlap; and when wavefunction overlap is sufficient, the bands will become delocalized. As the band broadens with increasing dopant concentration, it will eventually merge with the

nearest intrinsic extended band, resulting in extended state conduction on application of a field. However, due to the low solubility of many dopants in c-Si/Ge, such MITs can only be observed for systems in which they occur at low dopant concentrations.

The discrete levels are important when they lie in the energy-gap as illustrated in figure 3.1. Impurity states that lie deep in the band-gap, *i.e.* just above the valence band, are known as acceptor levels since above 0K electrons may be excited from the valence band into such a level, leaving holes in the extended band and thus increasing electrical conduction. In tetrahedrally-bonded crystalline semiconductors such as Si or Ge, this p-type conduction (*i.e.* by positive holes) is commonly brought about by doping with trivalent atoms such as boron. Similarly, impurities such as phosphorous (valence 5) introduce shallow states (*i.e.* just below the conduction band) in the band-gaps of c-Si. If temperatures are high enough to excite electrons from such donor levels into the empty extended state, then these negative charges can conduct and the material is known as an n-type semiconductor. This 'extrinsic conductivity' may be simultaneously present with the intrinsic conductivity of the pure host material and may often dominate it. However, at temperatures high enough to fully ionize all donor impurity atoms, or to fill all acceptor levels, this extrinsic conductivity will become constant.

Both electrons and holes contribute to the conductivity (σ) which is given by the formula:

$$\sigma = |e|(n_e\mu_e + n_h\mu_h) \tag{3}$$

where $n_{e/h}$ = number of electrons or holes per unit volume

$\mu_{e/h}$ =associated electron and hole mobilities

(both taken as positive numbers).

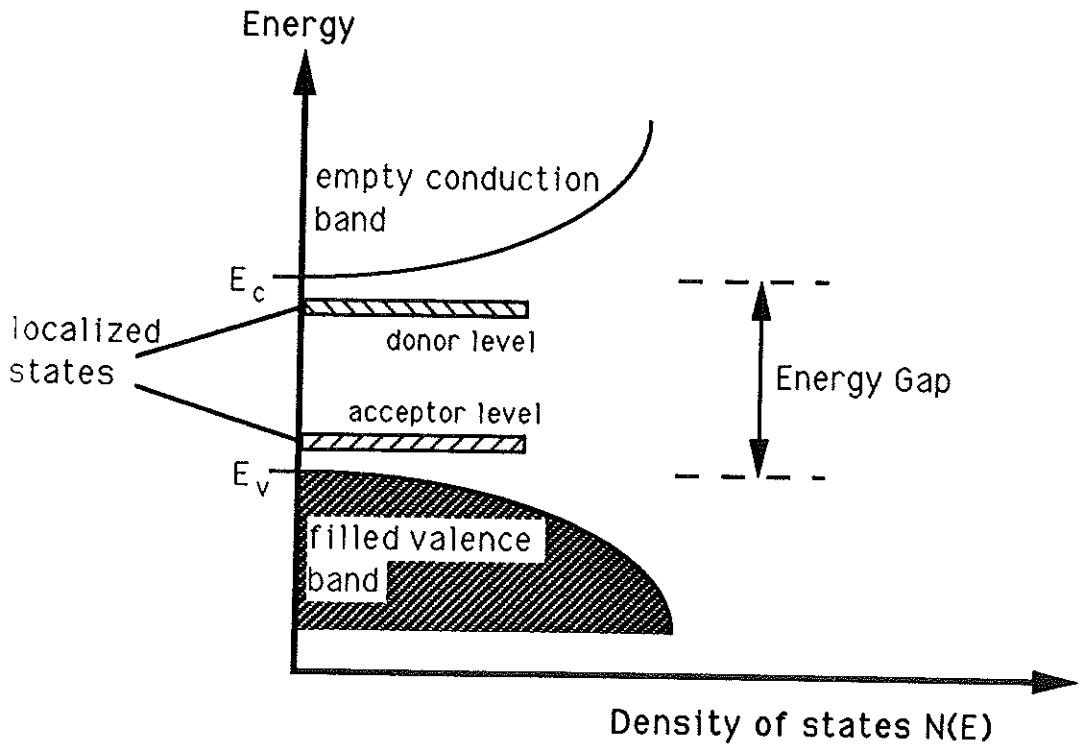

Figure 3.1: Schematic density of states diagram for a crystalline semiconductor showing discrete donor and acceptor levels due to impurities

For intrinsic semiconductors (or doped semiconductors at high temperatures where the conductivity is dominated by the intrinsic electrons) $n_e = n_h$ so that $\sigma = |e|n\mu$ where n and μ now represent the total number of carriers per unit volume and the combined mobility respectively.

3.2 Effects of Disorder on Electronic Properties

Consider now an amorphous material whose structure does not involve the characteristic periodicity of the crystal. Without such long-range order, k is no longer a good quantum number for the electrons and they cannot be represented as Bloch states. This suggests that band theory is inappropriate for amorphous materials, but the fact that window-glass is transparent to visible light is evidence that a band-gap does exist for this amorphous material even though conventional (crystalline) solid-state physics cannot explain its origins.

In 1971, Weaire and Thorpe [26] showed that if short-range interactions between electrons were dominant, then it is the local atomic ordering which mainly determines the electronic density of states, N(E); hence the density of states (number of states per unit volume per unit energy) is still a valid description for amorphous materials. This led to the construction of various model Hamiltonians for the electronic interactions which correctly predicted that, providing that the interactions are of a certain magnitude, a band-gap *is* expected for an *ideal* tetrahedrally-coordinated amorphous solid such as the semiconductors a-Si and a-Ge. (See figure 3.2).

Comparing figures 3.1 and 3.2b it can be seen that the sharp edges of the band-gap in the crystalline case are turned into smeared-out band-tails in the glass. This is a direct result of the lack of long-range order in the a-semiconductor; but of greater interest is the effect of disorder on the nature of such electron states. As indicated

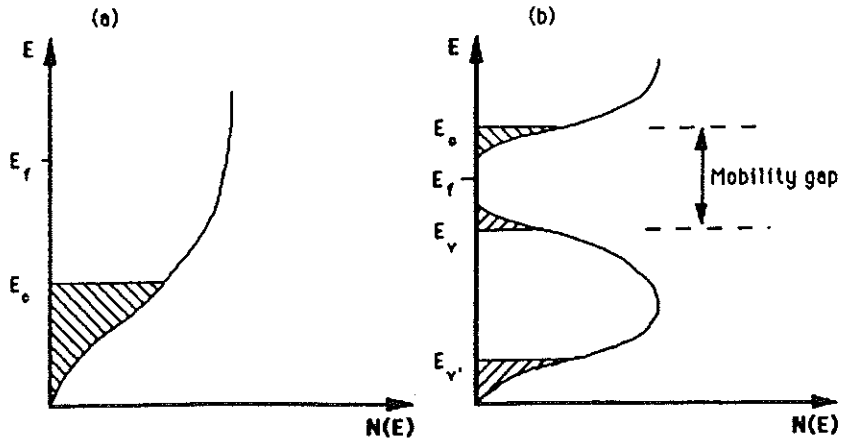

Figure 3.2: Schematic density of states diagram showing the Fermi energy at 0K in (a) an amorphous metal and (b) an amorphous insulator or intrinsic semiconductor. Localized states are shaded

in figure 3.2, electrons in the amorphous material may become confined in space *i.e.* localized; this occurrence is more likely in the band-tails since these arise, in general, from the most distorted sites and so these electrons experience the most disordered potentials.

The first criterion for localization was proposed by Anderson (1958) [6], namely that a wavefunction is localized if it is confined to a small region of space and has a probability $\propto \exp(-2\alpha r)$ (where α = inverse localization length) of remaining at a distance r within the volume as time $\rightarrow \infty$. This is known as Anderson localization. If there is a finite chance of diffusion at T=0K, then the state is delocalized or extended.

The concept of localized wavefunctions had been realized in connection with discrete impurity levels in crystalline semiconductors, but the Anderson model introduced the possibility of all the states in a band being localized.

Figure 3.3 shows a schematic representation of how such an Anderson transition (extended $\leftrightarrow$ localized states) takes place as disorder is increased in the system. In

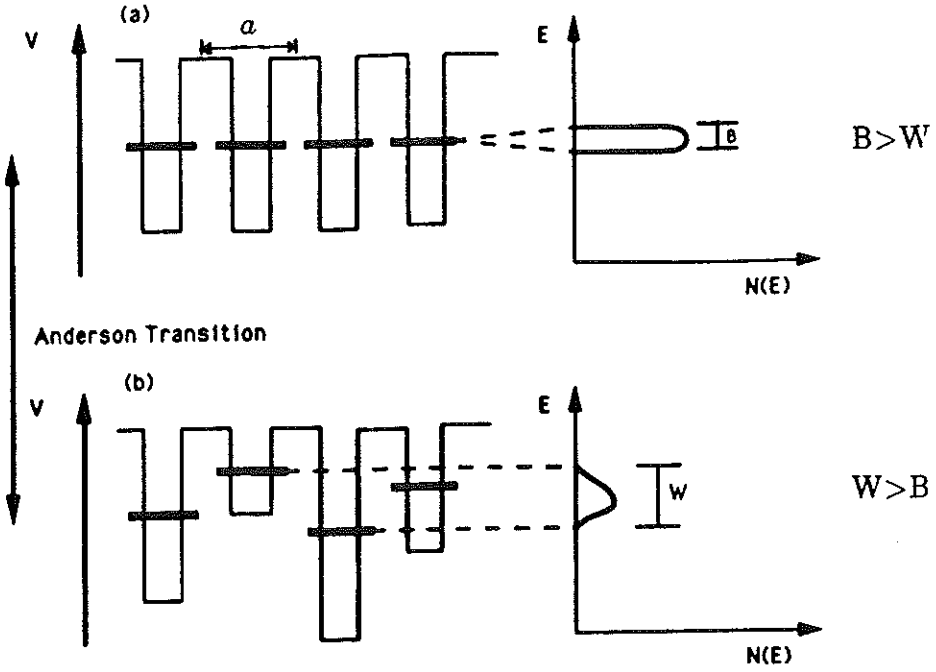

Figure 3.3: Schematic representation of potential wells and density of states for (a) crystalline lattice and (b) disordered lattice. When the width W of the disorder exceeds the overlap bandwidth B, an Anderson transition occurs.

the crystal case, (a), the periodic potentials give rise to a narrow band of levels of bandwidth B. The introduction of topological disorder, (b), creates random variations in the potentials; the width of this distribution being denoted by W. The value of the dimensionless 'disorder parameter', W/B, is the crucial factor in determining whether states are localized or extended, and the higher its value the more states are localized until at a critical value *all* states in the valence electron band become localized.

The electron wavefunctions in the Anderson model are illustrated schematically

in figure 3.4. The value of the electron mean free path (L) is reduced with increasing disorder until it becomes significantly shorter than the interatomic distance (a) and thus the wavefunction becomes localized on the atom *i.e.* confined in space.

The introduction of such a random potential by any means will create *some* localized states in the band-tails and these are separated from non-localized states in the same band by mobility edges (E_c, E_v and $E_{v'}$ in figure 3.2); the crystalline band-gap is effectively replaced by a mobility-gap. As disorder increases, E_v and $E_{v'}$ move towards each other until the entire band becomes Anderson localized at a critical disorder. Moving the Fermi energy through E_c or E_v by some means also produces a localization $\leftrightarrow$ delocalization Anderson transition (sometimes referred to as a metal-to-non-metal or metal-insulator transition, MIT). This is possible via changes in composition, pressure *etc.*

Using the concept of localized states in the band-tails, band structure models varying in the extent of this tailing were proposed for amorphous semiconductors.

The Cohen-Fritzsche-Ovshinsky model [28] assumes that tail states from the conduction and valence bands overlap in a continuous distribution (see figure 3.5a). The model was originally proposed for multicomponent chalcogenide glasses in which the authors suggested that the disorder was sufficiently great to cause an appreciable density of states in the mid-gap. The major objection to the CFO model was the experimental observation of the transparency of a-semiconductors in certain spectral regions. The localized region between the mobility edges is referred to as a pseudo-gap in this model, since the density of states does not fall to zero.

Conversely, the Davis-Mott model [29] proposed that band-tails should be narrow. Furthermore, their model distinguished between localized states in the band-tails (caused by lack of long-range order) and others near the middle of the mobility-gap

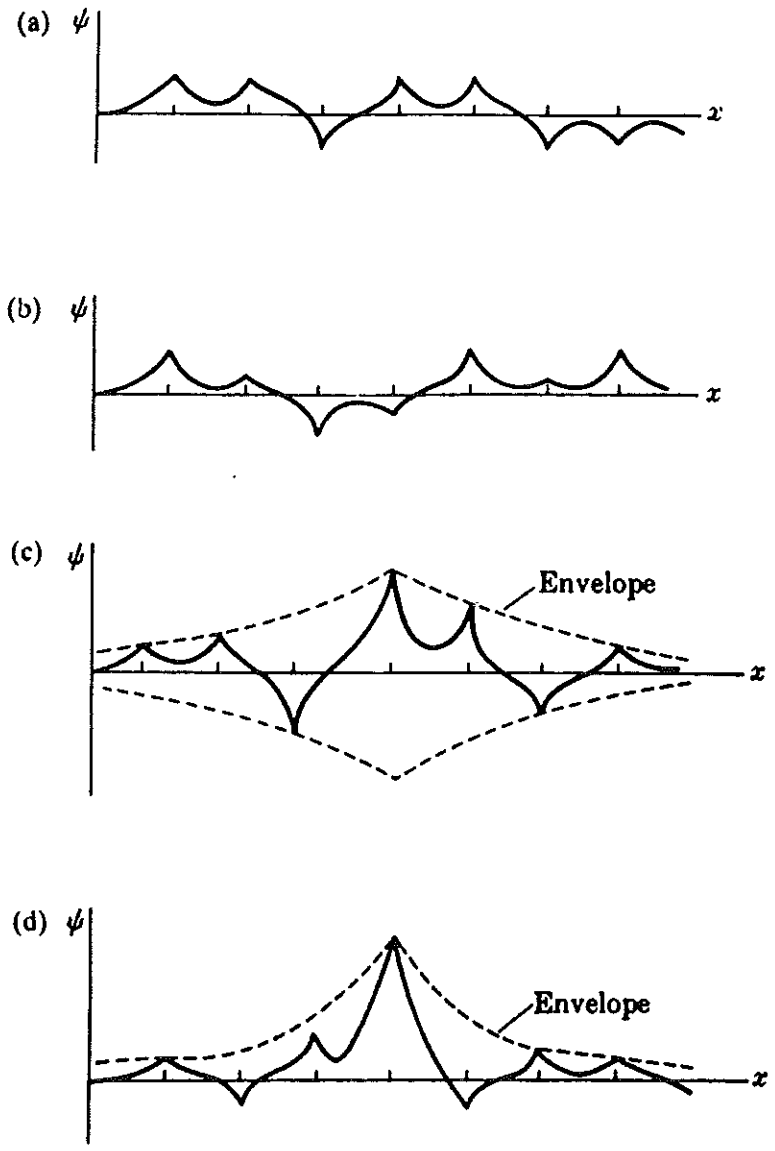

Figure 3.4: Schematic illustration of the form of the electron wavefunction in the Anderson model [27] (a) when L $\sim$ *a*, (b) when states are just non-localized (E > E_c), (c) when states are just localized (E < E_c) and (d) strong localization

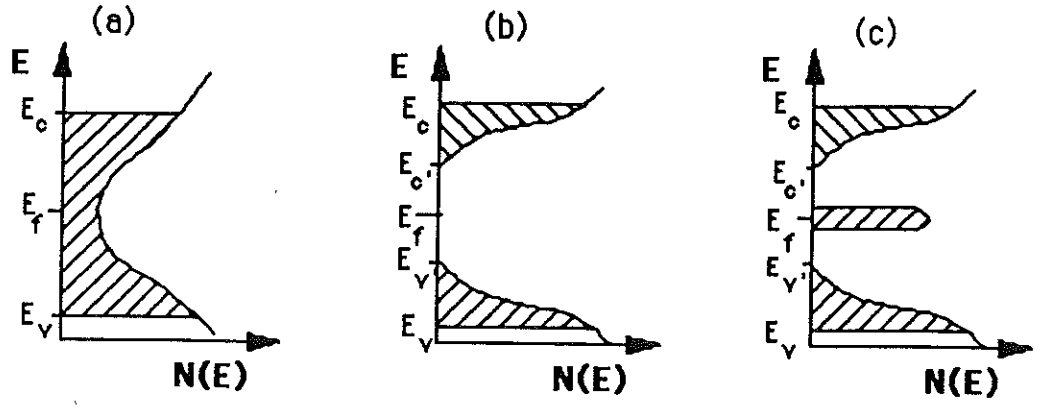

Figure 3.5: Schematic density of states diagrams for amorphous semiconductors. (a) the CFO model, (b) the Davis-Mott model showing no defects and (c) the Davis-Mott model with defects near the centre of the gap.

due to intrinsic defects in the random network (see figure 3.5b and c).

3.3 Effects of Defects on Electronic Properties of Covalently Bonded Amorphous Semiconductors

An *ideal* glass, in terms of the continuous random network (CRN) model for covalently-bonded amorphous structures (section 2.1) is defined as one having no bonding defects and no impurities. Although many of the defects common to c-solids *e.g.* dislocations, grain boundaries, vacancies and interstitials are less likely to be found in real, covalently-bonded, intrinsic a-semiconductors due to the absence of periodicity,

chemical defects such as undercoordinated or overcoordinated atoms are inherent.

The most common form of defect intrinsic to tetrahedrally-bonded a-semiconductors such as a-Si is the dangling bond *i.e.* an unsatisfied bond. Although, in theory, such point defects can be eliminated by structural rearrangement, in practice overconstrained networks with an average coordination above 2.4 prefer to relieve strain by dangling bond formation [30]. Such native defects produce states within the gap, the level being broadened into a band by disorder as indicated in figure 3.5c.

The position of such a defect state can be explained in terms of a molecular orbital picture (figure 3.6a). Consider a tetrahedral semiconductor such as a-Si or a-Ge, with an atomic electronic configuration s^2p^2. The atomic levels hybridize to form four equivalent sp^3 molecular hybrids, each of which may overlap with a similar orbital on a neighbouring atom to form a bonding and an antibonding orbital separated by a band-gap. Hence, a dangling bond containing a single electron will be effectively equivalent to one of the sp^3 hybrids and will therefore have a similar energy level *i.e.* near the middle of the gap.

A dangling bond usually contains one electron and is 'donor-like' *i.e.* electrically neutral when occupied. However, it is amphoteric in nature and when another electron is placed in the state it becomes 'acceptor-like' *i.e.* neutral when empty. In this case the mutual electric repulsion will increase the energy of the dangling bond state by the correlation energy (U) as shown in figure 3.6b.

The presence of such defect states 'pins' the Fermi energy (E_f) near the mid-gap. If the two defect bands are present, E_f will lie in the gap between them or in the region of their overlap. Although in this case E_f lies in a band, the states are localized so the material remains a semiconductor and not a metallic conductor.

Since semiconductors such as a-Si and a-Ge cannot be formed as bulk glasses, they

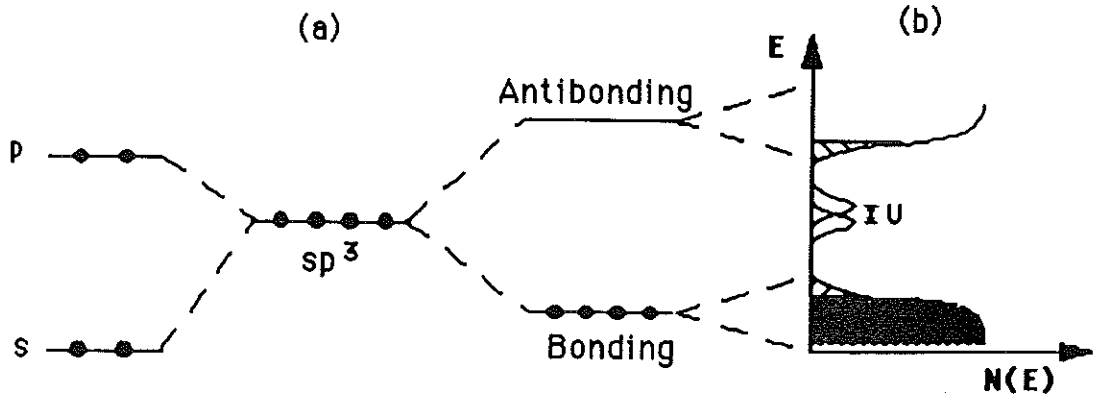

Figure 3.6: (a) Schematic representation of the electronic structure of a tetrahedrally bonded semiconductor and (b) corresponding density of states diagram, also showing single and double occupancy dangling bond states.

are usually prepared by rapid quenching from the vapour phase *e.g.* glow-discharge deposition or sputtering to form thin-films. Such deposition processes introduce other native defects in the form of microscopic voids. If two nearby dangling bonds project into such a void, they may reconstruct to form a weak Si–Si covalent bond. These weak bonds contribute to the tails near E_v and E_c. Dangling bonds that cannot reconstruct can be detected by electron spin resonance (ESR), and though annealing can reduce the density of states in the gap (and the extent of band-tailing) by allowing reconstruction and rearrangement, it remains high enough to pin E_f in the gap. Therefore E_f is not moved significantly by the addition of impurities which will simply donate or accept electrons to or from the defect states and hence, intrinsic semiconductors such as a-Si and a-Ge cannot be doped.

Although all such intrinsic non-bonding electrons cannot be paired together to

form the ideal CRN, they *can* be passified by other atoms such as oxygen, nitrogen, fluorine and, more commonly, hydrogen. In hydrogenated amorphous silicon (a-Si:H), hydrogen atoms form strong covalent bonds with the non-bonding electrons and effectively saturate all dangling bonds. In fact, the strength of the Si–H bond may cause weak Si–Si bonds to break up and acquire hydrogen. This fact, together with the knowledge that some of the reactive gas may end up trapped in microvoids during deposition, accounts for the fact that a-Si:H contains a larger percentage of H atoms than pure a-Si has dangling bonds. Since the Si–H bonding states lie in the valence band, hydrogenation removes defect states from the band-gap rendering the material dopable.

In the absence of the large density of states in the gap native to the host solid, the impurity states are able to move the Fermi energy, and in particular to move it close to E_v or E_c allowing p-type or n-type extrinsic semiconduction. If E_f is shifted enough to move it into a delocalized band, then extended state conduction will result. This is analogous to the Anderson metal-insulator transition mentioned in 3.2, the disordered potential being provided by the impurity atoms. Hence, hydrogenated amorphous silicon or germanium can be doped in a similar way to the crystalline case, but higher dopant concentrations can be achieved since, in principle, any kind of impurity can be incorporated into the amorphous host at any content.

3.4 Electron Transport

Since the fundamentally important, and technologically most useful, properties of amorphous semiconductors and their alloys involve the electronic properties of such materials, it is these that have received the most attention in terms of experimental research and theoretical explanations. One of the simplest and most informative

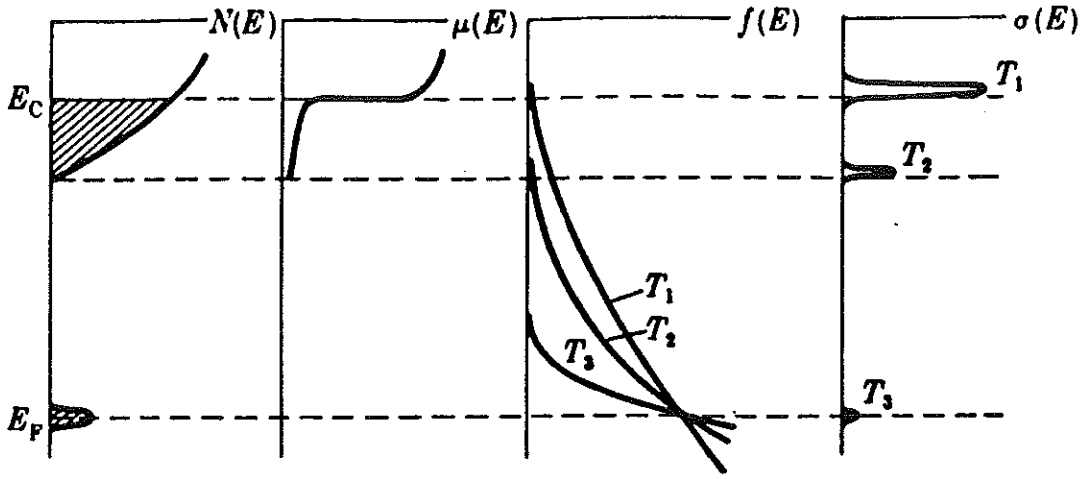

Figure 3.7: Schematic illustration of the effect of temperature ($T_1 < T_2 < T_3$) on the mode of conduction [27]

electrical properties to study is the dc electrical conductivity (σ) of these solids. For states above E_f in *ideal* a-semiconductors at a finite temperature (T), the *total* conductivity is obtained as an integral over all available energy states:

$$\sigma = -e \int_0^\infty N(E)\mu(E)k_B T \frac{\partial f(E)}{\partial E} dE \qquad (4)$$

cf. equation 3.

where N(E) = density of states at energy E

μ(E) = mobility of a carrier at energy E

f(E) = Fermi-Dirac function:

$$f(E) = \frac{1}{1 + \exp(\frac{E - E_f}{k_B T})} \qquad (5)$$

Figure 3.7 shows the variation of these parameters above E_f.

The Davis-Mott model (figure 3.5b and c) leads to several possible conduction processes that may contribute to the overall conductivity; their relative contributions predominating in different temperature regions.

(a) Extended State Conduction

An extended state is defined as one which is not localized. The associated conduction process is often thought of in terms of the degenerate extended state conductivity occurring in metals; however, semiconductors can also exhibit extended state conduction. With increasing temperature, some electrons will be thermally excited into the extended state above the conduction band mobility edge (E_c). These carriers contribute to the conductivity in a similar way to that of free carriers in a metal, their motion being impeded by scattering and, in the case of a-semiconductors, trapping and release by localized states. The main limitation of extended state transport in a-semiconductors being (just as for c-semiconductors) the small and temperature-sensitive carrier concentration as opposed to the large and temperature-insensitive carrier concentration of a metal. However, at high temperatures (*i.e.* above room temperature) a few such carriers in the extended states will provide the dominant conduction path.

Using the relationship from equation 5:

$$\frac{\partial f(E)}{\partial E} = -f(E)\frac{[1-f(E)]}{k_B T} \tag{6}$$

equation 4 can be rewritten:

$$\sigma = e\int_0^\infty N(E)\mu(E)f(E)[1-f(E)]dE \tag{7}$$

where f(E) represents the probability of an electron being in the conduction band and [1 - f(E)] the probability of a hole being in the valence band. For a full band, f(E) =1 and therefore σ =0.

Assuming sharp mobility edges at E_v and E_c, the Davis-Mott model proposes that E_f is situated near the middle of the gap and sufficiently far away from E_v and E_c that Boltzmann statistics can be used to describe the occupancy of states:

$$f(E)[1 - f(E)] \simeq \exp(-\frac{E - E_f}{k_B T}) \tag{8}$$

Assuming a constant mobility, substituting equation 8 into equation 7 and integrating gives (for the case of electrons excited above E_c):

$$\sigma_{ext} = \sigma_{0ext} \exp(-\frac{E_c - E_f}{k_B T}) \tag{9}$$

where $\sigma_{0ext} = eN(E_c)\mu_e k_B T$; μ_e being the average electron mobility in the conduction band, the mobility in the gap being taken as zero.

If the dominant conduction process is via holes in the valence band, the corresponding formula would be:

$$\sigma_{ext} = eN(E_v)\mu_h k_B T \exp(-\frac{E_f - E_v}{k_B T}) \tag{10}$$

Hence, extended state conduction is a thermally activated process since $\mu \propto 1/T$, and if $(E_f - E_v)$ is a linear function of T over the temperature range measured, then a plot of $\ln \sigma$ against $1/T$ will produce a straight line whose slope yields the activation energy for conduction (see figure 3.9).

(b) Localized State Conduction.

At temperatures below room temperature, the activated process of extended state conduction contributes less to the total conductivity since fewer electrons obtain the thermal energy to surpass E_c, and localized states now provide the dominant conduction paths. If the wavefunctions are localized then conduction can only take place by thermally activated hopping (also known as thermally assisted tunneling) to unoccupied states at higher energies. Hence, energy needs to be exchanged with a phonon. The exact form of this conduction depends on the nature of the localized state.

(i) Conduction via hopping in localized tail-states.

Although the states in the band-tails are localized, the density of states near the mobility edge is quite high and electrons may hop to a nearest neighbour state. The temperature-dependent mobility is expected to take the form:

$$\mu_{hop} = \mu_0 \exp(\frac{-\Delta W(E)}{k_B T}) \tag{11}$$

where $\Delta W(E)$ is the activation energy for hopping *i.e.* in addition to the energy needed to raise the electron between localized states and:

$$\mu_0 = \frac{\nu_0 e R^2}{6 k_B T} \tag{12}$$

with ν_0 being a typical phonon frequency ($\simeq 10^{13} s^{-1}$) and R the hopping distance ($\sim \mathring{A}$).

The conductivity, being an integral over all available energy states will depend on the energy distribution of the density of localized states N(E). Since this increases sharply in the tail-state region, it can be assumed to behave as some power, s, of E:

$$N(E) = \frac{N(E_c)}{(E_c - E_{c'})^s}(E - E_{c'})^s \tag{13}$$

The conductivity due to the hopping electrons (σ_{hop}) can be calculated from equation 7 [31] and is of the form:

$$\sigma_{1hop} = \sigma_{0hop}[\frac{k_BT}{(E_c - E_{c'})}]^s C \exp[-\frac{(E_{c'} - E_f + \Delta W)}{k_BT}] \tag{14}$$

where $\sigma_{0hop} = eN(E_c)\mu_{0hop}k_BT$ and C is the expansion:

$$C = s! - (\frac{E_c - E_{c'}}{k_BT})^s \exp(-\frac{E_c - E_{c'}}{k_BT})[1 + s(\frac{k_BT}{E_c - E_{c'}}) + s(s-1)(\frac{k_BT}{E_c - E_{c'}})^2 + \cdots]$$

(ii) Conduction via hopping in localized states near the Fermi energy.

Nearest neighbour hopping conduction is also thought to occur in localized states near the Fermi energy *i.e.* route A in figure 3.8, where it takes the form:

$$\sigma_{2hop} = eN(E_f)\mu_{0hop}k_BT \exp(-2\alpha R) \exp(\frac{-\Delta W(E)}{k_BT}) \tag{15}$$

Where the first exponential factor represents the overlap between wavefunctions on neighbouring localized states separated by the distance R, and α is the inverse localization length. The process of equation 15 is analogous to impurity conduction in heavily doped semiconductors. In both cases (i) and (ii) above, the nearest neighbour hopping leads to a straight line from $\ln\sigma$ against $1/T$ plots, but the lines will will have differing gradients (see figure 3.9).

(iii) Conduction via variable-range hopping.

At lower temperatures, electrons in the band-tails may not even have the energy to jump to a nearest neighbour state. However, enough energy may remain to reach a more distant state which is closer in energy. Similarly for electrons near the Fermi energy, when the factor $\exp(-2\alpha R)\exp(-\Delta W/k_BT)$ from equation 15 is no longer maximum for the nearest neighbour distance, carriers will hop further distances to find states closer in energy than their nearest neighbours *i.e.* path B in figure 3.8.

Mott's treatment of variable-range hopping [32] led to a $T^{-1/4}$ dependence for the conductivity of the form:

$$\sigma_{VRH} = \frac{1}{6}e^2R^2\nu_0N(E_f)exp(\frac{-A}{T^{1/4}}) \tag{16}$$

where $A = 2.1(\frac{\alpha^3}{k_BN(E_f)})^{1/4}$.

There have been several other derivations of the conductivity formula for variable-range hopping and all produce a $T^{-1/4}$ relationship, but vary slightly in their values for the numerical factor in A.

Figure 3.9 shows the temperature dependence of the conductivity. Unlike for c-semiconductors where extended state conduction is the main transport mechanism, for a-semiconductors hopping dominates the conductivity over the wide temperature range up to room temperature. By measuring the dark dc conductivity of samples over a wide temperature range and plotting $\ln\sigma$ against $1/T$ as in figure 3.9, important information about the type of conduction process and its associated activation energy can be obtained using the relevant equations.

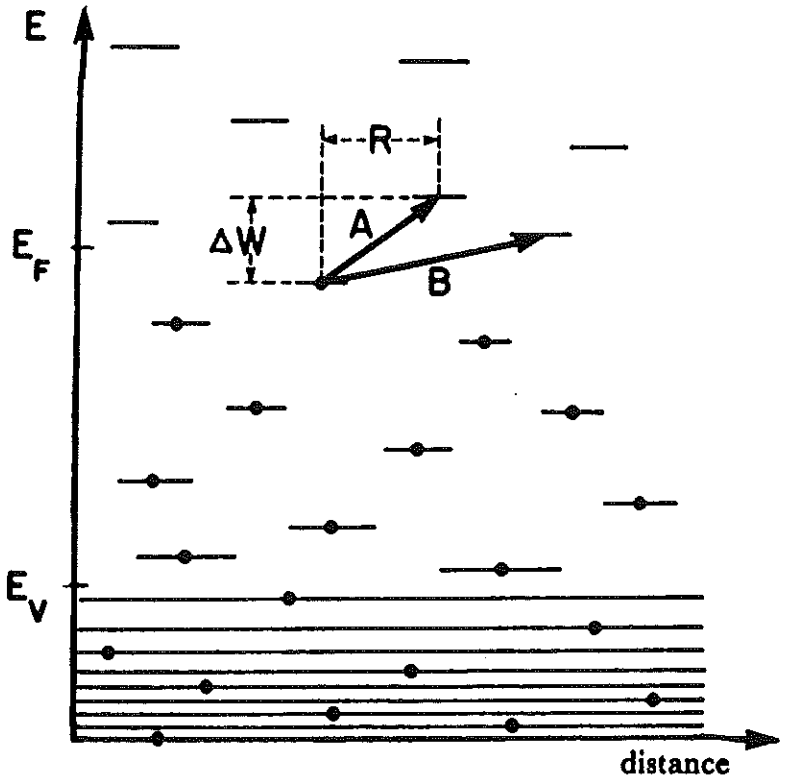

Figure 3.8: Schematic energy level diagram illustrating localized state conduction via hopping [18]

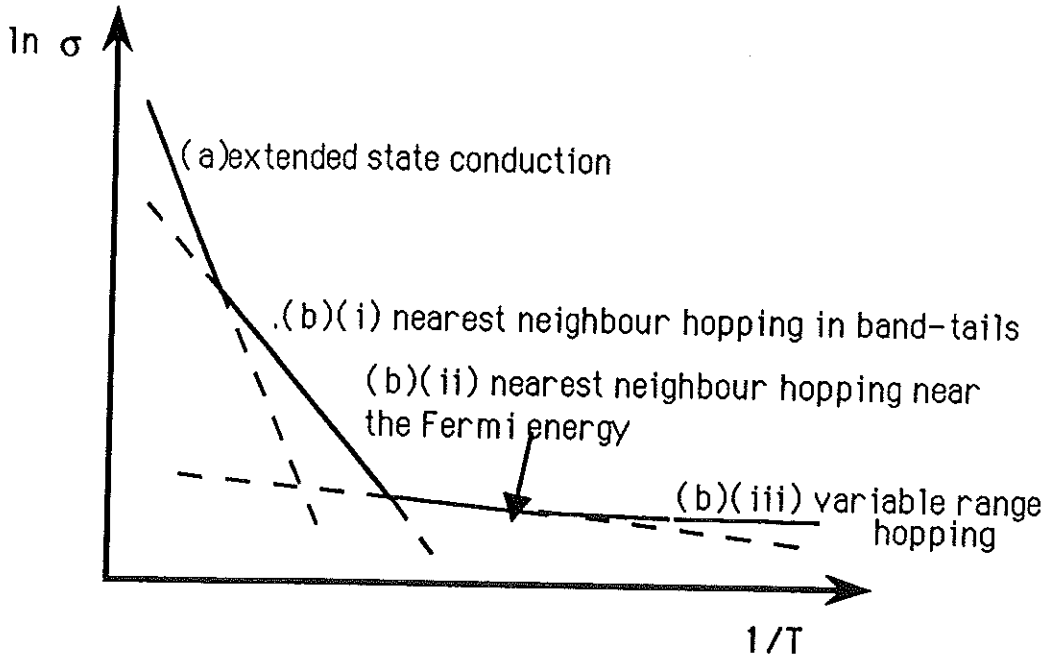

Figure 3.9: Schematic illustration of the temperature dependence of conductivity

3.5 Percolation

It is also possible to describe electron motion in an a-solid in terms of percolation theory [33]. This classical theory involves the concept of the passage of an influence through a medium, and is relevant to many diverse systems *e.g.* liquid in a porous medium, disease in a static population, information in a computer network, traffic on a road system or electron motion in condensed matter.

The passage of any such influence is clearly dependent on the 'connectedness' of the medium involved. For instance, for the 2 dimensional example of a car on a road system, the vehicle cannot get from A to B if a number of the roads are closed such that no continuous route connects A to B. As roads are re-opened at random, it may be possible to find a route that gets closer to A, but still not be able to reach it. Finally, as more roads are opened a continuous, connected route will suddenly appear and the journey made possible. This sharp change in the state of affairs is an important feature of percolation theory known as the percolation transition. It occurs at a point called the percolation threshold (P_c) when a certain fraction of pathways have been randomly opened (or conversely, closed).

Percolation can be of two forms, usually known as *site* and *bond* percolation. In the above example, site percolation would be analogous to the case where road junctions, rather than roads, were blocked and unblocked. The opening and closing of roads (bond between junctions) is an example of bond percolation.

The value of the critical fraction P_c depends on the type of percolation the physical structure of the system and its dimensionality. For 1 dimension, P_c obviously takes a value of 1, since as soon as one bond is broken or one site blocked, the system loses all connectedness. The value of this critical concentration decreases for higher dimensions, and percolation occurs when isolated clusters of connected bonds or sites

become large enough to meet and produce a continuous path across the system. In such (3D) cases, the site percolation threshold is often replaced by the critical volume fraction ϕ_c [34] where $\phi_c = \mathrm{v}P_c^{site}$ and v = the filling factor for the lattice *i.e.* corresponding to the packing of equal, non-overlapping spheres centered on the lattice sites.

As mentioned above, it is possible to apply percolation theory to electron transport in a-materials [35], though the model is obviously only valid if tunneling is precluded. At low energies, electrons reside in localized states which are confined in space. As the energy in the system is increased, these regions grow and merge until, at a critical energy, an allowed channel would be formed throughout the sample volume and the electrons can therefore move anywhere (extended state conduction).

This sort of transition is also applicable to the case of metal impurity atoms doped into an a-semiconductor. As the concentration of dopant increases, the wavefunctions of the impurity atoms begin to overlap, at first in clusters and eventually throughout the sample allowing extended state conduction. Thus it can be seen that these transitions are analogous to the previously mentioned localization $\leftrightarrow$ delocalization and insulator $\leftrightarrow$ metal transitions [16].

Chapter 4

Sample Preparation and Characterization Techniques

4.1 Sample Preparation

Of the wide range of of methods available for the production of amorphous materials (outlined in section 2.3), sputtering has become one of the most popular for the preparation of semiconductor:metal alloys. Sputtering is a physical process of film deposition that usually occurs as a result of a glow-discharge and there are many varied forms of sample deposition which employ this principle.

4.1.1 The Sputtering Principle

Sputtering is the vaporization of a target material by bombardment with high energy ions. The impact causes atoms or molecules to be ejected from target surface and these may then condense elsewhere to form a thin-film of the material.

Although there are exceptions (see for example section 4.1.2d), the ions necessary to initiate sputtering are usually produced by a glow-discharge (in argon or another inert sputtering gas) formed between the target material to be eroded and the substrate where deposition is to take place. Figure 4.1 shows a greatly simplified representation of such a sputtering system.

The vacuum chamber is typically held at a pressure of $\sim 10^{-2}$mbar of the sputtering gas, and a dc or rf potential is applied between the target and substrate (which is usually electrically grounded and may be heated or cooled). Details of the simple dc case are essentially explained in section 4.1.2a.

Application of an rf voltage to the target causes positive ions from the plasma to be attracted towards it during each negative half-cycle. However, during the next positive half-cycle a larger number of electrons are attracted to the target, owing to their increased mobility over the heavier ions, resulting in the build-up of a negative bias (V_{bias}) on the target (see figure 4.2). On reaching this so-called target sheath, positive ions are now attracted and accelerated by the bias potential, and bombard the target. This can result in several different events:

i reflection — the ion may be reflected, probably being neutralised in the process

ii ion implantation — the ion may become buried in the target

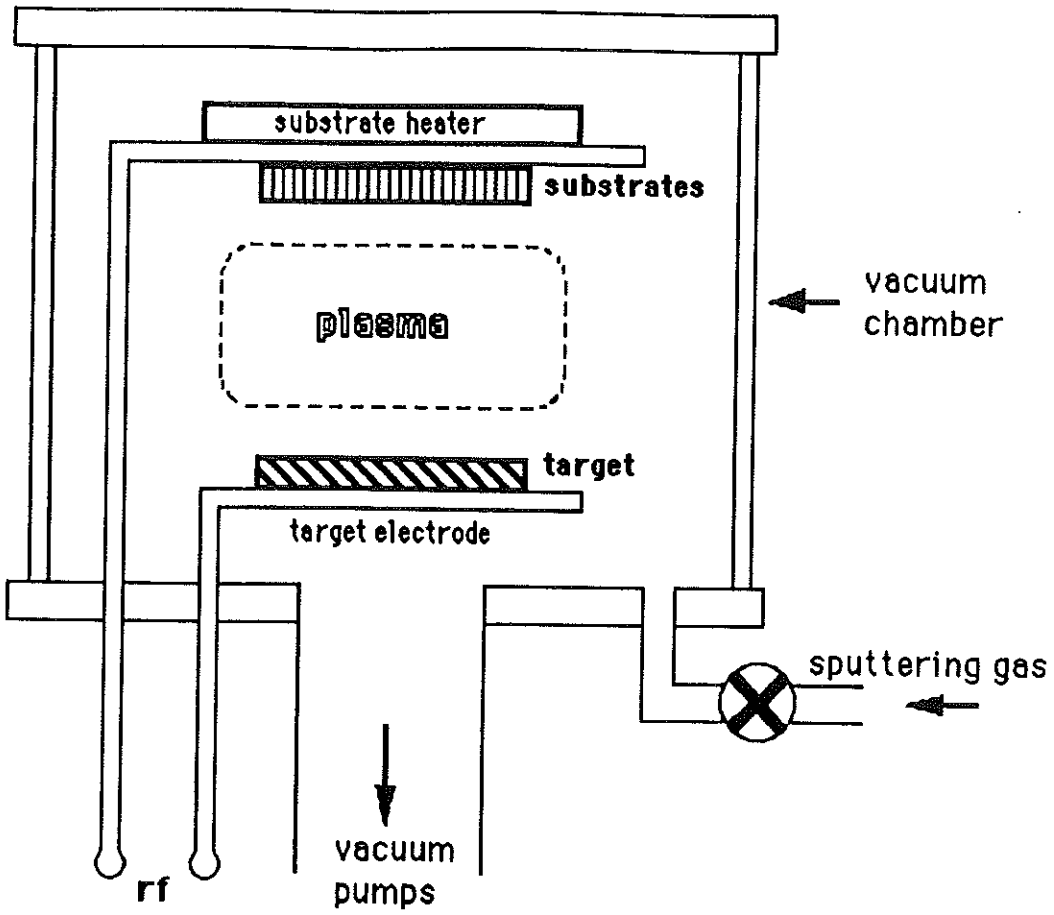

Figure 4.1: Schematic representation of an rf sputtering system.

iii radiation damage — the ion may cause structural rearrangements such as vacancies or interstitials.

iv secondary electron ejection — electrons ejected from the target may help to maintain the plasma by causing more ionisation or may neutralise approaching positive ions

v sputtering — the ion impact may set up a series of collisions between atoms or molecules of the target, eventually causing one of these particles to be ejected.

The ejected target material is then carried to the substrate by the following half-cycle of the rf field, though some backscattering may occur due to collisions with gas atoms.

At the substrate, sputtered atoms condense on the surface and their diffusion is influenced by its nature and temperature. Diffusing atoms join with others to form doublets and triplets *etc.* This nucleation and growth of groups of atoms continues until adjacent clusters coalesce to form a continuous layer. The resulting film will be amorphous if the temperature of the substrate is sufficiently low to reduce adatom mobility enough to prevent crystallization; though the temperature required will depend on the material being sputtered. Heating of the growing film and some re-emission of the deposited material will occur due to analogous bombardments at the substrate surface. These include:

i neutral bombardment by sputtered target atoms or reflected, neutralised sputtering gas ions (which may become embedded in the growing film)

ii positive ion bombardment by sputtering gas ions accelerated across the substrate sheath

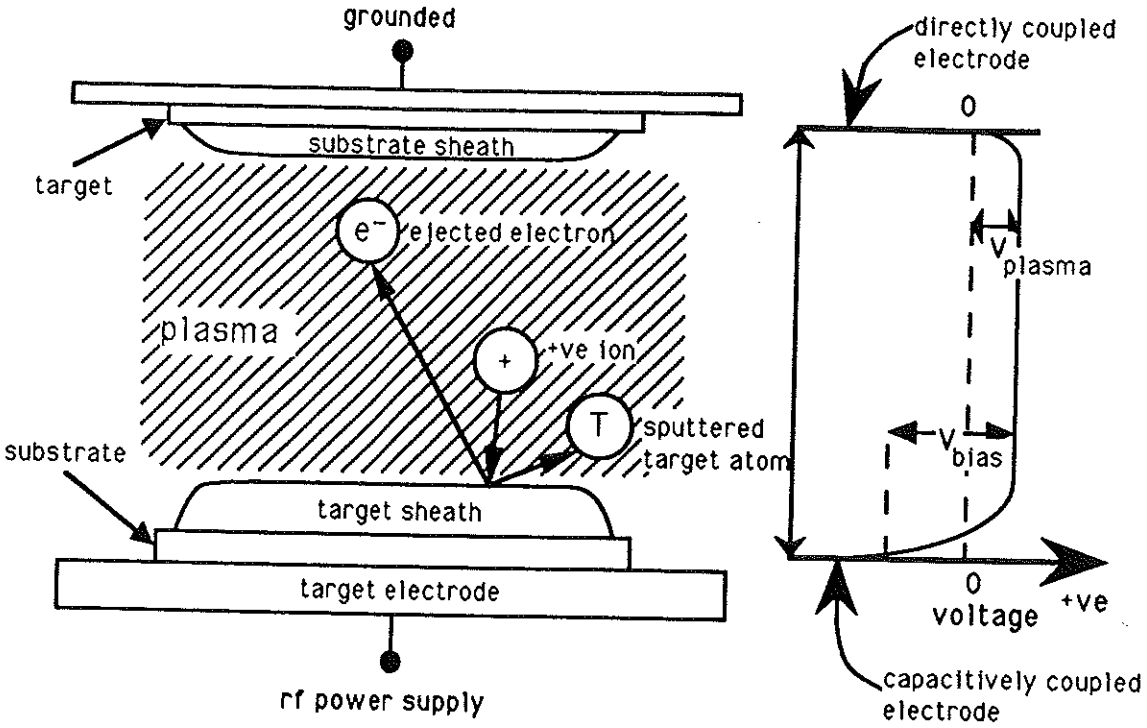

Figure 4.2: Schematic diagram of an rf sputtering electrode arrangement and potential distribution

iii electron bombardment by the few electrons from the plasma which have enough energy to surmount the substate sheath potential or fast secondary electrons ejected by the target.

The ratio of the number of atoms ejected from the target surface to the number of incident ions is known as the sputtering yield. It depends on many parameters, for example mass, energy and incident angle of the bombarding ions; mass and binding energy of the target atoms and factors which affect interactions between the two, such as sputtering gas pressure, rf power, bias voltage of the target and sputtering system geometry.

The sputtering yield determines the erosion rate of the target material, but not necessarily the deposition rate. In addition to the complication of re-emission of deposited material, it may not be valid to use yield values for pure metals when alloys, compounds or mixtures are sputtered. Multicomponent targets do not necessarily produce films of the naively expected composition, since the sputtering yield of material A from a matrix of A and B can differ considerably from that due to A alone. Therefore, deposition rates and film compositions for a particular set of parameters on any specific sputtering system have to be determined by calibration (see section 4.2).

4.1.2 Sputtering Techniques

(a) DC Sputtering

This is one of the simplest methods of sputtering. It involves the application of a high negative voltage (typically 1 - 5kV) to the target, thus attracting positive ions from the plasma and inducing sputtering. However, this technique is limited to metal

targets or to materials sufficiently electrically conducting that they can act as a high voltage electrode. Insulating materials would cause a build-up of positively charged gas ions which would repel the sputtering ions.

(b) RF Sputtering

A more common approach is to apply a radio-frequency field (typically of around 13.5 or 27MHz) capacitatively coupled to the target. The rf field enhances gas ionization and hence increases sputtering rates; but the main advantage of rf sputtering over dc is that both metallic and insulating targets can be used since positive ions are attracted to the target only during each negative half-cycle.

(c) Magnetron Sputtering

Another method of increasing ionization efficiency is to apply a transverse magnetic field normal to the electric field of conventional 'diode sputterers' (essentially described in (a) and (b) above) by the addition of permanent magnets behind the cathode target. A magnetic field parallel to the cathode surface helps to contain primary electrons in the vicinity of the target, reducing the risk of them being lost to the chamber walls or of bombarding the substrate and hence increasing their chances of causing more ionization. Both dc and rf magnetrons exist.

(d) Ion-beam Sputtering

The sputtering systems described above are ineffective at pressures below about

10^{-3}mbar due to the scarcity of ions. In ion-beam sputtering the ions are produced in a high-pressure chamber then extracted with the help of suitable electron and ion optics to obtain a high-density beam of ions which may be directed at the target in high vacuum. Ion-beam sputtering is often called secondary ion-beam deposition to distinguish it from primary ion-beam deposition where the ion-beam itself consists of the film material to be deposited. Several types of ion source are available, the most commonly used being the duoplasmatron and the Kaufman ion source.
Further details on sputtering techniques can be found elsewhere (see for example [24, 36]).

Other variations in basic sputtering techniques include the application of a bias potential to the substrate electrode as well as the target so that the growing film is subject to ion deposition and bombardment. This is known as bias sputtering.

Another option, and of direct relevance to the work presented here, is the inclusion of a reactive gas in addition to the sputtering gas. This reactive sputtering can produce films containing target material and the reactive gas species, and also increase the sputtering rate. Additives that cannot be introduced via the gaseous phase may be incorporated in varying amounts by the use of two or more simultaneously bombarded targets or by placing pieces of the solid additive on the permanent target surface. This method is called co-sputtering.

Further permutations involve the use of different configurations of sputtering source, for example planar or cylindrical, and the position of the substrate in relation to the target. Usually a sputtering system can offer a combination of these methods.

4.1.3 The Sputtering System

All the films in this study were prepared by planar rf co-sputtering (many also incorporating a reactive gas) using a Nordiko NM – 2000 –T8 –SE1 sputtering system, a schematic representation of which is shown in figure 4.3. The stainless steel chamber allowed access to the so-called substrate platen (removable, conducting plate to which substrates were clamped) and target surface through a 36 by 17cm front opening door, and the chamber body could be raised from the base for complete accessibility to the chamber interior.

Targets of 10cm diameter crystalline silicon or germanium were bonded with silver epoxy cement to 12mm thick copper backing plates which themselves attached to the target electrode. The backing plate acts as a capacitive component when the rf voltage is coupled to the target surface. The target arrangement was water-cooled, electrically insulated by PTFE and surrounded by a stainless steel earth-shield with 10cm diameter aperture.

The substrate electrode was vertically adjustable and included the option of heating, or cooling with water or liquid nitrogen. The substrate platen was machined from 20cm diameter oxygen-free copper and was easily removed from the electrode by virtue of its bayonet-style mounting system. Thin copper gaskets were inserted between the platen and the electrode to ensure good electrical and thermal contact. The substrate assembly was positioned vertically above the target *i.e.* sputter-up configuration. Substrate materials were clamped onto the platen using a stainless steel contact mask. A rotary shutter positioned just below the level of the substrates allowed sputter-cleaning of the target before deposition. See figure 4.3.

The chamber was pumped by a Varian VHS – 250mm oil diffusion pump (approximate pumping speed $2000ls^{-1}$ for air and $3000ls^{-1}$ for hydrogen) with a liquid

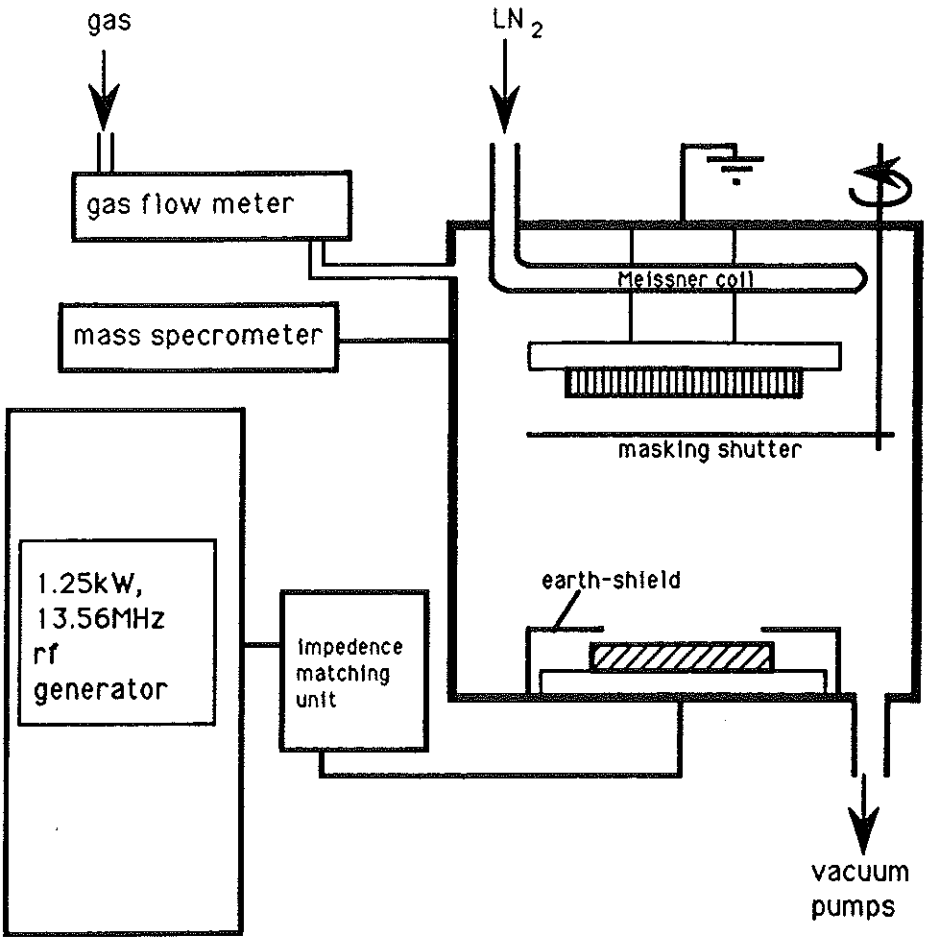

Figure 4.3: Schematic representation of the sputtering system used

nitrogen cold-trap. A water-cooled baffle below this trap helped to reduce the prescence of pump oil components into the chamber. The diffusion pump was backed by a Leybold-Heraeus D30A direct-drive rotary pump (approximate pumping speed for air $10ls^{-1}$). A foreline trap containing porous alumina was situated between pumps to reduce the backstreaming of rotary pump oil into the diffusion pump or chamber. A quadrupole mass spectrometer (VSW Vacuum Analyst) enabled the levels of any oil contamination in the chamber to be monitored, in addition to examining the proportion of residual gases remaining before sputtering.

This arrangement provided a base chamber pressure of $< 3\times10^{-7}$mbar. This could be further reduced by filling the copper 'Meissner' coil, situated around the substrate electrode, with liquid nitrogen. This was particularly effective in condensing water and hydro-carbons left in the chamber, thereby removing possible film contaminants and reducing the chamber base pressure to $\sim 10^{-7}$mbar. See figure 4.3.

The gas flow into the chamber was controlled through piezoelectric valves by a Vacuum General 78 - 7 flow ratio and pressure control system. A Vacuum General CM capacitive manometer monitored the absolute chamber pressure during sputtering and information from this gauge was fed back to the control system to maintain the required chamber pressure and ratio of gases. Both the gauge head and valves were carefully isolated from any rf pickup which would otherwise have resulted in unreliable readings.

A pneumatically-driven throttle plate positioned above the diffusion-pump port was used to reduce the pumping speed, and hence the gas-flow rate, during sputtering by partially blocking the gas exit to the vacuum pumps so that suitable pressures (typically $0.5 - 1.5\times10^{-2}$mbar) could be obtained without using large quantities of gas. This was particularly valuable when using deuterium as the reactive gas, due to

its high cost. The plate was removed during pumpdown to allow maximum pumping speed.

The rf power was provided by a 1.25kW, 13.56MHz rf generator. Since the output impedence of the generator was not equal to the impedence of the target electrode, a matching unit was employed between the two. This unit tuned the circuit by use of inductance coils. The rf power supply meters continuously read the input and reflected power so that optimum tuning could be achieved.

4.1.4 Experimental Conditions

Since the adhesion of sputtered material is greatly influenced by the nature of the substrate surface, it was important that the substrates were contaminated as little as possible. Therefore, all substrates were handled carefully with tweezers and cleaned thoroughly to encourage deposition. The cleaning procedure usually involved washing the substrate in acetone and then ultrasonically cleaning it in methanol, or simply washing it in methanol where the former method was not suitable (*e.g.* for polypropylene). The substrate platen and contact mask were also cleaned and rinsed with methanol before the substrate materials were clamped into position and the platen was inserted into the chamber.

In the case of the semiconductor:metal alloy films, the semiconducting target was prepared by placing a number of the metal pieces onto the target surface. These were uniformly arranged to ensure even mixing in the plasma and hence to produce a macroscopically homogeneous distribution of the metal in the films. A target – substrate separation of 5.5cm was used throughout this study.

Once the chamber had been sealed and pumped to its base pressure, the mass

spectrometer was used to check for residual species. At this stage, the main contaminants were usually found to be nitrogen/carbon monoxide, water and, to a lesser extent, oxygen and various hydrocarbons. The readily condensible species could be reduced considerably by the addition of liquid nitrogen to the Meissner coil. A nitrogen:oxygen ratio of around 4:1 was indicative of a slow air leak, since the ratio would normally be considerably higher due to the presence of carbon monoxide (having the same molecular mass as nitrogen); all gases having approximately the same pumping rates for the diffusion pump.

Prior to deposition, the sputtering gas (99.998% pure argon) and the reactive gas (99.993% pure hydrogen or 99.7% pure deuterium) if used, were flushed through the chamber for at least half an hour to help remove any remaining contaminants, especially air that may have leaked into the gas lines while not in use. The reactive gas pressure was reduced before the plasma was ignited and the reflected power reduced to a minimum by tuning of the matching unit. With the substrate shutter in place to prevent deposition, the target was etched in a pure argon plasma for around thirty minutes to remove any adsorbed impurities. The gas mass-flow ratio, rf power and total gas pressure were then adjusted to their required values, the substrate shutter removed and deposition allowed for a recorded time. The Meissner coil was kept full throughout deposition. Typical conditions for deposition are given in Table 4.1.

Substrate heating was used in initial studies of the intrinsic a-Si:H system, as this has been found found to produce the best electrical properties [37], but when preparing the a-Si:M:H alloys (where M = metal) the resultant films appeared to have a partially crystalline structure (see section 4.2.1) so this was abandoned. Various sputtering pressures and their effect on the deposition rate had previously been studied to determine the optimum value of 7.3×10^{-3}mbar.

Table 4.1: Typical deposition conditions

rf power	~200 watts (power density ~2.5Wcm^{-2}
reflected power	$\langle$ 1W
target bias	~700V (dependent on target composition)
chamber pressure	7.3×10^{-3}mbar
gas mass-flow ratio	10:1, Ar:H_2 or D_2
substrate temperature	ambient

After the required deposition time, typically 8 hours, the plasma was extinguished and the chamber repumped to its base pressure. When all the liquid nitrogen had evaporated from the Meissner coil, the chamber was vented with oxygen-free nitrogen and the samples removed.

4.2 Sample Characterization Techniques

A variety of techniques were employed to determine various parameters and properties of the films. Those techniques most commonly used to characterize the systems prepared are described briefly in this section.

4.2.1 Initial Microstructural Determination

Although later measurements were to yield more detailed microstructural information, it was important to obtain initial indications of film morphology to avoid wasted effort later.

Extremely thin samples (estimated $\sim 200\mathring{A}$ thickness) were deposited onto single lithium fluoride crystals, freshly cleaved to ensure a clean, flat surface. These films could be prepared simultaneously with other, thicker samples by use of a subsidiary mechanical masking shutter which attached to the substrate platen to cover only this one substrate component. The film was floated off the crystal in a dilute solution (~5%) of hydrofluoric acid and carefully transferred to a standard copper electron microscope grid.

A Joel Jem 100CX transmission electron microscope was used to examine the films by room temperature selected-area electron diffraction (SAED). As previously mentioned, alloy films deposited using a heated substrate produced sharp rings associated with crystallinity (sometimes with spots superposed on them, indicative of large polycrystalline inclusions). Consequently, substrate heating was abandoned and all subsequent films tested gave the diffuse patterns or haloes associated with amorphous structures (see figure 4.4).

X-ray diffraction using a laboratory source and a Debye-Scherrer camera was

performed on powdered samples of the films removed from glass substrates. This technique also showed all films tested to be amorphous (see figure 4.5) and in some cases was subsequently used to study the samples after crystallizing them by heating.

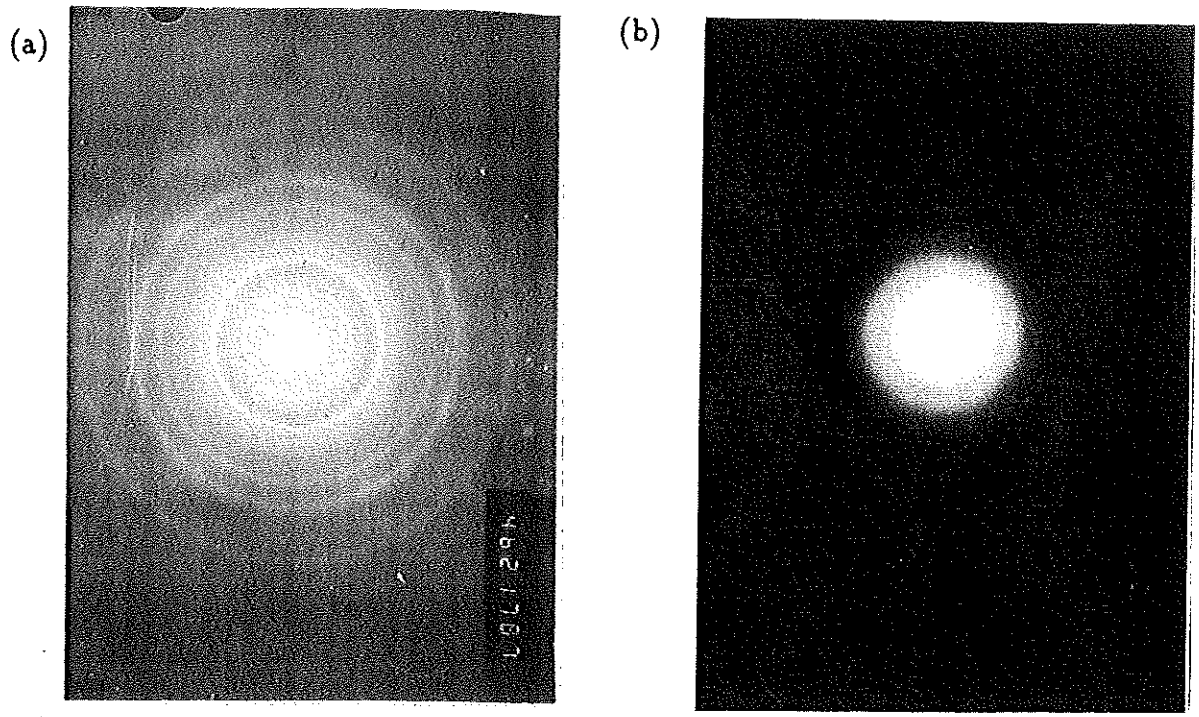

Figure 4.4: Selected-area electron diffraction patterns of a-Si:Ni:H prepared (a) with and (b) without substrate heating.

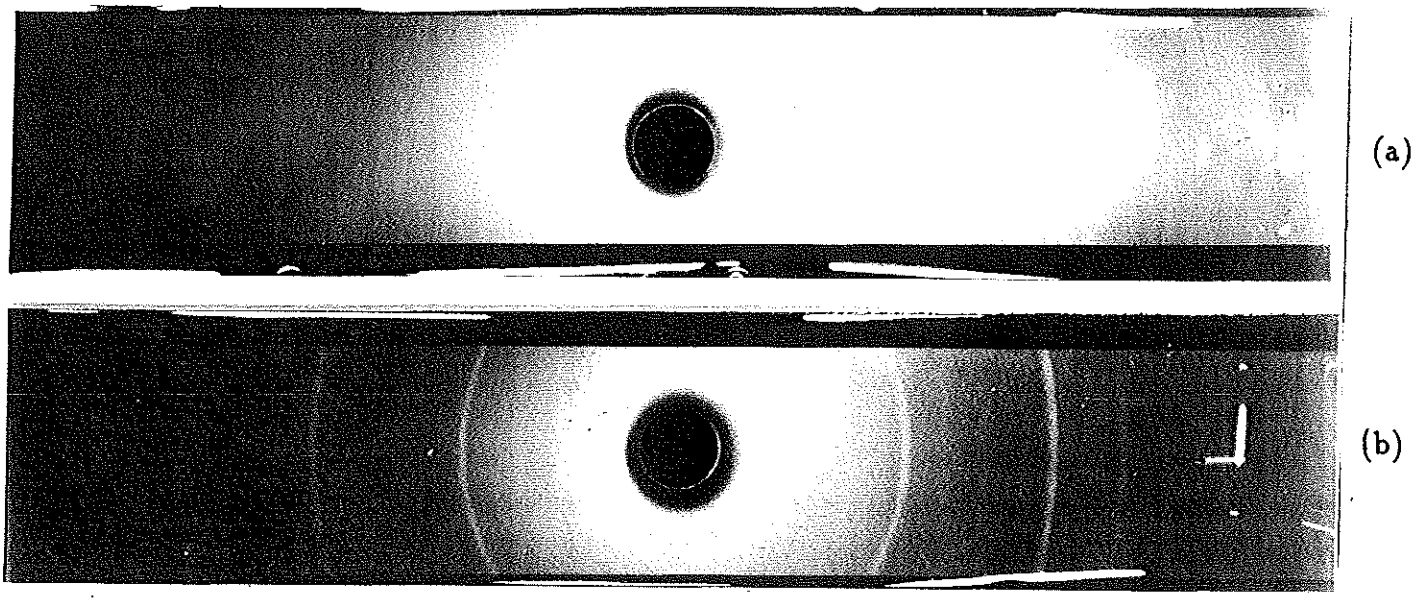

Figure 4.5: Laboratory X-ray diffraction patterns of a-Si:Ni:H (a) before and (b) after heating to 450°C.

4.2.2 Thickness Determination

Film thicknesses were measured using a Talysurf (Rank Taylor Hobson) to scan across any pinholes in the films deposited on glass substrates. In the event that no suitable pinholes could be located, grooves were scored in the central region of the film by a sharp implement. This mechanical method gave a direct graphical output that could be estimated to $\pm \sim 0.2\mu$m. Film thicknesses of about 2μm typically resulted from a deposition time of eight hours, corresponding to a deposition rate of around $0.7\text{Å}s^{-1}$.

4.2.3 Compositional Analysis

Since the metallic content of the films was altered by varying the number of metal pieces on the target surface, sample composition could not be predicted a priori. Initial compositional analysis was undertaken on an ISI - DS 130 scanning electron microscope which included a microprobe facility. This was operated in energy dispersive mode, and samples were deposited on metallic substrates (usually aluminium) to prevent charging during analysis. This technique involves the focussing of a 15keV electron beam onto the sample surface and the detection and analysis of the resulting characteristic X-ray emission. Using this method, the percentage of argon incorporated during the sputtering process could also be estimated and the films checked for any impurities. Unfortunately, the instrument could not detect elements with atomic numbers below $z = 11$, so the proportion of reactive gas and amount of any oxygen contamination could not be estimated, though the latter was easily attainable by other techniques (see sections 7.5.1 and 8.2).

However, since no software was available to apply the ZAF correction (essentially three corrections for the atomic number, z, of the emitting atom; the absorption,

A, of the X-rays by surrounding atoms and fluorescence, F, in the sample) the results obtained were not absolute. Furthermore, this characteristic-energy dependent technique was not able to distinguish easily between the K-edge of germanium and the L_3-edge of gold (11.1 and 11.9 keV respectively) in the germanium:gold samples; therefore all sample compositions were later checked (and if necessary corrected) by the mass dependent technique of Rutherford backscattering using a 1.5MeV $^4He^+$ beam and a scattering angle of 160° at the SERC facility at the University of Surrey.

4.2.4 Conductivity Measurements

For the important characterization measurements of dc conductivity, films were deposited onto Corning 7059, a highly electrically resistive barium-alumino-silicate glass. Following deposition, the films were placed in an Edwards 12E6/1514 coating unit and four 99.99% pure gold electrodes were evaporated onto the film surface using a contact mask. This gap-cell geometry could be used in 2-probe or 4-probe configuration; the latter being necessary for the alloy films with higher conductivity where contact resistance was no longer negligible. Samples were mounted onto a sample stage and a silver-based electrically conducting paint was used to attach fine copper wires to the electrodes, and two copper-constantan thermocouples directly onto the substrate. This sample arrangement fitted into a Delta Design Environmental Control Cabinet which was evacuated to a base pressure of around 10^{-6}mbar then flushed and filled with a slight over-pressure of helium which acted as an inert heat exchanger. Voltage was supplied by a Coutant 50V dc stabilised power supply and the current read by a Keithley 616 digital electometer. The voltage drop across the sample was measured by a Keithley 181 digital nanovoltmeter.

Using this arrangement, dc 'dark' conductivity measurements were taken in the

temperature range 300 – 475K which was sufficient to determine the activation energy and hence the electronic quality of the initial films produced. Parallel research at the University of Leicester extended this temperature range down to 100K by the flow of liquid nitrogen vapour into the chamber from a pressurized dewar to investigate further the electronic properties of samples prepared in this study.

Chapter 5

EXAFS Theory and Data Analysis

5.1 EXAFS Theory

Extended X-ray Absorption Fine Structure (EXAFS) represents the oscillations of the X-ray absorption coefficient, $\mu(h\nu)$, at energies up to $\sim$1keV above the X-ray absorption edge of elements in a condensed matter system. These oscillations arise from interference of the outgoing wavefunctions associated with photo-excited electrons with those waves which have been elastically backscattered by the surrounding atoms (see figure 5.1).

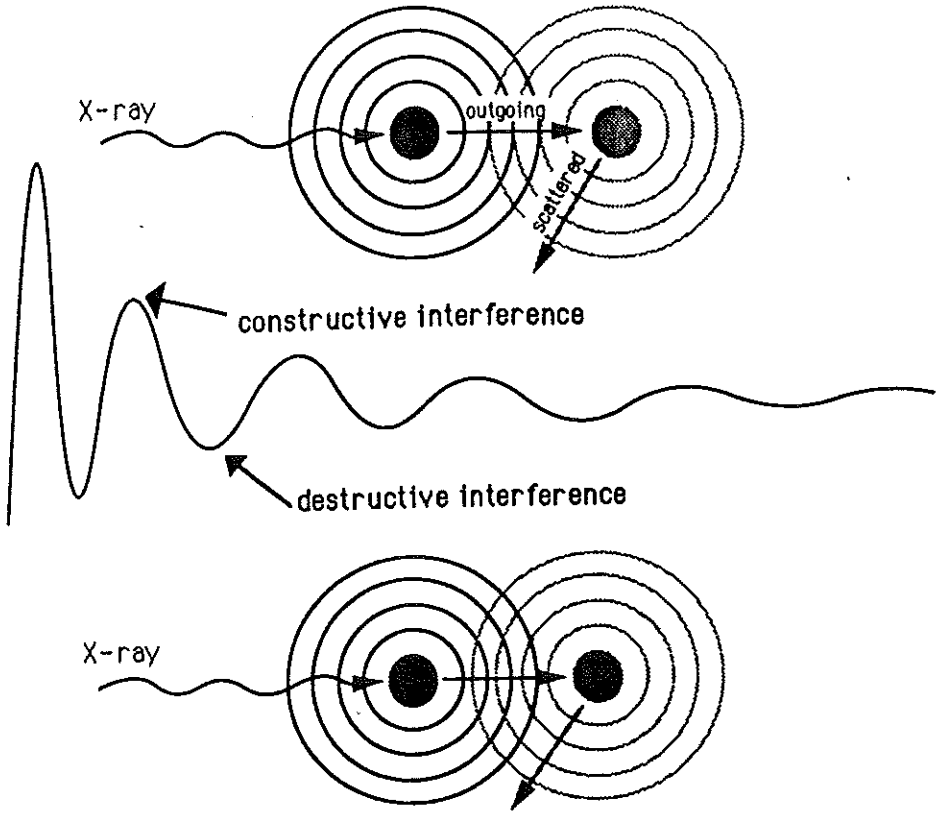

Figure 5.1: Schematic representation of the production of EXAFS

5.1.1 Review of the EXAFS Technique

Fine structure beyond absorption edges was first detected experimentally in 1920 [38, 39]. Initial studies only observed the X-ray absorption near edge structure (XANES) occurring in approximately the first 50eV above the edge (see figure 5.2), but by the end of the decade structure extending to hundreds of eV beyond the edge *(i.e.* EXAFS) was being reported [40, 41].

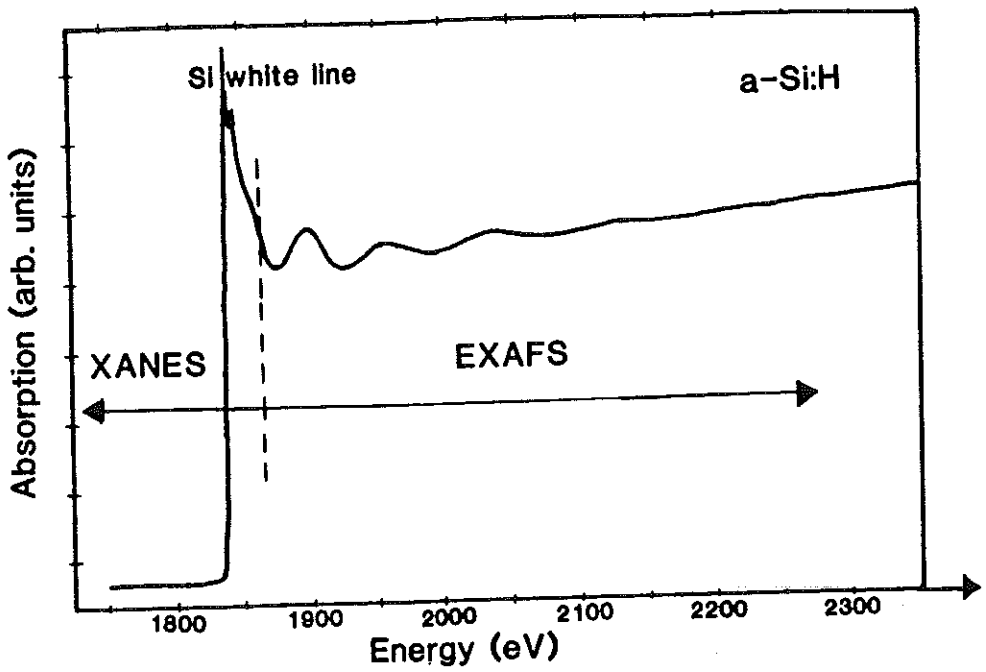

Figure 5.2: Si K-edge spectrum showing the strong near edge resonances (XANES) and the weaker EXAFS oscillations.

Basic physical explanations were provided by Kronig; firstly in terms of the long-range order of solids [42] and then using the idea of short-range order [43]. Both theories predicted fine structure oscillations, but were too simple with the result that a lack of agreement between theory and experiment created confusion over the exact theoretical form of the EXAFS function. This theoretical uncertainty, combined with the poor experimental spectra available at the time, meant that little use was made of the EXAFS structure as an experimental tool for most of the following half century.

Interest was renewed in 1971 by the work of Sayers et al. [44] which showed that a short-range order theory gave the correct form for $\chi(E)$, which was defined experimentally as the normalized oscillatory part of the absorption coefficient, μ:

$$\chi(E) = \frac{\mu(E) - \mu_0(E)}{\mu_0(E)} \tag{17}$$

where μ_0 is the smoothly varying background corresponding to the absorption coefficient of an isolated atom.

Furthermore, this work [44] showed that a Fourier transform of the EXAFS with respect to the photoelectron wavenumber (k) would peak at distances corresponding to near-neighbour coordination shells of atoms.

Around the same time, the development of storage rings as stable sources of synchrotron radiation (see Chapter 6) meant that EXAFS experiments could be performed over a wide spectral range with X-ray intensities three or more orders of magnitude greater than those obtainable from X-ray tubes, reducing measurement times and improving statistics.

The first EXAFS studies utilizing synchrotron radiation were performed in 1974

[45]. These experiments involved an X-ray transmission investigation, since the absorption of an X-ray photon of energy E by a sample of thickness t is given by:

$$I_T(E) = I_0(E)\exp(-\mu_{total}(E)t) \tag{18}$$

where I_T and I_0 are the transmitted and incident intensity respectively and μ_{total} is the total absorption coefficient of the sample which gives a measurement of the EXAFS (see equation 20). Since then there has been much development in EXAFS studies, and other detection techniques such as fluorescence and electron yield are now regularly used (see Chapter 6). The relatively easy measurement and short timescales of such EXAFS experiments, combined with their comparatively simple and direct data analysis (see section 5.2) makes EXAFS a practical structural tool. However, its most useful quality is its atom-specific nature which means that the local atomic arrangement can be determined about each atom type individually. This fact makes the technique particularly useful for the study of multicomponent and dilute systems, including thin-films. Since the interpretation of EXAFS is based upon a SRO theory, liquid, amorphous and crystalline materials can be studied and it has proved possible to apply the technique successfully to a wide variety of systems.

Apart from computational difficulties, to be discussed later in this chapter, the main limitation to the EXAFS technique is the fact that it only gives information up to 4 - 5 $\AA$ from the absorbing atom. Thus while being a useful complement to diffraction techniques, it cannot replace them. Samples in which the absorbing atom species may exist in a variety of bonding configurations present a particular difficulty since, like many other techniques, EXAFS analysis can only return average parameters for the system.

The use of EXAFS for the structural investigation of amorphous materials has

been discussed extensively [46, 47, 48, 49] and reviews of such studies including group IV materials and their alloys have been given by Cargill [50], Gurman [51] and Greaves [52]. In this study, the EXAFS technique was used to probe the structure of three amorphous metalloid:metal alloys: a-Si:Ni:H, a-Si:Sn:H and a-Ge:Au.

5.1.2 Basic EXAFS Theory

The basic origins of the EXAFS structure are easy to understand. The attenuation of X-rays by a medium can occur via three processes: scattering, pair production and photo-electric absorption. Below about 40keV, the latter is the dominant process. When the energy of an X-ray exceeds the binding energy of a bound electron, the photon can be absorbed by an atom, exciting the electron to a continuum state, (Rydberg transitions to weakly bound states are not considered in EXAFS). These absorption edges are known as K-edges when the ejected electron comes from the n=1 shell and L-edges if it comes from the less tightly bound n=2 shell. These are, at present, the only absorption edges used to observe EXAFS. For a monatomic gas such as argon at atmospheric pressure, the ejected photoelectron, which can be represented as an outgoing spherical wave with a wavelength $2\pi/k$ (where k = photoelectron wavevector) undergoes little or no interference due to the lack of closely neighbouring atoms. However, in condensed matter, atoms surrounding the absorbing/emitting atom can scatter this photoelectron; though the remaining deep core hole is unaffected to a good approximation. Hence, the final state wavefunction is a superposition of the outgoing and scattered waves.

The X-ray absorption can be described quantum mechanically by a matrix element between the initial and final states. Since the major contribution to this absorption matrix element comes from regions of space very close to the centre of the absorbing

atom [53], it is only necessary to determine the final state modifications (due to backscattering) in *this* region in order to deduce the EXAFS function $\chi(k)$.

At the absorbing atom centre, the backscattered waves may interfere with the outgoing wavefunction either constructively or destructively (see figure 5.1) depending on their relative phase; and this phase difference will alter with variations in the wavelength of the outgoing photoelectron *e.g.* as the X-ray energy increases above the absorption edge. It is because only elastically scattered electrons can contribute to this interference and the elastic mean free path is short, that EXAFS only depends on the local environment. The phase variation is also dependent on the distance (R) between the central and backscattering atoms; hence EXAFS gives information on this interatomic separation. Although the total phase of the backscattered wave is largely made up of the product of the photoelectron wavevector (k) and the distance travelled ($2R$), it also contains additional contributions from the scattering process and from the passage of the photoelectron out and back through the surrounding atom potential. The amplitude of the oscillations depends on the number of scattering atoms (N) at the distance R and also on their backscattering strength $[|f(k,\pi)|]$, which in its turn depends on the atomic number of the atom doing the backscattering. Hence, EXAFS also contains information on near neighbour coordination numbers and atom types.

In a real solid, atoms are subject to thermal motion which averages the signal over the mean square configurations of the atoms. This has the effect of reducing the amplitude of the EXAFS interference function, χ. In amorphous materials this effect is heightened by the inherent static disorder [49]. Both these contributions will produce dephasing effects which, if they are small and can therefore be considered to have a Gaussian distribution about the average distance (R), reduce the determined

average coordination number (N) by a Debye-Waller factor $\exp(-2k^2\sigma^2)$, where σ is the rms deviation around R. The effect actually depends on the scattering angle (θ) at the scattering atom and produces a factor of the form:

$$\exp(-\sigma_j^2[1-\cos\theta]) \tag{19}$$

For single scattering, when $\theta=\pi$ (*i.e.* direct backscattering), this reduces to the previous form of $\exp(-2\sigma^2)$. It should be noted that the EXAFS Debye-Waller term is not the same as that used in X-ray diffraction, which involves the mean square vibrations of atoms about their equilibrium positions. In EXAFS the mean square deviation (σ^2) is a relative one between the central and backscattering atoms. Since nearest neighbour atoms are likely to have correlated motions [54], the vibrational contributions to the σ^2 term will be less than naively assumed by consideration of a well separated pair of atoms.

Another physical effect involved in the consideration of the EXAFS function is the lifetime of the excited photoelectron state. This lifetime has two contributions: the lifetime of the unstable core hole, which has been tabulated for various atoms and shells [55] and the lifetime of the actual photoelectron. Both are finite, the latter because the emitted photoelectron may not be elastically backscattered, but may excite other electrons (multi-electron effects) or be inelastically scattered by the surrounding atoms, thus losing its coherence and its ability to contribute to the EXAFS signal. This finite mean free path, and hence finite lifetime, for the photoelectron adds to that of the core level to produce an energy uncertainty obtained from the uncertainty principle and thus a blurring of the EXAFS signal. The effects of this finite lifetime can be reduced by inclusion of a mean free path term, $\exp(-2R/\lambda)$, which represents the probability that the photoelectron is elastically backscattered to

the central atom without the hole state being filled. The mean free path (λ) measures the average distance an excited electron can travel before losing coherence with its initial state.

Consideration of all the above effects leads to Stern's [53] original approximate expression for the EXAFS function of K-edges:

$$\chi(k,R) = \sum_j -\frac{N_j}{kR_j^2}|f_j(k,\pi)|\sin(2kR_j + 2\delta_l + \psi_j)\exp(-2\sigma_j^2 k^2)\exp(\frac{-2R_j}{\lambda}) \quad (20)$$

where atomic units have been used *i.e.* lengths in Bohr radii and energies in Hartrees.

Here, λ is the elastic mean free path of the photoelectron and ψ_j is the phase of the atom specific backscattering factor, the amplitude of which is given by $|f_j(k,\pi)|$. The term δ_l is the phase shift (for a wavefunction component of angular momentum, l) produced by passage of the photoelectron through the excited atom potential. For K-edges, which involve an excitation from a 1s initial state, the selection rule Δl=1 requires the outgoing wave to be a p wave with l=1. However, L-edges involve initial states of either 2s (l=0) or 2p (l=1) and give rise to three possible angular momentum values for the final state outgoing wave. Out of these, it is the more intense L_3-edge occurring at lower energy that is used in EXAFS. All other terms have been previously introduced and their aquisition in practice will be discussed later.

5.1.3 Further Considerations

Although the original theory described above takes into account the energy losses due to inelastic scattering and finite mean free path of the photoelectron, it does not consider all of the inelastic processes that tend to diminish the amplitude of EXAFS signal. The absorption of an X-ray by an atom may, for instance, result in multiple

electron effects (sometimes referred to as shake-up and shake-off effects) rather than the emission of a single photoelectron. The excitation of a photoelectron from a core state can be considered as producing a rapid change in the potential of the central atom (sudden approximation). This may result in another central atom electron being excited to a higher bound level (shake-up) or to a continuum state (shake-off). Studies of this process [56, 57] show that the ratio of shake-off to shake-up effects is about 2:1 for K-shells of medium weight elements and the probability of such multiple-electron excitations shows no overall trend with atomic number. Since these events contribute to the absorption but not to the EXAFS signal, they reduce the amplitude of the oscillations. Thus, a complete theory needs to take them into account and equation 20 becomes:

$$\chi(k,R) = \sum_j \frac{A(k)N_j}{kR_j^2}|f_j(k,\pi)|\sin(2kR_j + 2\delta_l + \psi_j)\exp(-2\sigma_j^2k^2)\exp(\frac{-2R_j}{\lambda}) \quad (21)$$

where $A(k)$ is the amplitude factor to account for multiple electron effects. Since these effects are due to the appearance of the core hole rather than the passage of the photoelectron, $A(k)$ can be considered independent of the X-ray energy within the sudden approximation. However, it is written as a function of k due to the breakdown of the sudden approximation at low k values, and it does vary with the atomic number and absorption edge of the central atom under investigation.

A complete treatment of inelastic effects in EXAFS must include not only the many-electron effects themselves but also the interference between them. However, recent work [57] has shown that interference between the intrinsic processes (*i.e.* those directly related to the remaining central atom such as core hole lifetime and shake-up/shake-off effects) and extrinsic processes (*i.e.* those related to the ejected photoelectron such as inelastic scattering) is only significant at energies very close to

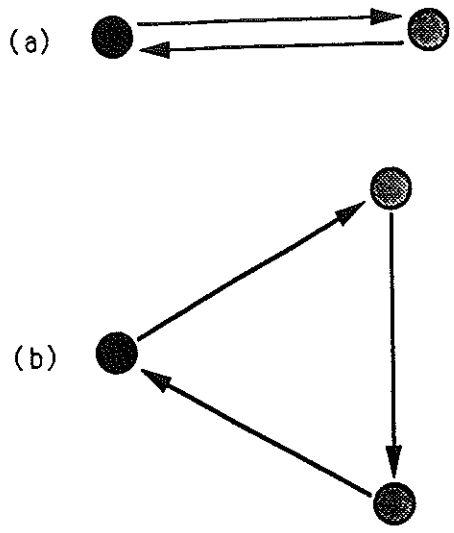

Figure 5.3: Schematic representation of (a) a single-scattering path and (b) a double-scattering path for the photoelectron

the absorption edge and can thus generally be ignored in consideration of EXAFS work.

Another process that is very significant close to the absorption edge is multiple-scattering (see figure 5.3). At low photoelectron energies (*i.e.* near to the edge) the photoelectron mean free path and lifetime are long, allowing multiple-scattering events to occur. Calculation of the path sum over such electron scattering paths is complex, hence the EXAFS regime is not generally considered as starting below around 30eV above the edge, avoiding this region but also limiting the range of usable EXAFS. A full multiple-scattering treatment is included in the more complicated XANES theory [58, 59].

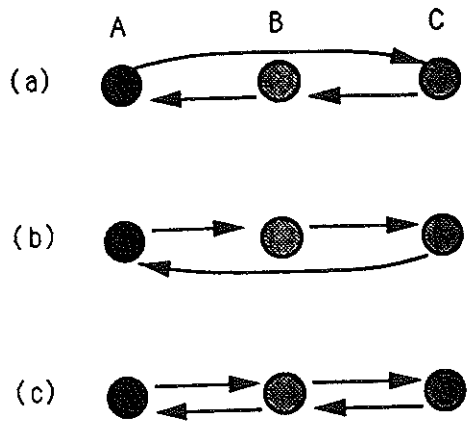

Figure 5.4: Schematic representation of some important forward scattering processes: (a) and (b) double-scattering and (c) triple scattering.

For much EXAFS work only single-scattering need be considered; however, in some situations the contribution from a few, strong, multiple-scattering paths has to be included. For example, when relatively local atoms lie directly behind one another with respect to the central atom (see figure 5.4). In this case the contribution from the shadowed atom (C) is greatly affected by the *forward* scattering of the shadowing atom (B). It should also be noted that while the nonshadowing type of multiple-scattering in figure 5.3(b) is small in the EXAFS region compared with the single-scattering contribution of the same shell, it may be significant compared with the single-scattering of a more distant shell. Hence multiple-scattering cannot be entirely neglected in EXAFS.

5.2 Obtaining Structural Information

Before analysis of the EXAFS can proceed, it must be extracted from the total measured absorption. The pre-edge must be subtracted to remove any contributions from lower energy edges, leaving only absorption from the atom under investigation. Now, subtracting off this atomic absorption factor (μ_0) leaves only the EXAFS function, $\chi(k)$ (see figure 5.5) with any associated background errors.

The approximate form of the EXAFS function (equation 20) due to Stern [53] was developed extensively by Lee and Pendry [60] and Ashley and Doniach [61]. Both of these theories treat the outgoing electron exactly as a spherical wave and are therefore extremely complex in terms of their mathematics. Lee and Pendry used an electron scattering theory which described the process in terms of the wavefunctions of the outgoing and scattered photoelectron. These may be expressed as sums over angular momenta and represented by matrices. In EXAFS the initial state has a well-defined angular momentum and the outgoing wave can be represented by a unit matrix. However, a single angular momentum component of the outgoing wave will give rise to many components in the scattered wave and hence the latter needs to be represented by a higher order matrix, conventionally called the Z matrix. Thus the Z matrix describes the scattering of the photoelectron and the EXAFS function $\chi(k)$ can be expressed as a linear function of Z.

The Z matrix may be split into terms corresponding to different orders of scattering *i.e.* single, double, triple *etc.* (see section 5.1.3) *e.g.*

$$Z = Z_{single} + Z_{double} + Z_{triple} + \cdots \tag{22}$$

Because only elastic scattering need be considered, and the elastic mean free path

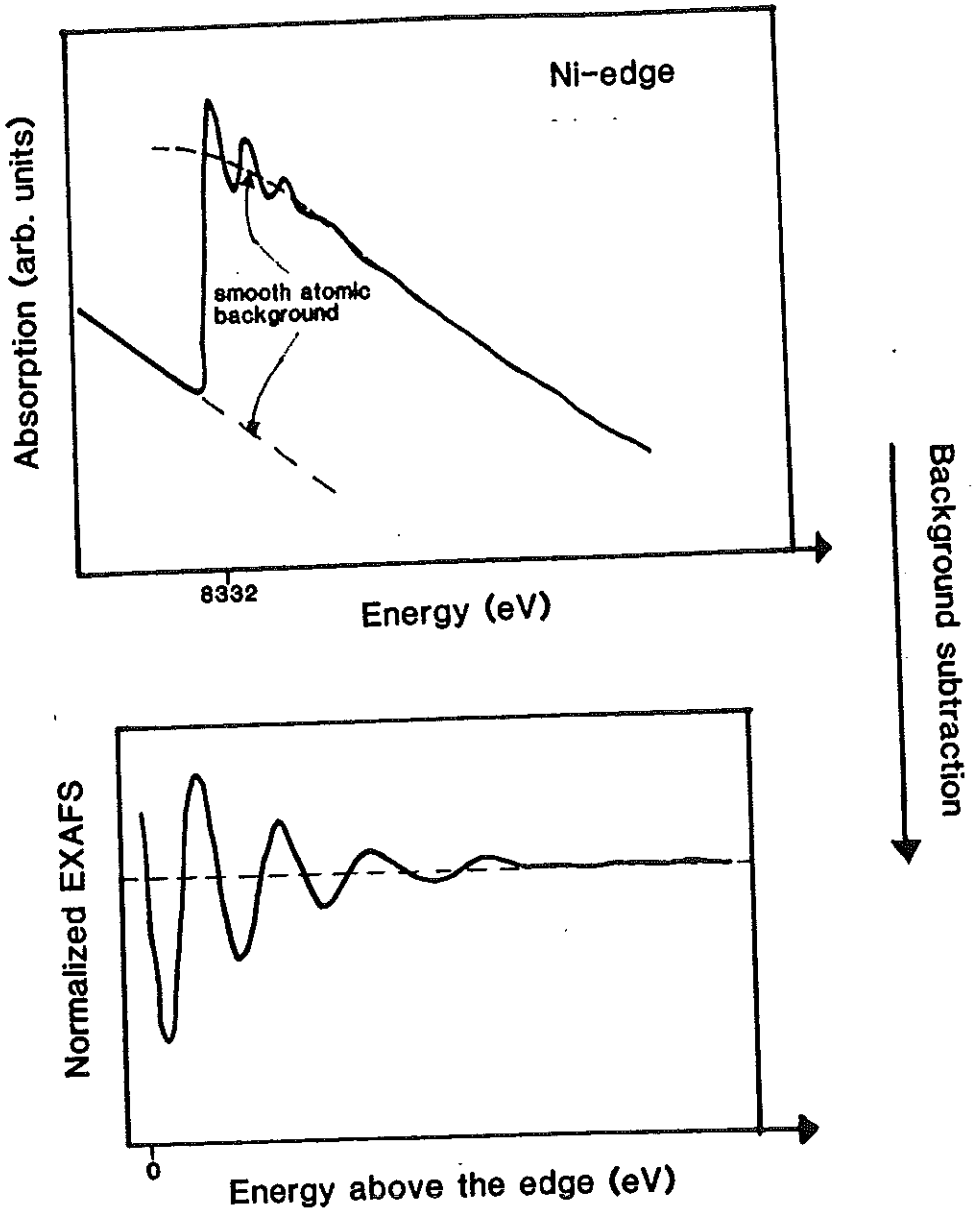

Figure 5.5: Subtraction of smooth atomic background to yield the normalized EXAFS function.

is short, only a few orders will contribute and often only single scattering need be included. Also, since the major contribution to the absorption matrix comes from regions of space very close to the nucleus of the central atom (see section 5.1.2), for a given order of scattering, only the few scattering paths that return the photoelectron exactly to the central atom have to be introduced. Thus the path sum is calculable, but limits EXAFS to local structure.

The terms in the Z matrix are complex and involve angular integrals and Hankel functions (solutions to the Schrödinger equation for a constant potential and particular angular momentum). The complicated expression produced, although analytically correct, takes a large amount of computer time to evaluate. Since this is impractical for interactive analysis of EXAFS data, several approximate theories have been developed for calculating $\chi(k)$ based on different forms and approximations for the matrix Z. These faster theories form the basis of the data analysis programs available at present.

5.2.1 Faster Analytical Approaches

(a) The Plane Wave Theory

The complex nature of the exact EXAFS expression lies in its use of spherical waves, in which each angular momentum component needs to be treated independently. However, if the photoelectron energy is sufficiently high or the interatomic distances sufficiently large that the curvature of the outgoing wavefunction can be neglected, then it can be approximated by a plane wave. This approximation is the basis of the plane wave approach and greatly simplifies the theory. Mathematically this is achieved by replacing the Hankel functions used in the full curved wave theory

by the first term in their expansion. This term is a simple exponential and corresponds to the plane wave form. The plane wave theory is, in fact, Stern's original approximate theory. The Plane Wave Approximation (PWA) of the EXAFS function is equivalent for both K- and L-edges, excepting a minus sign for the K-edge function which is introduced by the Hankel function term for p waves (l=1).

Although the PWA produces a simplified theory which enables straightforward data analysis, it is limited to the high energy part of the spectrum. Also, comparative results with a curved wave theory show that the PWA is particularly poor for orders of scattering above single [62], the theoretical errors occurring in the description of the phase of the photoelectron. An improved form of the PWA called the spherical wave theory has recently been developed [63, 64]. This theory includes higher order terms from the expansion of the Hankel function in order to include some multiple scattering effects, while still allowing fairly rapid calculation. Also, recent publication of standard distance-dependent effective backscattering factors [$f(k, R, \pi)$] [65] calculated using the full curved wave theory has led to improved accuracy for the plane wave theory; the distance dependence allowing for the inherent phase error.

(b) The Small Atom Approximation

The so-called Small Atom Approximation (SAA), originally briefly described by Lee and Pendry [60], has most recently been revived by Gurman [66]. This approximation to the full curved wave theory retains the simplicity of the PWA and its low computational timescales, but avoids its phase problem outlined above, by still approximating the spherical wavefronts as plane waves at the scattering atom — but plane waves having the correct phase and amplitude at the centre of the scattering

atom. The theory achieves this by continuing to treat the outgoing and scattered waves as plane waves, which allows rapid calculation of directional effects, but adjusting the phase to make it correct (*i.e.* the same as that given by the full Hankel function) at the centre of the scattering atom.

The approximation will be better the smaller the scattering atom and the higher the photoelectron energy, since at high energies the effective size of the scattering centre is decreases by the photoelectron's ability to penetrate deeper into the atom before scattering.

Using this theory, higher order scattering contributions can be obtained rapidly and accurately. The SAA is available in the EXCURV88 [67] data analysis package available at the SERC Daresbury Laboratory, where it was used interactively for the analysis of crystalline standard samples which showed the shadowing effect mentioned in section 5.1.3.

(c) The Fast Curved Wave Theory

The Fast Curved Wave Theory [68] does not, in fact, use any approximations and is an exact theory, treating the wavefunctions as spherical. However it does need the assumption that the sample under investigation is either amorphous or polycrystalline.

The complexities of the Lee and Pendry theory arise largely from the problem of describing the scattering of a spherical wave by an atom situated at a fixed angle from the central atom with respect to the direction of the incoming X-ray. However, in the case of amorphous or polycrystalline samples, the angle between the beam (or rather, the electric field polarization vector of the X-ray, $\underline{\varepsilon}$) and the scattering

atom as viewed from the central atom is 'randomly' distributed and it is necessary to average the absorption coefficient over the angles of these interatomic vectors relative to $\underline{\varepsilon}$. The result is that the number of directional effects that need to be considered is reduced and the angle-averaged absorption coefficient involves a sum over only the diagonal elements of the Z matrix.

For single-scattering, this angle-averaged expression contains far fewer sums than the full curved wave theory and is therefore much faster to compute while still exact. For single-scattering, computing times are comparable to those obtained from the PWA but although double- and triple-scattering contributions may be similarly simplified, they remain too slow to be calculated interactively with present computing facilities.

The Fast Curved Wave Theory is employed interactively by the Daresbury Laboratory EXCURV88 program to give single-scattering contributions to the data from amorphous and polycrystalline samples over the entire energy range (*i.e.* including low k data).

5.2.2 Types Of Data Analysis

Apart from the different theories described above which lead to various computer programs for analysing EXAFS data, there are also various types of data analysis available for extracting the structural information from the theory used. These may be grouped into two classes: real space and k-space analysis.

(a) Real Space Analysis

Since it was originally pointed out [44] that a Fourier transform of the EXAFS function with respect to the photoelectron wavenumber should peak at distances

corresponding to near-neighbour coordination shells of atoms, this simple technique has been widely used in preliminary analysis due to its speed. The usual method employed is to Fourier transform $k\chi(k)$ with respect to $\exp(-2ikR)$, although the transform is sometimes taken with respect to $\sin(2kR)$ to produce the imaginary part of the transform. The multiplication of $\chi(k)$ by k before transformation removes the $1/k$ factor in equation 21. Since a constant amplitude function gives a sharper Fourier transform, the spectra may often be weighted by k^n (where n = an integer) before transforming to counteract the decreasing amplitude of $\chi(k)$ with increasing k which arises from the factors $|f_j(k,\pi)|$ and $\exp(-2\sigma_j^2)$.

The result of the Fourier transform with respect to $\exp(-2ikR)$ is a series of peaks corresponding to shells of atoms. However, these coordination shells may overlap and be hard to resolve. A criterion has to be chosen to decide when the average position of a given atom is far enough away from that of other atoms to warrent classifying them as separate shells. This definition depends on the band pass of the experiment. If more than one atomic species is present and approximate interatomic distances are known (either from standard samples or, for some samples, the sum of covalent atomic radii) then differing atomic types can be assumed to be in different coordination shells although they may be at physically similar distances from the atom under observation.

Structural information may be obtained by performing a detailed fit to the Fourier transform and this type of analysis has been developed and described by Hayes [69]. Although the speed and simplicity of the Fourier transform are advantageous, along with its ability to handle non-Gaussian peak-shapes, the peaks are shifted from the true interatomic distances due to the effects of the extra phase $2\delta + \psi$, which depends on both the central and scattering atoms and is a function of k, since:

$$2\delta + \psi \simeq ak + b \tag{23}$$

where a and b are constants.

Tables of calculated scattering phases and amplitudes [70] can be used to improve the analysis by weighting the experimental spectrum with the calculated backscattering amplitude and taking the Fourier transform with respect to $\exp(-2ikR - 2\delta - \psi)$ using calculated phases. Using scattering phases calculated for the atomic species in the first coordination shell puts peaks due to this element at their correct distances, but those due to other elements remain shifted to some extent. Weighting by $|f(k,\pi)|$ removes distortions in the peak shape which arise from the energy dependence of this function. The Debye-Waller factor also depends on energy and will result in a broadening of peaks in the Fourier transform and a loss of information contained in the higher energy signal. Further problems may also be caused by truncation effects due to the finite data range, though these may be reduced by use of a window function.

(b) k-Space Analysis

This, more common, type of data analysis relies on fitting to the raw experimental EXAFS spectrum in k-space. This involves calculating the EXAFS function (χ) for an assumed set of structural parameters and adjusting these until a best fit to the experimental data is obtained. This is usually done shell by shell, assuming that the shell contributions are independent. This assumption is valid if the Fourier transform peaks are well separated, but if they overlap significantly then there will be an interaction between shell contributions and the structural parameters obtained will be correlated.

If the Fourier transform peaks do not overlap, it is possible to separate different shell contributions by a method known as Fourier filtering. This involves Fourier transforming the spectrum with respect to $\exp(-2ikR)$, choosing a single peak in the real space spectrum and backtransforming only this peak to k-space. Such a filtered spectrum taken from a standard sample may be used to obtain empirical forms of the phase and amplitude factors in the EXAFS equation, which may be used in place of the calculated values.

Hence, k-space analysis yields detailed structural information when used with accurate scattering data and avoids the problems associated with a finite energy range that occur in real space fitting. However, it can be rather slow computationally.

5.2.3 Obtaining Structural Information From The Raw Data

All EXAFS data collected for this thesis were analysed using computing facilities available at the SERC Daresbury Laboratory. Transmission data from beamlines 7.1 and 9.2 were energy calibrated by the EXCALIB program [71]. This program also allows the summing of series of spectra and the editing of glitches and discontinuities. Summation of the energy calibrated spectra produced by beamline 3.4 was performed using the general graphics package, PLOTEK.

Normalisation of the EXAFS spectra was performed using the EXBACK program [71]. This determines the edge energy and fits low-order polynomials to the smooth atomic absorption backgrounds (μ_0) of the pre- and post-edge data (see figure 5.5) and subtracts these to leave the EXAFS function (see equation 17). The edge was assumed to occur at the energy of the principal maximum in the first derivative of the raw data. A first-order polynomial was usually used for the pre-edge and, if possible, a third-order polynomial for the post-edge. A Fourier transform of the background

subtracted plot could be performed to gauge the accuracy of the fitted background.

Structural information from the normalised spectra was obtained using the EXCURV88 interactive analysis program [67]. This k-space analysis package uses a non-linear least squares routine to fit an assumed set of structural parameters to the experimental spectra. The theoretical fits obtained are calculated according to the fast curved wave theory (see section 5.2.1 (c)), though the small atom approximation is available for interactive multiple scattering calculations.

According to information entered into the program by the user, certain terms from EXAFS equation 21 are calculated, while others are to be determined by the analysis. For successful application of the theory, it is necessary to use a reliable set of scattering phaseshifts $(2\delta + \psi)$. The backscattering factor, $f(k, \pi)$, is dictated by the potential of the scattering atom which itself is determined by the charge density about each atom and is assumed to be spherically symmetric about each atom centre. A further assumption made is that the system's total potential is the sum of so-called Muffin-tin potentials, where the spherical potentials of neighbouring atoms do not overlap and a constant potential exists between them. The phase of the backscattering factor (ψ), which describes the refraction of the electron by the scattering atom, can affect EXAFS spectra by shifting the effective scattering centre of the atom; hence an accurate calculation of the scattering phaseshifts is needed to assess the position of the centre of the atom precisely. Values of tabulated atomic charge densities can be used to calculate the phaseshifts associated with the central atom (δ) and scattering atom (ψ) by a modification of the MUFPOT program contained within the EXCURV88 program, though the default values of the Muffin-tin radius, constant potential term *etc.* can be altered by the user if required.

While the outgoing wave only has a single angular momentum value, scattering

gives rise to several components of angular momentum whose origin is the scattering atom. Each of these will produce an associated phaseshift and the combination of these phaseshifts produces both the amplitude and phase of the backscattering factor (represented as $|f(k,\pi)|$ and ψ in equation 21). Thus the program needs to calculate as many phaseshifts as there are contributing angular momentum components. The default of 13 was usually used, since this proved sufficient to return accurate interatomic distances for the standard samples tested. The scattering phaseshifts can be calculated in a straightforward way, but the central atom introduces the additional complication of its core hole. This tends to draw in the electronic charge in much the same way as an extra positive atomic charge would. For this reason, central atom phaseshifts were approximated as those of the atom having the next highest atomic number to the atom being considered *i.e.* z+1. The central atom contribution to the total phaseshift is written as 2δ since the photoelectron is affected by the central atom potential on its way out and back. (Although the returning photoelectron is actually represented as more than one component of angular momentum with respect to the scattering atom, only that component that is directly backscattered to the centre of the excited atom needs to be considered with respect to this atom; hence the simple factor of 2 can be applied.)

Since inaccuracies in the combined phaseshift $(2\delta + \psi)$ would lead to incorrect interatomic distances, the calculated phaseshifts for each element were first used to fit to the spectrum of a standard sample containing that element (often a crystalline or amorphous form of the element) which had been taken during the same experimental run to avoid the problem of long-term instrumental instabilities. By fixing interatomic distances associated with the standard at their known, tabulated values and then fitting to the spectrum, empirical coefficients for modification of the phaseshifts

(essentially additional coefficients in equation 23) could be returned by the program. It was frequently found that the calculated phaseshifts required modification and also that the magnitude of these modifications varied between experimental runs on the same instrument, necessitating the measurement of a standard sample to be taken during each run. Where possible, the transferability of the modified phaseshifts was tested on other standard samples containing the appropriate elements in different chemical environments to the original standard.

The calculated scattering phaseshifts relate only to elastic scattering, the effects of inelastic processes giving rise to the correction factors in equation 21 as described in section 5.1.2 and 5.1.3. These factors are included in the fitting procedure by the terms VPI and AFAC. VPI is the constant imaginary potential representing the photoelectron lifetime, and AFAC is an amplitude factor describing the proportion of events that result in EXAFS. The imaginary part of the photoelectron energy is usually considered as a free parameter, though its physical range is limited and usually lies between -1 and -6eV, being of higher magnitude for metallic samples than for insulators. For experimental fits in this thesis, VPI was initially set at the value dictated by a fit to the standard sample, and then floated about this point. AFAC was always fixed by reference to a standard sample with the same central atom, since this term is highly correlated with the coordination number to be determined by the fit, and was generally found in the range 0.4 – 0.8. A further non-structural parameter that has to be included in the fitting process is the threshold energy, $E0$. This represents the difference between the position of zero wavevector ($k = 0$) and the as-determined position of the absorption edge. Hence, the $k = 0$ point is taken as offset by a value $E0$ below the absorption edge. This parameter is generated within the fit, but usually lies in the range 0 – 20eV. Apart from $E0$,

the main variable fit parameters are the interatomic distance (R), the coordination number (N) and the Debye-Waller term ($A = 2\sigma^2$).

All of the EXAFS data analysis presented here was performed in k-space, usually using k^3 weighting of the spectra; however, the modified, weighted Fourier transform method (see section 5.2.2 (a)) was used to observe the real space fit and also in presentation of the data. In these cases, Gaussian windows were used for the Fourier transform. Fourier filtering and back transformation was also available for removing residual background or smoothing noisy spectra, but this was avoided unless absolutely necessary.

In summary then, the EXCURV88 program uses a least squares routine to search for a best fit to the fast curved wave theory by varying one or more of the basis parameters, as requested by the user, until a minimum in the square error is obtained. This is done interactively, optimizing R, N and $2\sigma^2$ for each shell of atomic number set by the user. The fitted values of these parameters constitute the structural information obtainable from the EXAFS data.

5.2.4 Error Estimation

The quality of the theoretical fit to the experimental spectra may be quantified by using a parameter known as the fit index (FI), which is defined as:

$$FI = \frac{1}{100N_{pt}} \sum_{i=1}^{N_{pt}} [(\chi_{theor} - \chi_{expt})k^{wt}]^2 \qquad (24)$$

where N_{pt} = the number of data points and wt = the integral k-weighting factor used.

A statistics package within the EXCURV88 program returns errors on individual parameters; however, the true accuracy of the results is somewhat lower since these

calculations do not consider systematic errors arising from such things as poorly calculated phaseshifts and the uncertainty introduced by the terms VPI and AFAC.

The fit index may be decreased by the addition of a further shell, however each new shell introduces three additional parameters (N_n, R_n and A_n) where n = the number of the shell. Joyner et al. [72] applied a statistical approach to gauge the significance of an additional shell and suggested that for a typical data set of around 200 points the fit index needs to decrease by:

$$\frac{FI_{n+1}}{FI_n} < 0.96 \tag{25}$$

to obtain a 5% level of significance (*i.e.* for the new shell to have a 95% probability of being meaningful). Of course, this statistical test is merely a guideline and must be applied with care; parameters must be, for instance, chemically and physically reasonable.

Since strong correlations often exist between parameters, errors on individual parameters are better estimated by use of the 'mapping' routine available on EXCURV88 which produces contour maps of any two parameters and indicates the 5% limit of significance. These type of error estimates have been used throughout this thesis.

Chapter 6

Experimental EXAFS

All of the EXAFS data presented in this thesis were collected using the Synchrotron Radiation Source (SRS) at the SERC Daresbury Laboratory. The local structure around both the semiconductor and metal atoms were investigated over a range of compositions for each of the systems: a-Si:Ni:H, a-Si:Sn:H and a-Ge:Au.

The results and their interpretation for the three systems are presented in Chapters 7, 8 and 9 respectively. The following section describes the experimental arrangements for collection of this data.

6.1 The Synchrotron Radiation Source

Synchrotron radiation is the smooth, continuous spectrum of electromagnetic radiation emitted by high energy electrons (or other charged particles) when they are accelerated and takes its name from the General Electric Synchrotron where it was first directly observed in 1947 [73]. Particles travelling in a circle at fixed speeds experience a continuous acceleration towards the centre of the circle due to the ever changing direction of the velocity. The large acceleration experienced by relativistic charged particles in curved orbits leads to a spread in emitted radiation stretching from X-rays to the far infra-red region.

Synchrotron radiation has many unique properties including high intensity, wide tunability of energy, high polarization and collimation and a precise time structure which is imposed by the rf acceleration process, which produces bunches of electrons so that the radiation is emitted as a series of discrete pulses.

In a basic synchrotron, the electrons are simply accelerated and ejected; while in storage rings such as the one at the Daresbury Laboratory the electrons are accelerated and then stored at high energy in the ring . At the SRS, electrons are initially emitted from a hot cathode and accelerated to 12 MeV in a linear accelerator (linac). Then a synchrotron booster accelerates the electrons to a peak energy of 600MeV for injection into the storage ring where they are accelerated to a final peak energy of 2GeV by a klystron coupled to the electron beam via rf cavities around the ring. This rf accelerating system also replenishes the energy emitted by the electrons as synchrotron radiation, and hence electrons can be stored for many hours.

The 96m circumference SRS storage ring (figure 6.1) consists of 16 dipole magnets, each of field strength 1.2 tesla, which bend the electron beam through a radius of around 5m leading to the emission of electromagnetic radiation. Each of the 16

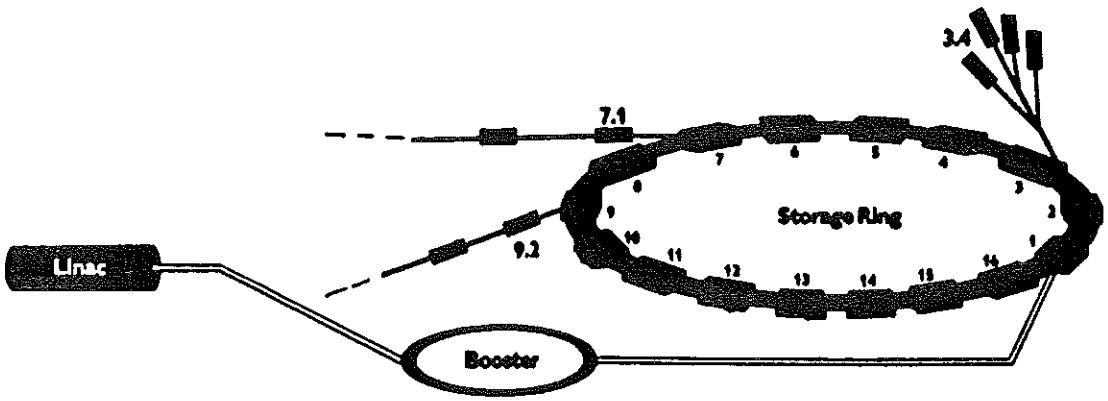

Figure 6.1: Schematic diagram of the SRS storage ring showing only the beamlines used in this study.

straight sections between bending magnets contains 2 quadrupole (focussing) magnets as well as other essential components and additional devices.

In order to prevent the electrons being scattered out of orbit, they are contained in an ultra-high vacuum (10^{-9} - 10^{-10}mbar) maintained by the many vacuum pumps around the ring. The maximum current at the SRS is 375mA, but all data presented here were taken with beam current between 150 and 250mA, the normal operating range.

Additional magnetic devices known as 'wigglers' and 'undulators' can be inserted in the straight sections to impart oscillations of various curvatures and hence shift the peak in the white continuum to shorter or longer wavelengths respectively. At the SRS, a 5 tesla superconducting wiggler magnet produces hard X-rays with wavelengths down to $\sim 0.1\mathring{A}$ (see figure 6.2). Opposing fields before and after this magnet ensure no net deflection of the beam.

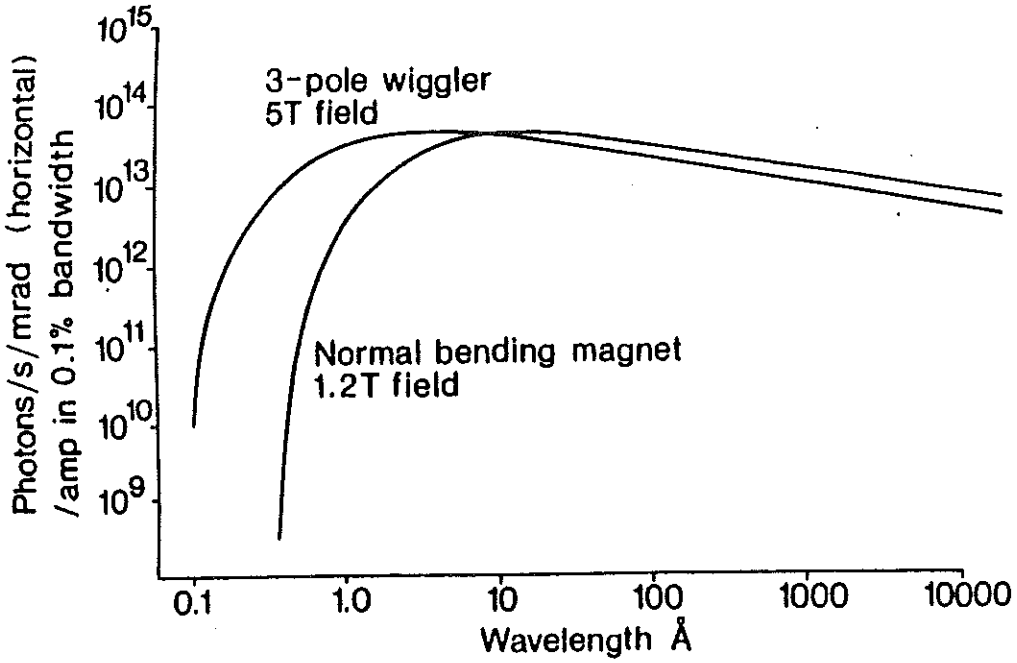

Figure 6.2: Comparison of radiation spectra from wiggler and dipole bending magnets at the SRS [71]

6.2 Beamline Configurations

The synchrotron radiation from the storage ring is directed down evacuated pipes from 'ports' on the storage ring. At the SRS, these are numbered by reference to which of the 16 dipole magnets they originate from. The X-rays can be made available to the experimenter via a number of beamlines that include specific experimental stations –*e.g.* spectrometry, spectroscopy, crystallography, diffraction, topography, interferometry or EXAFS stations. Each beamline will also include a shutter to block off the radiation when not required and the specific beamline optics required for each station.

Of the experimental stations existing or under construction at the SRS, 6 are dedicated to EXAFS (or to its surface equivalent SEXAFS). The 3 EXAFS stations used in this work are described in detail below.

(a) Beamline 3.4

This is the SRS soft X-ray extended absorption fine structure (SOXAFS) beamline. It has a possible X-ray wavelength range for EXAFS of around 3 - 15$\AA$ ($\sim$ 4 to 0.8 keV) using the various monochromator crystals available. In this study it was used to study Si K-edge (1839eV) EXAFS and to make preliminary measurements on the Ar K-edge (3203 eV) of any gas incorporated in the samples during the sputtering process.

This beamline consists of a 75cm long toroidal mirror which is used to focus the beam in the vertical direction and its take-off angle can be adjusted manually to optimise the input signal. Due to the relatively short wavelengths of X-rays, total external reflection for typical mirror materials (which need to be resistant to radiation,

have high thermal conductivity, low thermal expansion and be highly polishable) occurs at low angles of incidence so mirrors need to be comparatively large though, since synchrotron radiation is intrinsically highly collimated, it is not necessary to use a full surface of revolution. In initial measurements a Pt coated quartz mirror was used but, as the UV background was reduced by the addition of filters in the main beam, glitches appeared on the spectra at 2122eV corresponding to the Pt M_5-edge and the mirror was subsequently recoated with Cr. Unfortunately, this reduced the energy cut-off of the mirror and hence the energy range of the beamline to 3500eV at the usual beamline angle of 1.6° from horizontal (0.8° at the mirror). In order to scan the required energy range for the Ar K-edge the beamline angle was altered to 1.5°.

A 9000Å thick C window separates the ultra-high vacuum (UHV) ($\sim 10^{-9}$mbar) region from the high vacuum (HV) ($\sim 10^{-7}$mbar) in the monochromator section and a 7μm Be filter after the monochromator helps cut down UV scatter.

The SOXAFS beamline uses a double crystal, order sorting monochromator (see figure 6.3) with a fixed exit beam. As the parallel crystals are rotated to vary the Bragg angle, and consequently to give a range of output energies, they are also translated to maintain the fixed output position. Order sorting can be achieved by adjusting the pair to be slightly non-parallel so that the narrower higher order reflections are reduced in intensity by a greater amount than the fundamental wavelength. This harmonic rejection was usually set at 70% for both Si and Ar (this notation referring to the percentage of intensity used *i.e.* 70% harmonic rejection corresponds to rejection of 30% of the beam intensity). The first crystal (top) is water cooled and the monochromator has an angular range of 10 – 80°.

InSb(111) crystals, with an energy range of 1680 – 9520eV were used to scan the

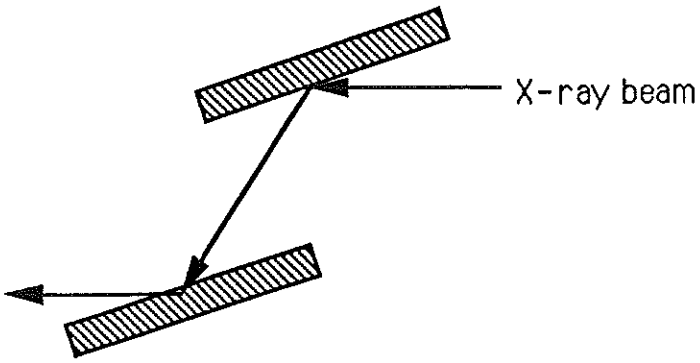

Figure 6.3: Arrangement of crystals a in double crystal monochromator

Si K-edge and Ge(111) crystal with a range of 1920 - 10910eV for the Ar K-edge. The entrance slits to the monochromator were usually set at approximately 3mm to reduce angular dispersion of the beam and therefore increase the energy resolution of the crystals. The monochromator exit slits cut out any vertical scatter of the beam and the slits after the monochromator trimmed the beam horizontally to produce a spot size compatible with the sample. The beam could be seen at various strategic places down the beamline by use of phosphorescent paint.

The beam current after passage through the monochromator Be filter (I_0) was initially monitored with a 7μm thick Be foil, but this was found to produce a very weak signal which was extremely prone to noise and all later scans used a 0.75μm thick Al foil, which also served to further reduce UV components. The I_0 signal could be maximised by adjustment of the top crystal via a motorized micrometer and then a solenoid for finer tuning. Both the I_0 and the signal from the sample were amplified using 427 Keithley amplifiers and then displayed digitally.

After manual adjustment of the crystals to maximise the I_0 signal to the top of

their Bragg peak in each region of the energy scan (scans normally being divided into 3 or more energy regions with variable counting times and energy steps), these intensities are entered into the computer controlled scanning program along with the required harmonic rejection, energy step and count time for each energy region. The peak I_0 values are interpolated by the program and a percentage corresponding to the harmonic rejection is subtracted to generate a reference signal. When control of the monochromator crystals by the solenoid driver is switched from manual to servo mode, the solenoid then tries to follow the reference signal in order to hold harmonic rejection at the constant required level throughout the scan.

The sample chamber was evacuated to $< 10^{-6}$mbar range before opening it to the beam. The sample holder was usually rotated to 30 – 60° to the beam in order to probe a larger area of the sample and hence improve the signal:noise ratio. Since the existing Daresbury Laboratory sample holder was not suitable for the prepared samples, an alternative stainless steel holder was designed and made by the mechanical workshops in the Physics Laboratory at UKC. The position of the sample holder could be adjusted vertically to introduce different samples into the beam. The position of the samples was recorded with respect to a line scribed on phosphorescent paint on one end of the holder. Special care was taken to avoid contaminating the surface of the samples with this paint or any other impurities. Protective gloves were worn during all preparation and sample loading. EXAFS detection was possible via transmission, electron yield or fluorescence (see section 6.1.3).

(b) Beamline 7.1

EXAFS beamline 7.1 (see figure 6.4) has a working energy range of approximately

4 – 14 keV by employment of an order sorting, double crystal monochromator (as described above) with double Si(111) crystals or a single channel-cut Si(111) crystal. The two crystal arrangement was used in this work to examine the Ni K-edge (8.33 keV), the Ge K-edge (11.1 keV) and the Au L_3-edge (11.9 keV) environments. Operation and control of monochromator crystals and harmonic rejection of 50% via a servo lock-in system was similar to that previously described and was controlled by station software.

This beamline uses a 60cm long Pt coated vertical focussing toroidal quartz mirror. Pt is a commonly used coating material for higher X-ray energies since the shorter wavelengths require lower angles of incidence for total external reflection and the more electron dense a material the higher its critical angle will be.

A set of entrance slits defines the horizontal and vertical extent of the white beam entering the monochromator, while a set of exit slits define the size of the monochromatic beam at the sample and reduce scatter. The monochromator and slit vessels are kept under a rough vacuum and a Be window separates this from the rest of the beamline which is open to air. For safety reasons the whole beamline is contained in a interlocked hutch.

The I_0 intensity was measure by an Ar/He gas ionisation chamber and could be maximised for reference in a similar way to that described in (a). Samples were held in a simple clamp situated after the I_0 chamber. The beam position was determined by photography. Detection of the EXAFS on this station was achieved in transmission using a further Ar/He ionisation chamber.

(c) Beamline 9.2

This beamline is closely similar to beamline 7.1 but being situated on the wiggler line (*i.e.* line 9) experiences higher energy X-rays. The order sorting, double crystal monochromator containg Si(220) crystals gives a theoretical energy range of 3.3 – 18.6KeV for 80 – 10° Bragg angles. For observation of the Sn K-edge at 29.2 keV, the monochromator was at the limit of its energy range ($\sim 5°$) resulting in low intensities and a relatively poor signal:noise ratio for the transmission data. Si(400) crystals with a energy range up to 32.8 keV for an 8° Bragg angle would have improved this problem, but these were not available. The possibility of investigating the Sn L_3-edge was ruled out due to the small L_3 – L_2-edge energy gap ($\sim$ 200eV).

Details of monochromator and sample stage are the same as for 7.1 and maintenance of the harmonic rejection of 70% during a scan is similar to that previously described. The I_0 signal was monitored using a Kr/He ionisation chamber for this energy range.

On each beamline, data were stored on a Winchester disc and transferred to the SRS mainframe computer ready for analysis.

6.3 Types of EXAFS Detection

X-ray absorption experiments necessitate measurement of the sample absorption as a function of energy. This can be done directly by measuring the attenuation of the incident beam in a transmission experiment, or indirectly by measuring the products of absorption such as fluorescent radiation or emitted electrons. Regardless of the detection scheme, it is necessary to monitor the incident intensity (I_0) in order to remove the effect of a varying source intensity, and this must be done in a manner that depletes the incident intensity by only a small fraction. Three types of EXAFS detection were used in this study:

(a) Transmission EXAFS

As the name implies, sample absorption in the transmission mode is investigated by measuring the incident (I_0) and transmitted (I_t) X-ray intensity with varying energy. Since, from equation 18:

$$\ln \frac{I_0(E)}{I_t(E)} = \mu_{total}(E)t$$

where t = sample thickness and μ = total absorption coefficient of the sample.

Figure 6.4 shows a general experimental arrangement. Incident and transmitted light intensity are measured by the first and second ionisation chambers respectively. These consist of a gas or mixture of gases held between two thin windows and containing two electrodes, and work on the principle of measuring photo-ion current. For optimum performance, the attenuation of the first ion chamber is set at around 20% and the second to around 80%. This is achieved by filling the detectors with the appropriate gas mixtures for the energy range under investigation. Transmission experiments were performed on beamlines 7.1 and 9.2, where the gases used in the ionisation chambers were argon/helium and krypton/helium respectively (the helium being used to increase the total pressure to atmospheric).

Apart from the fraction (f) of incoming beam lost in determining I_0, one of the main influences on experimental accuracy in transmission mode is the sample thickness (t). Minimizing the noise:signal ratio in the transmitted intensity with respect

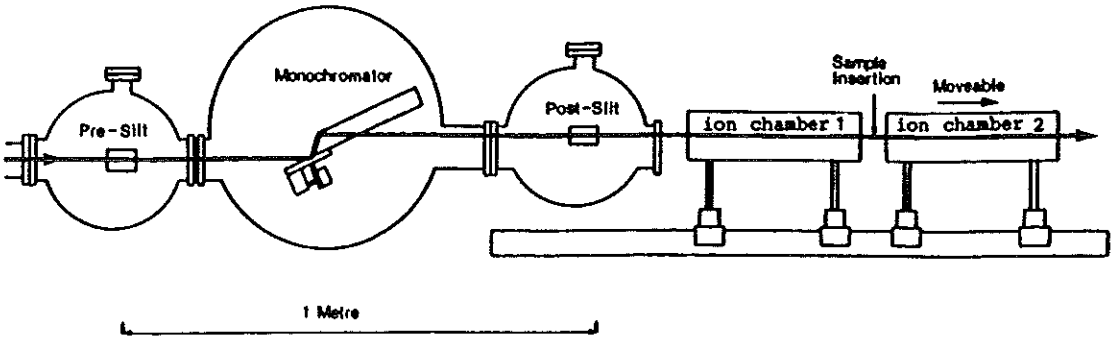

Figure 6.4: Schematic layout of experimental arrangement for measuring EXAFS in transmission mode [74]

to f and t gives f=0.24 [75] (*i.e.* first ionization chamber set to $\sim$ 20% attenuation) and μt=2.55, while ignoring the intensity absorbed by the I_0 detector gives μt=2 [76]. The linear absorption coefficient (μ) at the edge energy (E_{edge}) can be calculated in m^{-1} by:

$$\mu \simeq \frac{\rho\sigma(E_{edge})}{Mm_N}$$

where ρ = weighted average density of sample in kgm^{-3}

$\sigma(E_{edge})$ = weighted average absorption cross-section at energy E_{edge} in m^2atom^{-1}

M = weighted average molecular weight of sample in a.m.u.

m_N = mass of a neutron in kg.

In this way, sample thicknesses for the concentration ranges to be prepared were

calculated before preparation and, depending on the metallic concentration, were determined to be in the ranges:

a-Si:Ni:H	Ni K-edge	100 - 165μm
a-Si:Sn:H	Sn K-edge	200 - 1000μm
a-Ge:Au	Ge K-edge	16 - 22μm
a-Ge:Au	Au L_3-edge	12 - 21μm

In view of the large thicknesses required for some of the samples, it was necessary to deposit several 1 - 2μm thick samples at each composition and stack them for transmission experiments. Samples were deposited on 0.02mm thick polypropylene substrates which would not absorb or attenuate the beam significantly at these energies, and could also be folded to increase sample thickness, thus reducing the number of samples of each concentration that needed to be prepared.

Thickness effects account for most of the amplitude distorting factors in absorption measurements. These effects occur whenever some part of the incident beam is not attenuated by the sample or is at a different energy from the primary radiation. The former occurs if the sample contains pinholes, so the multiple stacking of samples also helps reduce this effect considerably. The latter case can be caused by higher-order harmonics passing through the monochromator, so care must be taken to eliminate these before the sample. A similar problem may be caused by the emission of fluorescent photons by the sample on absorption of the X-rays. If these photons are detected then the measured absorption is effectively reduced, so the detector solid angle needs to be small enough to eliminate this.

These effects are small for thin samples, but become a large fraction of the total signal for thicker samples. Since the reduction factor is proportional to μt [75], if

the statistically optimum value of $\triangle\mu t = 2.55$ ($\triangle\mu$ = edge-step) is used, then even small effects can result in serious amplitude reduction. However, it is found that with reasonable care, the distortions usually become negligible when $\triangle\mu t < 1.5$, and since the noise:signal minimum is broad, this does not significantly degrade statistics. In this study all transmission samples were stacked to give $\triangle\mu t = 1 - 2$.

To enable calibration of the measured phases and amplitudes, data from standard samples were collected for each edge. The standard edge was chosen to match the environment of the sample edge as closely as possible, and in the absence of a suitable compound, a standard spectrum of the crystalline or amorphous edge element was taken.

The possibility of using transmission to study the Si K-edge was investigated and $1.5 - 3.0\mu$m thick samples were deposited on 0.025mm thick beryllium foils. However, difficulties caused by bad adhesion of the sputtered samples and handling of the Be foils led to the use of more suitable detection techniques.

(b) Total Electron Yield EXAFS

The absorption of an X-ray photon can result in several processes (see figure 6.5) including the emission of Auger electrons and fluorescent X-rays. These are competing processes and their relative strengths depend on the atomic number of the absorber. For heavy atoms fluorescence is the dominant process but for atoms with K-edges below about 2 keV and for the L-edges of most atoms, Auger emission is predominant. The Auger emission is atom-specific with a fixed kinetic energy characteristic of the binding energies of the levels involved. The number of electrons (γ_{Auger}) per incident photon created in a depth L of a solid with absorption coefficient μ is given by:

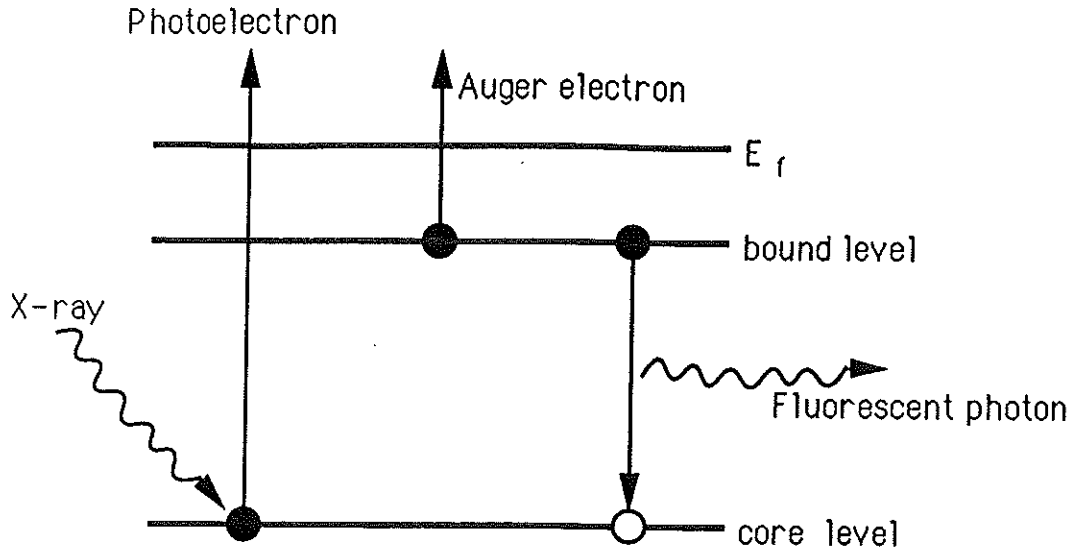

Figure 6.5: Schematic diagram of the possible processes resulting from absorption of an X-ray by an atom

$$\gamma_{Auger} \propto 1 - \exp(-\mu L) \tag{26}$$

But for photon energies h$\nu \geq$ 100eV the photon absorption coefficient $\mu \leq 1 \times 10^{-2}\mathring{A}^{-1}$ [77] and since direct Auger electrons originate within $\sim 50\mathring{A}$ of the surface (see figure 6.6) L $\leq 30\mathring{A}$ so $\mu L \ll 1$ and thus:

$$\gamma_{Auger} \propto \mu L \tag{27}$$

Since the electron yield (γ) is proportional to μ it can be used as a measure of the photon absorption (μ) *i.e.* EXAFS. Because of the large probability that an Auger electron will undergo inelastic collisions, an electron detector tuned to the

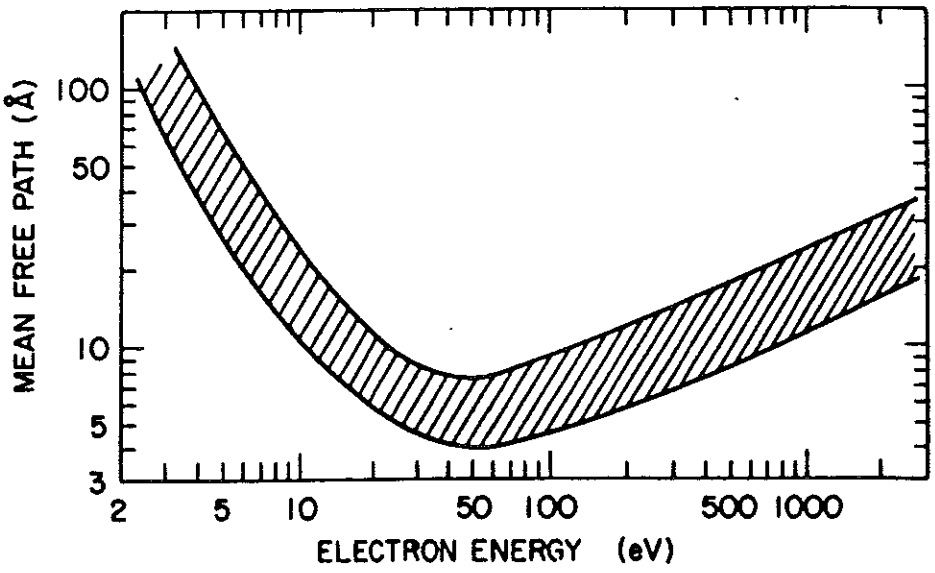

Figure 6.6: Electron mean free path in most solids as a function of electron kinetic energy [78]

energy of the Auger electron will effectively result in a surface investigation ($\leq 50\mathring{A}$ depth). To study the bulk sample (effectively up to $1000\mathring{A}$ depth) the scattered Auger electrons must also be included and hence the band pass of the detector must be opened. This will result in detection of the total electron yield which will consist of photoelectrons, secondary electrons induced by electrons ejected into the sample and a small contribution from electrons induced by fluorescent X-rays as well as the inelastically scattered electrons and directly ejected Auger electrons. If these electrons are emitted simultaneously (with respect to the detector time resolution) then as long as each absorbed photon produces at least one electron that reaches the detector, the counting rate can be assumed to remain proportional to the absorption *i.e.* $\gamma_{total} \propto \mu L$.

Since the absorption of the X-ray photon must result in the emission of a photoelectron, the detection of these electrons could also be used to measure μ; but the angular distribution of the photoelectrons varies as the photon energy is increased, thereby superimposing an energy-dependent 'background' onto the EXAFS unless the photoelectrons are collected over a full 4π solid angle. As this detection geometry is impossible in practice, electron total yield which involves a minimum solid angle of detection of 2π, seems the more reliable method.

However, for the high signal levels encountered in many experiments, electron detectors will saturate and the total yield signal is often performed via a current measurement rather than a counting chain. On beamline 3.4, the method of electron drain current (*i.e.* measurement of the electron drain needed to earth the sample after emission of the electrons) was used. This requires the use of electrically conducting substrates (and preferably a reasonably conducting sample — see (c) below) and so all $1 - 2\mu$m thick samples for Si- or Ar-K edge investigations were deposited on stainless

steel. This substrate material was chosen not only for its good conductivity and good sample adhesion, but also for the fact that it contained no elements with absorption edges in the range under investigation to eliminate the possibility of enhancing the yield signal at specific energies with electrons from the substrate via any pinholes in the sample. The thickness effects from such pinholes are negligible due to the small values of $\triangle\mu t$ for the samples.

Since the detection of the yield signal by a current measures the total number of electrons emitted as opposed to the total number of absorption events, the constant proportionality of the yield signal to the absorption is not necessarily assured. In particular, the photoelectron energy is a function of the incoming photon energy, resulting in an energy dependence for the average number of emitted electrons per photon absorption and hence possible amplitude distortions in the EXAFS. As the energy of the incoming photon increases, so will the kinetic energy of the emitted photoelectron making more energy available for secondary processes; however, the associated decrease in the electron absorption cross-section will reduce the probability of such processes. Similar arguments hold for the measurement of the I_0 signal, but the dependence of these effects on the physical parameters of the materials involved means that any deviations in the I_0 spectrum do not cancel those from the sample. Coupled to the unknown energy dependence of the photoelectron emission angle, all these factors combine to make the exact amplitude deviations of the total electron yield EXAFS difficult to predict. In an attempt to reduce the effect of such distortions, standard samples were measured, using the same technique, in order to compare relative amplitudes.

Although the assumption of an energy independent electron yield seems to work reasonably well for many cases, the possible amplitude deviations indicate that full

EXAFS information may not be extracted from the fine structure (though it does contain the important interatomic distance information) and a detailed investigation of the energy dependence of the total electron yield technique is required.

(c) Fluorescence EXAFS

As previously mentioned, after creation of a core hole by the emission of a photoelectron the excited absorbing atom can relax by X-ray fluorescence (see figure 6.5). As in the total electron yield case, if the fluorescent yield is assumed to be energy independent, the intensity of the fluorescent signal becomes proportional to the absorption process and hence can be used to measure EXAFS.

Since Auger electron emission is a more dominant process than fluorescence for K-edges below $\sim 2\,\mathrm{keV}$ the former was chosen to study the Si K-edge. However, the total electron drain current method employed required conducting samples and where this was not possible (*e.g.* SiO_2 as a standard sample) the electron yield signal was weak and the fluorescence technique was employed on beamline 3.4. Non-conducting samples were contacted onto conducting substrates to minimise sample charging effects and rotated to obtain the optimum fluorescence signal. Detection of the fluorescent photons was achieved via a photomulitiplier tube perpendicular to the incoming X-ray beam.

As for total electron yield, thickness effects are minimal for fluorescence measurements because the sample $\Delta\mu t$ is low due to the relatively small sample thickness needed. However, corrections must be made for the self-absorption of fluorescent X-rays and experimentally this confines the use of fluorescence detection to dilute systems (and equivalently, thin concentrated samples) where it is more efficient than

the conventional transmission experiment [79, 80]. Fluorescence is also useful when the sample is too absorbing or not macroscopically homogeneous enough for transmission, and since the fluorescent yield increases with atomic number it is more likely than Auger electron emission for heavier elements. However, consideration of the aforementioned advantages and disadvantages compared to the other techniques available led to the rejection of fluorescence for the study of any of the edges of the main systems studied.

The effect of self-absorption on EXAFS experiments can be clearly demonstrated in comparing the Si co-ordination number of 1.4 nearest neighbours given by the fluorescent yield of the Si K-edge of the c-SiO_2 sample with the correct value of 4 given by the total electron drain current method. This highlights the importance of standard samples for amplitude correction. As well as the differing amplitude considerations for techniques (a), (b) and (c), it is often found that data taken at different times on the same apparatus using the same technique have different amplitudes. If thickness effects are ruled out the most likely cause is differing energy resolution. Therefore, for comparison of data it is important to measure samples on the same apparatus, preferably at the same time and definitely to take at least one type of standard sample measurement.

Chapter 7

Amorphous Silicon:Nickel:Hydrogen Thin-Films

7.1 Introduction

While several optical and electrical-based studies have been performed on the a-Si:Ni(:H) system, no known direct structural investigations have been undertaken, although the structure of a-Ge:Ni has been the focus of both neutron diffraction [81] and EXAFS [82] studies. Here, both sets of authors report evidence for an a-Ge tetrahedral network up to around 10at.% Ni and suggest that the metal enters this structure substitutionally. The structure is assumed to approach a dense random packing (DRP) model at high metal concentrations; while in the region of the a-Ge:Ni MIT (23 – 30at.% Ni) a strong interaction between metal and metalloid atoms and a modified intermediate structure somewhere between a TRN and DRP is suggested

for the system.

Early conductivity work on micro-crystalline Si:Ni alloys [83] reported that the MIT occurred at 13at.% Ni. Crude electron diffraction data on this work reported for this work indicated grain sizes of 10 – 20nm and also suggested that the impurity atoms primarily occupied substitutional sites, although the possible existence of small grains of an undetectable second phase were not ruled out. The assumption of a microscopically homogeneous system led to the interpretation of the MIT as being of the Anderson type (see Chapter 3).

Later work on amorphous but unhydrogenated sputtered Si:Ni [84] indicated that the electrical conductivity was increased by up to 7 orders of magnitude over that of the intrinsic semiconductor for as little as 5at.% Ni content. In this report, electrical measurements appear to have been taken using a 2-probe gap-cell geometry (where electrode resistance would begin to become significant for the higher conductivity samples) implying that the increase could be even greater. The authors also investigated the effect of hydrogenation and Ar gas pressure during co-sputtering of the samples. They concluded that while the effect of hydrogen is not as large for samples doped with transition elements as for those doped with elements inducing shallow impurities, the value of the conductivity is affected quite considerably by the Ar pressure used during film deposition; highlighting the fact that only *qualitative* comparisons can ever be made between samples prepared under even slightly differing conditions. No MIT was expected, or observed, in the concentration range investigated (0 – 10at.% Ni) and the variable range hopping relation (see section 3.4) was obeyed below room temperature for all samples. The authors suggest that this conduction process remains dominant up to increasingly higher temperatures on the

addition of more nickel due to the hopping of electrons through Ni atom sites below and near the intrinsic Fermi level. Above room temperature, annealed samples showed a thermally activated type of conduction (*i.e.* $\propto 1/T$) with the result that the two conduction mechanisms (thermally activated and variable range hopping) may be present in this temperature region. Although reporting, in a slightly earlier paper [12] covering part of the same work, that the thermoelectric power for samples containing transition elements becomes so small that it is difficult to obtain reliable data and that its sign was found to change from sample to sample, the authors later [84] use these measurements and their change of sign (from minus to plus on addition of Ni) as indicative of the expected presence of deep acceptor levels in the bandgap and hence speculate on their substitutional incorporation.

More recent work [85] on a-Si:Ni:H in the concentration range 0 – ~17at.% Ni also reported a large enhancement of the dc conductivity for small amounts of Ni (up to ~8 orders of magnitude for as little as 5at.% Ni) and $T^{-1/4}$ dependence *i.e.* variable range hopping, at low temperatures. Above 90K, the temperature dependence of the log conductivity was found to follow a T^{-1} law indicating thermally activated transport. However, the surprising conclusion is that there is no MIT in this composition range whereas, assuming the microscopically homogeneous structure produced by random substitutional incorporation of the Ni atoms, an Anderson transition would have been expected on the basis of earlier results [83]. However, given that Ni is reported as having one of the fastest diffusion rates of all metals in silicon [86, 87] and that the sputtering process enhances surface diffusion during deposition due to secondary bombardment of the substrate by the ionised sputtering gas, it is probable that clustering of metal atoms will occur. In this case, any MIT that occurs in such a system may not be of Anderson type.

While it remains debatable which structural model is correct for such systems, exactly how the Ni impurity atoms are incorporated into the a-Si matrix is of obvious importance to the understanding of the conduction process. This chapter presents EXAFS and supporting data on the structure of a-Si:Ni:H over the composition range where a metal-insulator transition might be expected to occur.

7.2 Sample Preparation and Characterization

Thin-films of a-$Si_{1-x}Ni_x$:H were prepared by rf reactive co-sputtering as described in Chapter 4. The deposition parameters used were those given in Table 4.1 and the metal content of the samples was altered by varying the number of 99.98% pure Ni or 99.0% pure $NiSi_2$ discs placed on the c-Si target.

Initial microstructural determination by SAED transmission electron microscopy (section 4.2.1) did not indicate crystallinity in any of the samples (see figure 4.4 and 4.5). All films were found to be in the region 1 – 2μm thick using a Talysurf (section 4.2.2).

Sample composition, via energy dispersive electron microprobe analysis and $^4He^+$ Rutherford backscattering (section 4.2.3), was found to be uniform ($x\pm$ 0.02) over the film area for any particular sample. In addition to Si and Ni, immediately after deposition each sample was found to contain approximately 8at.% Ar, incorporated during the sputtering process.

An initial series of dc 'dark' conductivity measurements was undertaken and later extended in a parallel study at the University of Leicester using the same samples. Figure 7.1 [88] shows the room temperature dc conductivity of a-$Si_{1-x}Ni_x$:H as a function of x. A dramatic increase in conductivity, compared to that of undoped a-Si:H, is obtained on the addition of a few percent Ni. These results show good qualitative

agreement with those of Shimizu et al. [84] and Rogachev et al. [85], any quantitative differences possibly being due to differing preparation conditions or sample composition determination methods. Data collected over the range ~77 – 475K showed a T^{-1} dependence of the log conductivity, with activation energies indicative of thermally activated hopping conduction. A metal-insulator transition would be indicated in figure 7.2 [88] by the conductivity becoming essentially temperature-independent. This is hard to determine from figure 7.2, but the smooth decrease and finite values of activation energy obtained from least squares fits to the plots indicate that there is no MIT in the $0.03< x <0.26$ region. It is possible that the MIT occurs below x=0.03±0.02 (where it is difficult to produce accurate compositions by sputtering) accounting for the large increase in conductivity with low Ni concentrations. Structural results will be discussed in view of this possibility. Alternatively, the MIT may not have been reached by 26at.% Ni, but in the absence of more conclusive electronic data (such as thermopower or very low temperature conductivity measurements) it is difficult to speculate. Recent optical work at the University of Leicester on 'in-house' samples [89] indicates an MIT at ~26at.% Ni using the E_{04} method (*i.e.* representing the optical gap as the photon energy at which the absorption coefficient is $10^4 cm^{-1}$) for determining the optical gap. However, on using the Tauc gap definition of the optical gap, a transition point is not defined. It should also be noted that preparation conditions and sample composition determination may again produce quantitative differences in the determined position of the MIT.

7.3 EXAFS Results

Extended X-ray absorption fine structure data from both the silicon and nickel K-edges of a-$Si_{1-x}Ni_x$:H were collected for samples in the composition range $0< x <0.3$

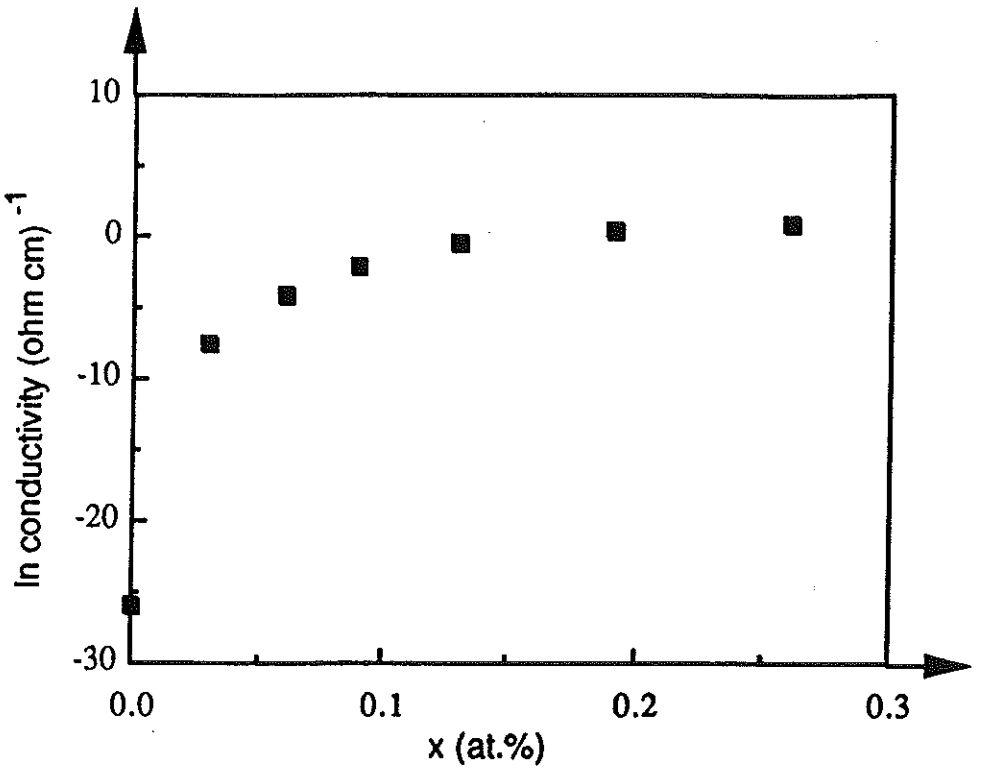

Figure 7.1: Room temperature dc conductivity of a-Si:Ni:H as a function of Ni content

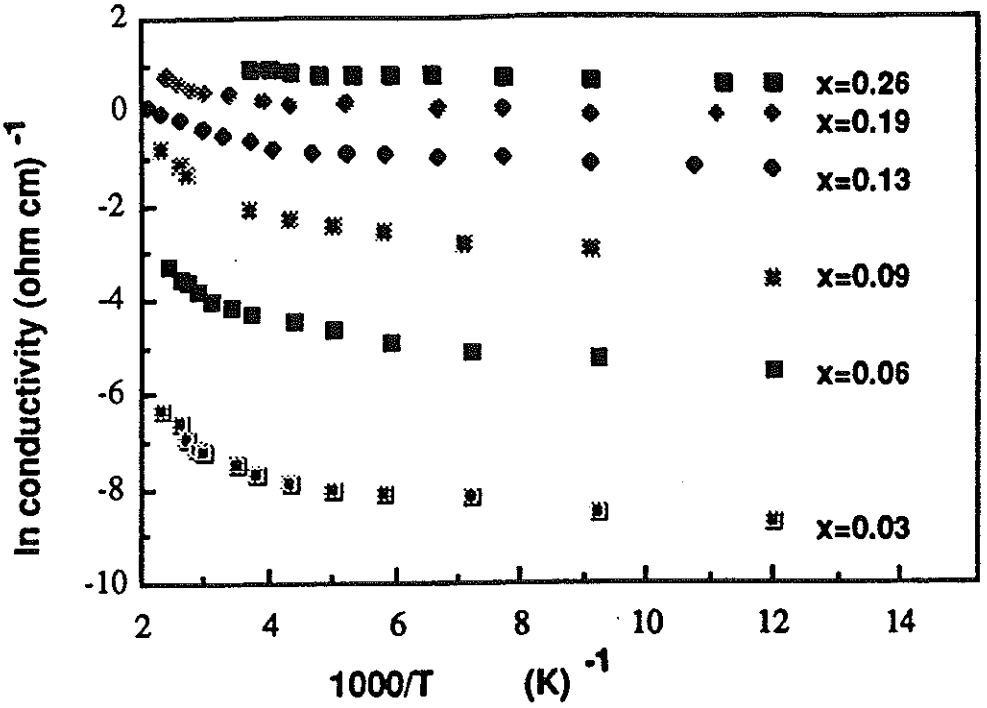

Figure 7.2: dc conductivity as a function of temperature for a-$Si_{1-x}Ni_xH_x$

using SRS beamlines 3.4 and 7.1 respectively (sections 6.2 and 6.1) at the SERC Daresbury Laboratory.

Si-edge measurements were taken using the electron drain current method using 1 –2μm thick samples deposited on stainless steel substrates. Measurements on the Ni-edge were performed in transmission using samples deposited on mylar substrates and several layers of these samples were stacked to obtain the optimum absorption-thickness product at the absorption edge (section 6.3).

Data analysis was performed as detailed in section 5.2.3. Using the criteria of Joyner et al. [72] it was only meaningful to fit one shell to the Si-edge data, but a 2-shell model was justified for the Ni-edge. Fits of the Si $k^3\chi(k)$ and their corresponding Fourier transforms are shown in figures 7.3 and 7.4, while the Ni $k^3\chi(k)$ fits and Fourier transforms are presented in figures 7.5 and 7.6. The summarized results of these fits are shown in Tables 7.1 and 7.2 respectively.

Data from standard samples of c-Si and a-Si:H were collected for phaseshift and amplitude corrections (discussed in Chapters 5 and 6) to the Si K-edge fitting. Fits to the first shell of c-Si or to a-Si:H produced similar phaseshift corrections which were then applied to the phaseshifts used for the unknown sample fits. As these corrections were found to alter between data collection dates (due to systematic variations on beamline 3.4) corresponding to variations in interatomic distances of several hundredths of an Ångstom, standard sample data were therefore taken during each experimental run. The transferability of the corrected phaseshifts were investigated by using them to fit to SiO_2 sample spectra taken during corresponding runs. They were found to produce good fits and accurate interatomic distances.

The amplitude factor (AFAC), which is dependent only on the edge under investigation, was set to the standard sample value, which was determined to be 0.7. The

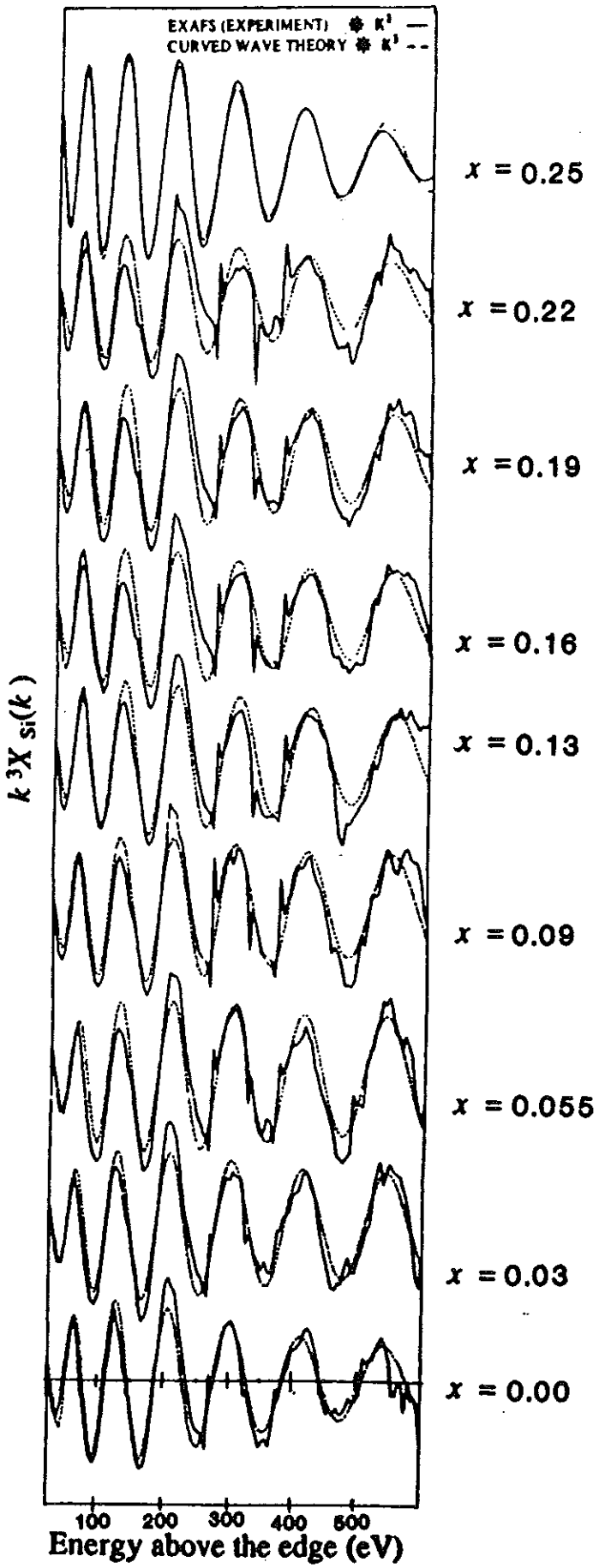

Figure 7.3: Silicon K-edge EXAFS spectra for a-$Si_{1-x}Ni_x$:H.

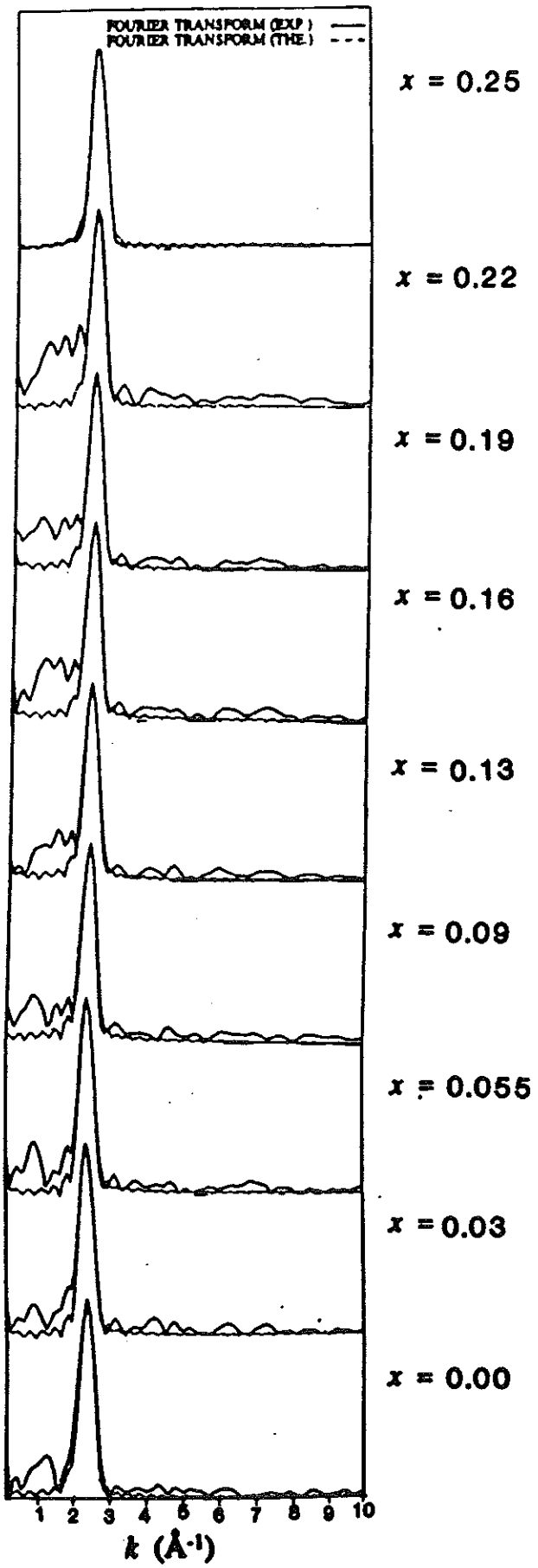

Figure 7.4: Silicon K-edge Fourier transforms for a-$Si_{1-x}Ni_x$:H.

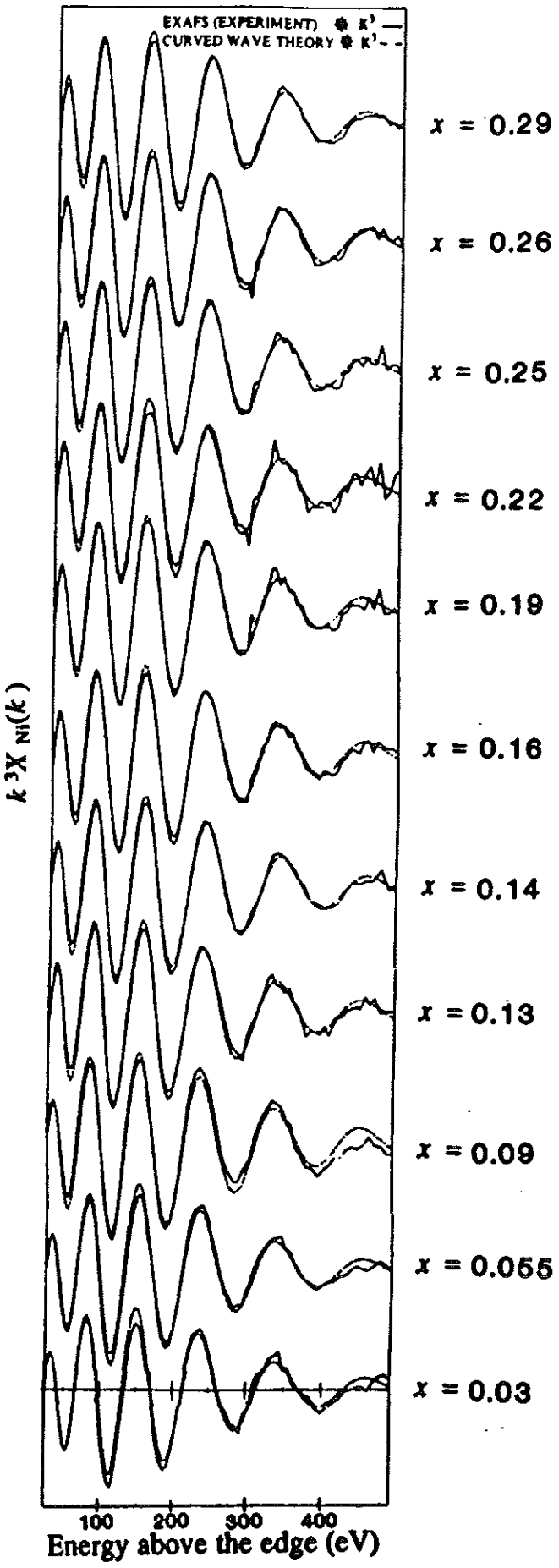

Figure 7.5: Nickel K-edge EXAFS spectra for a-$Si_{1-x}Ni_x$:H.

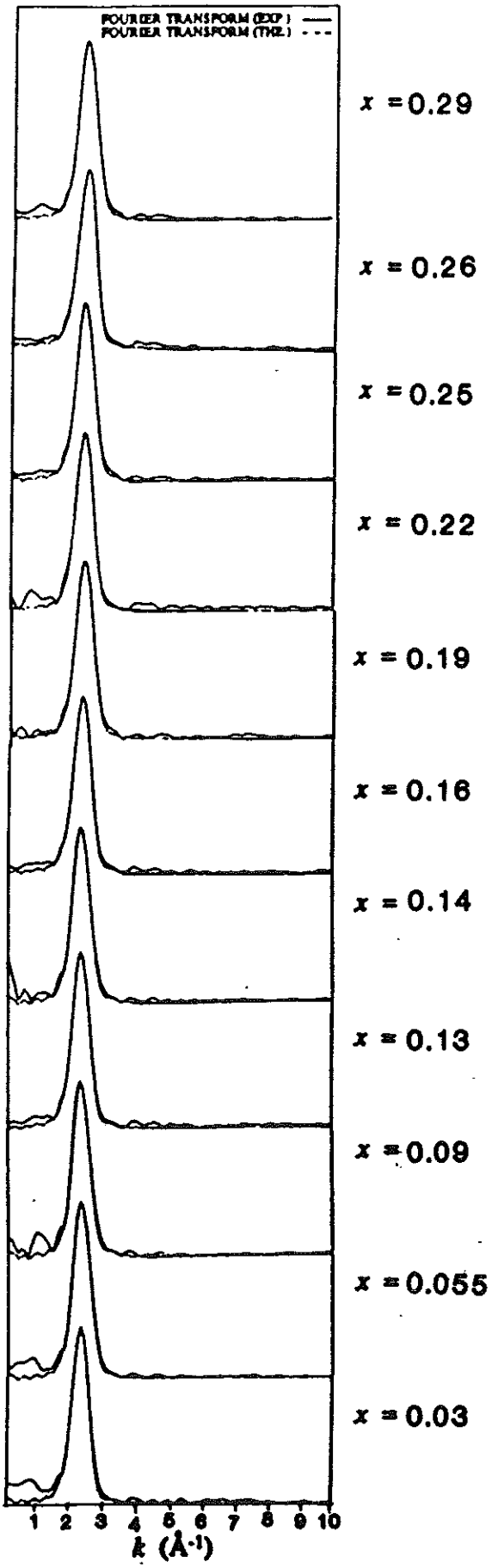

Figure 7.6: Nickel K-edge Fourier transforms for a-$Si_{1-x}Ni_x$:H.

Table 7.1 Silicon K-edge EXAFS results for a-$Si_{1-x}Ni_x$:H

AFAC=0.7

x	$E0$ (eV)	VPI (eV)	N_{Si-Si} (± 0.8)	R_{Si-Si} ($\pm 0.02\AA$)	A_{Si-Si} ($\pm 0.003\AA^2$)
0.00	2.67	-2.00	4.0	2.35	0.007
0.03	3.16	-2.00	3.0	2.35	0.003
0.055	1.64	-2.00	2.6	2.36	0.002
0.09	4.96	-2.00	2.7	2.34	0.003
0.13	4.14	-2.85	3.4	2.34	0.005
0.16	4.34	-2.85	2.2	2.35	0.005
0.19	4.54	-2.84	2.4	2.35	0.005
0.22	2.95	-2.25	1.8	2.36	0.006
0.25	1.25	-1.00	1.1	2.39	0.009

Table 7.2 Nickel K-edge EXAFS results for a-$Si_{1-x}Ni_x$:H

AFAC=0.75

x	$E0$ (eV)	VPI (eV)	N_{Ni-Si} (± 1.0)	N_{Ni-Ni} (± 1.0)	R_{Ni-Si} ($\pm 0.01\AA$)	R_{Ni-Ni} ($\pm 0.02\AA$)	A_{Ni-Si} ($\pm 0.003\AA^2$)	A_{Ni-Ni} ($\pm 0.005\AA^2$)
0.03	10.43	-5.50	7.4	1.5	2.33	2.55	0.019	0.021
0.055	10.44	-5.50	7.5	2.3	2.33	2.54	0.020	0.024
0.09	8.14	-5.50	9.0	4.9	2.37	2.51	0.022	0.039
0.13	7.46	-5.51	9.3	3.5	2.36	2.52	0.024	0.033
0.14	7.89	-5.51	9.1	4.0	2.36	2.52	0.024	0.035
0.16	8.17	-5.51	8.8	3.3	2.35	2.53	0.023	0.031
0.19	9.03	-5.53	8.6	2.8	2.34	2.54	0.024	0.026
0.22	7.88	-5.53	8.7	2.6	2.35	2.54	0.024	0.025
0.25	9.17	-5.53	8.5	2.7	2.35	2.54	0.023	0.026
0.26	8.16	-5.53	8.4	2.5	2.35	2.54	0.022	0.025
0.29	8.69	-5.53	8.3	2.3	2.34	2.55	0.022	0.022

energy offset, $E0$, was found to vary between 1.25 and 4.96eV; while the electron mean free path fit parameter (VPI) ranged from -1 to -2.85eV, being floated from the standard sample value of -2.0eV.

For the Ni K-edge data a standard sample of Ni metal foil was used. A large phaseshift modification was not required for this edge, but the transferability of the slight adjustment that was applied was tested by fitting to a corresponding c-$NiSi_2$ spectrum. The small phaseshift modification did not alter interatomic distances by more than a hundredth of an Ångstom, but did reduce the error on them as defined by the EXCURV88 'mapping' routine. Such maps for an mid-range composition (x=0.09) are shown in figures 7.7 and 7.8 for correlations between R and $E0$ plus A and N for the first shells of both the Si and Ni-edges. The limit of significance is shown as a bold contour, the errors estimated in this way are quoted in Tables 7.1 and 7.2.

For the Ni-edge, AFAC was determined as 0.75. The magnitude of $E0$ in the fits was found to vary in the range ~7.5 – 10.5eV; while the value of VPI remained within 0.03eV of the standard sample value of -5.5eV.

7.4 Interpretation of EXAFS Results

From figures 7.5 and 7.6 of the Ni K-edge fits, it can be seen that the EXAFS signal is remarkably constant in both phase and amplitude across the composition range studied $0.03 < x < 0.29$. From Table 7.2 it is also evident that there is little significant change in the local environment of the Ni atoms. Each metal atom has approximately 8 nearest neighbours of Si at ~2.35Å and roughly 3 Ni near neighbours at ~2.53Å, resulting in a total coordination of around 11. This figure is surprisingly high considering the assumption of substitutional doping and the presence of Ni-Ni correlations

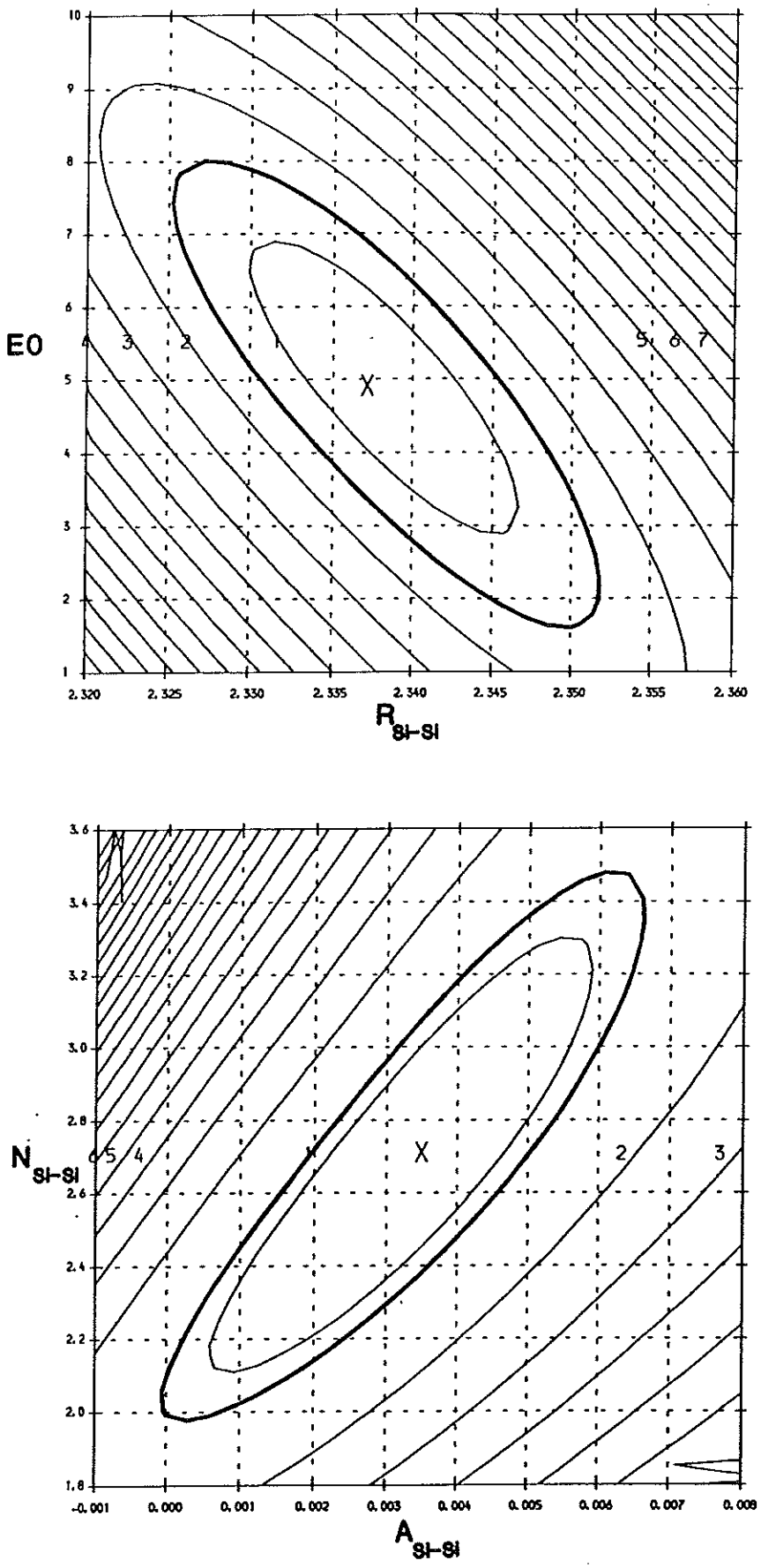

Figure 7.7: Contour map for Si K-edge first shell (x=0.09) showing correlation between R & $E0$ and A & N.

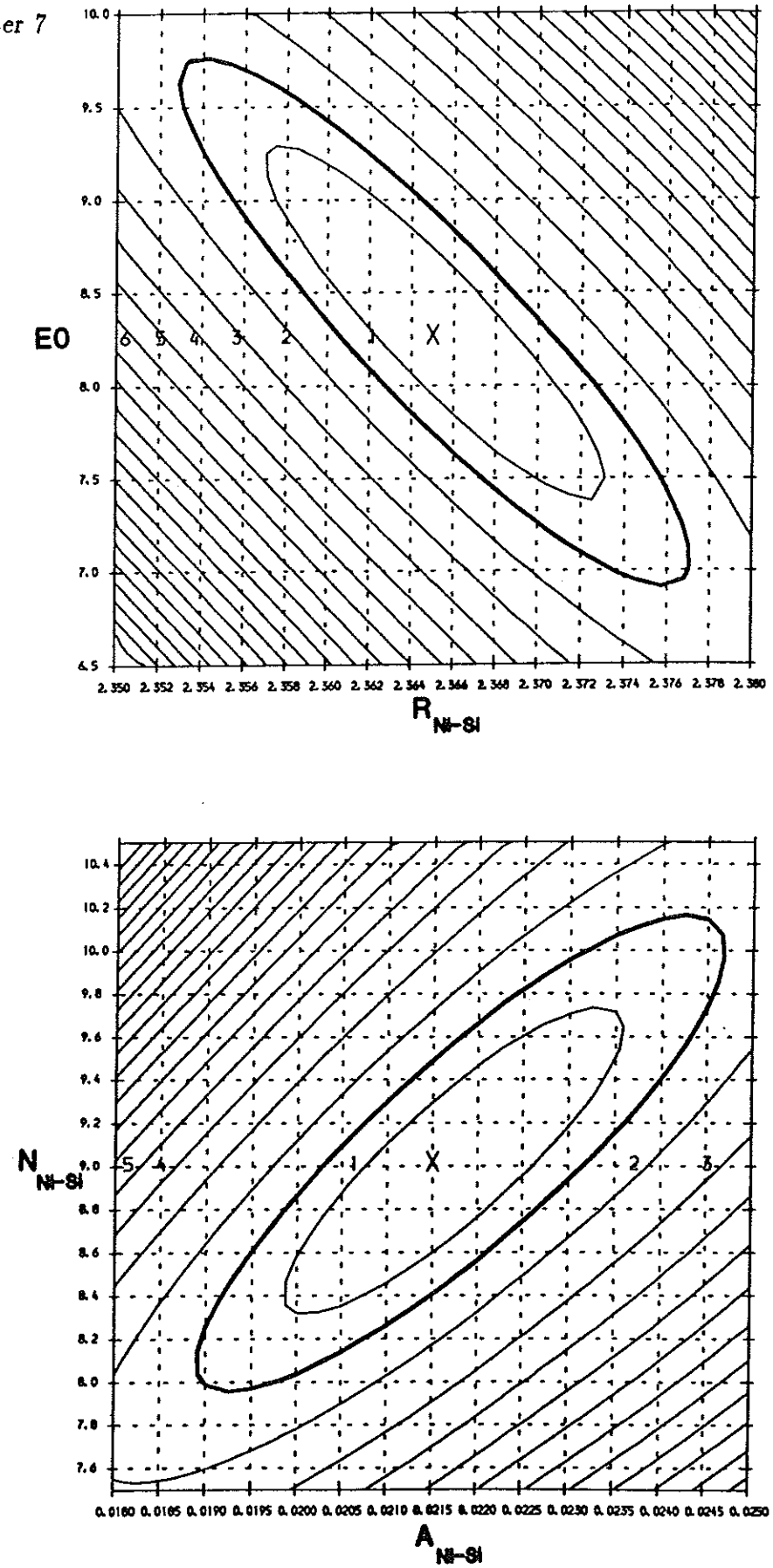

Figure 7.8: Contour map for Ni K-edge first shell (x=0.09) showing correlation between R & $E0$ and A & N.

at low Ni concentrations suggests that some kind of clustering must be occurring around the Ni sites. However, as is clear from the Ni-Si correlations in Table 7.2, this clustering cannot consist simply of metal atoms, but actually comprises of an estimated Si:Ni ratio of at least 2:1. The high Ni-Si coordination strongly suggests that the Ni atoms do not enter the a-Si TRN substitutionally, while the stability of the Ni atom local environment points away from interstitial incorporation. Rather, the results are indicative of a close-packed Ni-Si alloy.

It can be seen from Table 7.1, that at low Ni content the Si K-edge EXAFS is dominated by the a-Si TRN giving rise to the expected interatomic distances and coordination numbers. As the metallic content is increased, there is a trend towards lower Si-Si coordination and larger Si-Si distances. Resolution between Si-Si and Si-Ni distances (which are found to be of similar magnitude) is extremely difficult for the Si-edge data, so that although the nickel must be contributing to the signal at higher values of x, only a near neighbour shell of Si could be reliably fitted. However, not including a Ni shell in the fit introduces a phase problem at higher energies, since Si scatters at low energies only while the Ni scatters at higher energies. The sharp decrease in Si-Si coordination number on addition of Ni can be explained by the fact that the Ni and Si backscattering phases differ by a factor close to π in the energy region of the experiment [70]. Therefore, the Ni backscattering will tend to cancel out that of the Si, causing the EXAFS to determine a Si-Si coordination lower than the true one. Using the Ni-Si coordination given by the Ni-edge data, it is possible to apply a bond consistency method to calculate the expected Si-Ni coordination which is found to show an opposite trend to the Si-Si coordination and rises with increasing metal content. The increasing metal concentration also increases the overall absorption of the soft X-ray beam, decreasing the statistical accuracy of

the Si-edge spectra.

7.5 Complementary Results

7.5.1 Infra-Red Absorption

IR absorption measurements were performed using a double-beam Perkin Elmer 580B spectrophotometer in the wavenumber range 180 – 2500cm^{-1} (0.02 – 0.31eV). This system incorporated an air-filter unit to purge the sample compartment of water vapour and carbon dioxide which absorb in this region. Samples were deposited on 0.5mm thick crystalline silicon substrates, highly polished on both sides to reduce beam scatter at the surface. A similarly polished substrate was placed in the reference beam. Spectra taken at room temperature indicated the presence of Si-H covalent bonds at all compositions. In addition, the spectra show no significant contamination of the samples by oxygen or nitrogen.

As can be seen from figure 7.9, the position of the Si-H bending mode is not altered on addition of the metal, indicating that Ni and H do not bond to the same Si atom. Indeed, the decreasing intensity of the Si-H bending peak with increasing Ni suggests that the hydrogen content is reduced by the addition of the dopant or that overall absorption is increased. Previous work on Ni^+ ion implanted a-Si [90] suggests that direct saturation of dangling bonds with the metal takes place. However, reference to spectra associated with the vibration of Si-As bonds [91] suggests that, under the assumption of comparable bond strengths, a Si-Ni vibrational mode would be expected in the range 400 – 600cm^{-1}. This feature is not present in any of the spectra, indicating the lack of covalent bonds between Ni and Si.

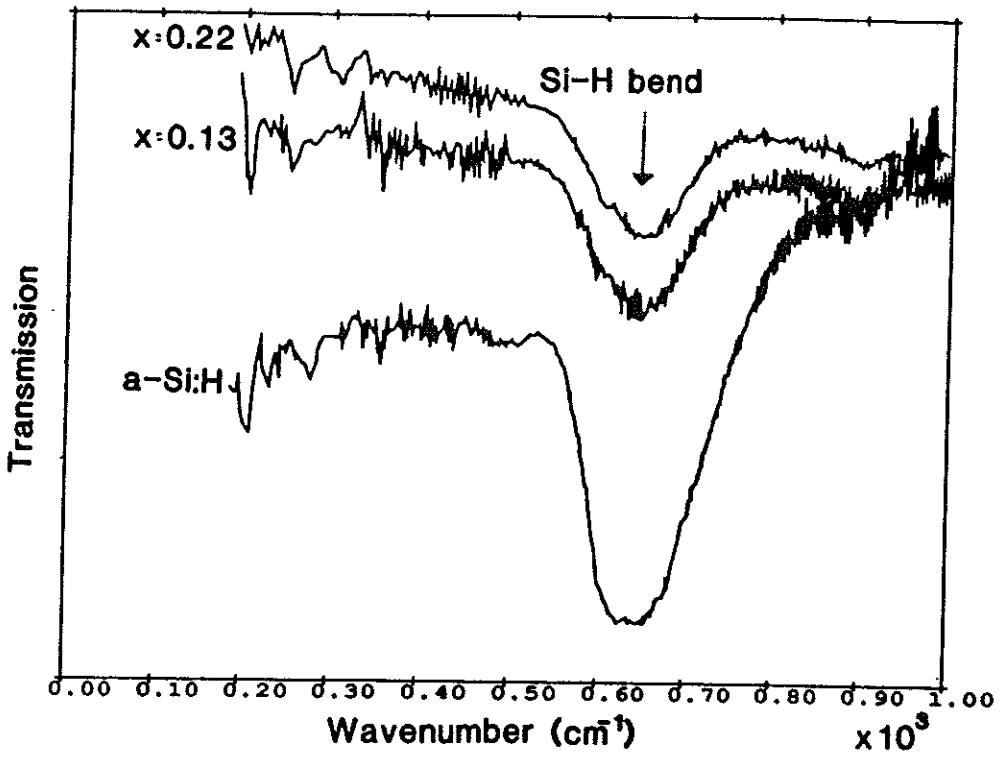

Figure 7.9: IR absorption spectra of some a-$Si_{1-x}Ni_x$:H samples illustrating the Si-H bending mode (spectra vertically offset for clarity).

7.5.2 Raman Scattering

Raman spectroscopy was performed using plane polarised light from the 5145Å line of a 1W Spectra-Physics argon ion laser over the range 200 - 700cm^{-1}. The scattered light entered a SPEX 1402 double-grating monochromator and its intensity was measured using a cooled photo-multiplier and an Ortec-Brookdeal photon counter. Measurements were taken in reflection geometry using glass substrates. Raman scattering provides an extremely sensitive test for the presence of crystalline silicon: microcrystallites of c-Si down to around 20Å diameter resulting in the presence of a very distinct Raman peak at 522cm^{-1} [92], whereas the spectrum of a-Si has a much broader peak at around 480cm^{-1} [93]. The spectra of some of the samples within the composition range $0.03 < x < 0.25$ and an example of a c-Si spectrum are shown in figure 7.10. All of the sample spectra show the broad peak centred around 480cm^{-1} and there is no evidence in any of these spectra for the c-Si peak, indicating that the a-Si network persists over the entire composition range. The sharp peaks observed in some of the spectra are the plasma lines of the Ar^+ laser. The visibility of these lines depends on the sample surface. The intensity of the a-Si peaks decreases with increasing metal content indicating that the proportion of the sample that consists of a-Si decreases as more Ni is added. The corresponding broadening of the peaks is consistent with an increasing rms bond-angle deviation [94], suggesting that internal stress in the films is gradually increased as more impurity is introduced. However, the spectra obtained were not of sufficient statistical quality for a quantitative analysis.

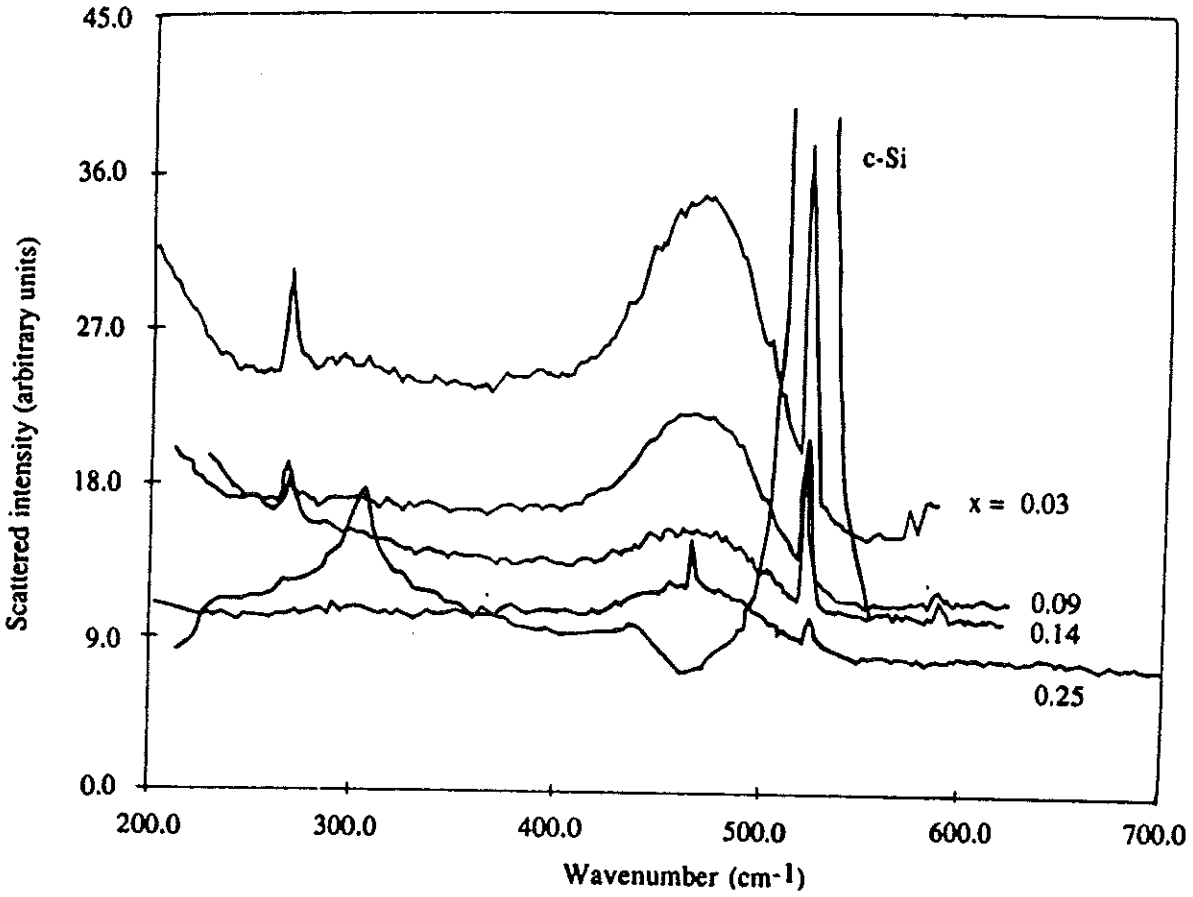

Figure 7.10: Raman spectra of a-$Si_{1-x}Ni_x$:H compared to that of c-Si.

7.5.3 Neutron Scattering

A neutron scattering experiment was performed on a single powder sample of a-$Si_{1-x}Ni_x$:D of composition $x \sim 0.1$ using the liquids and amorphous materials diffractometer (LAD) on the ISIS spallation neutron source at the SERC Rutherford Appleton Laboratory. Deuterium was substituted for the more usual hydrogen in order to minimise the complications in the reduction of experimental data due to the high incoherent neutron scattering cross-section of hydrogen. Despite rather poor statistics due to limited beamtime and the small volume of the sample (limited by the sputtering technique), figure 7.11 shows no observable volume fraction of crystalline material over the whole sample and thus provides further strong evidence of the amorphous nature of the sample.

7.6 Discussion

EXAFS results from the Ni K-edge clearly indicate some form of clustering of both Si and Ni atoms around the Ni sites. The Ni-Ni and Ni-Si distances determined here correspond to some of the interatomic distances found in several phases of the crystalline Ni_aSi_b system [95, 96, 97, 98, 99]. However, neither the neutron diffraction experiment nor any other structural techniques employed (*e.g.* TEM, EXAFS, Raman) showed any evidence of crystallinity, leading to the conclusion that the clusters take the structure of some amorphous form of nickel silicide. This is consistent with IR transmission results which showed no evidence of Si-Ni covalent bonding, and given that the nickel silicide system has 8 stable phases [100] it is highly probable that a disordered mixture of these can be deposited by sputtering.

Raman spectroscopy indicates the presence of an a-Si matrix at all compositions

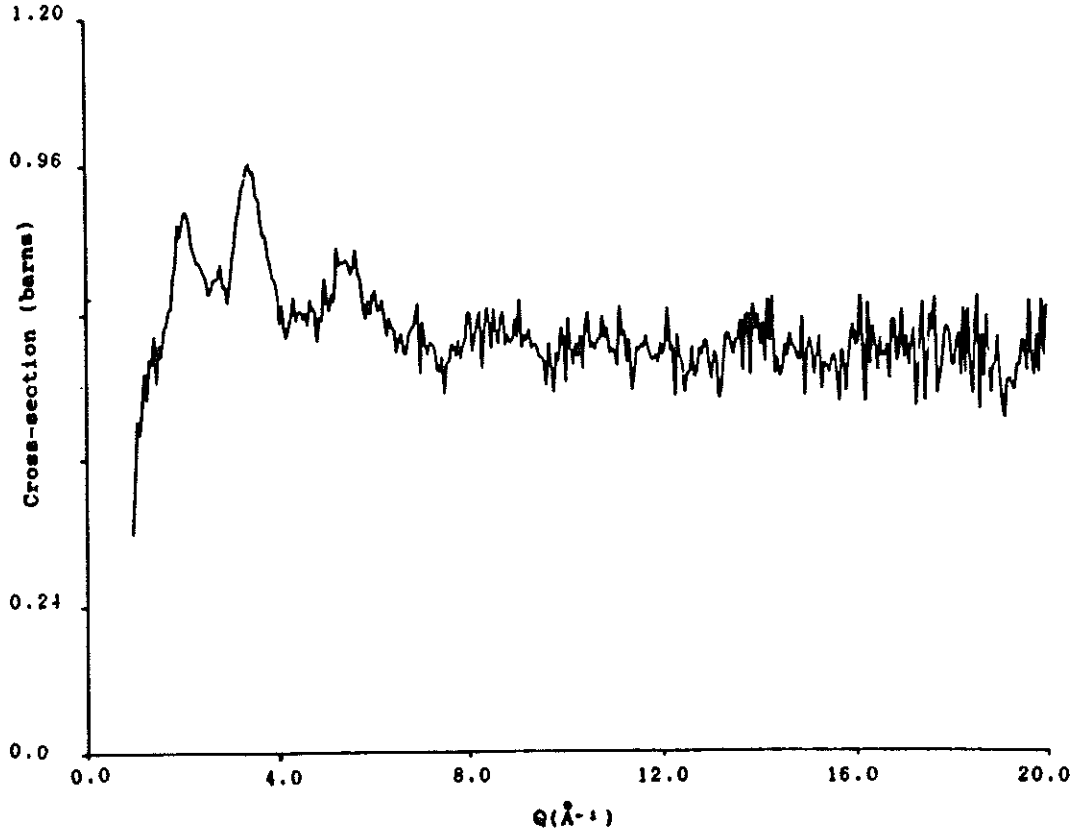

Figure 7.11: Total neutron scattering cross-section for a-$Si_{0.9}Ni_{0.1}$:D.

with no evidence of any c-Si. This fact, taken with the previous conclusions, implies that the system contains two distinct amorphous regions, both containing Si. This complicates the interpretation of the Si K-edge EXAFS since the technique only returns coordination numbers and interatomic distances for the environment around a specific atom, averaged over all of the sites occupied by that atom. In the light of this heterogeneous structure, the Si-edge results can now be interpreted as containing increasing contributions from the disordered Ni-Si clusters with increasing metal content, although an a-Si TRN persists at all compositions. Using this explanation, the trend of increasing Si-Si interatomic distance for higher metal concentrations suggests that the average Si-Si distance in the clusters is greater than in a-Si. Although Ni-edge data indicates that a Ni-Si amorphous alloy of roughly constant composition is present at all values of x and Si-edge results show that its contribution to the spectra increases as more Ni is added, it is not clear whether it is the size or number of clusters (or indeed both) that is increasing.

Comparing these results qualitatively with those for a-Ge:Ni [81, 82], it can be seen that the general trends are similar. Without direct evidence for or against the existence of the a-Ge TRN above 10at.% Ni, it is likely that this system has a heterogeneous structure similar to a-Si:Ni. However, the increasing Ge-Ni coordination reported in the EXAFS paper suggests that any disordered Ge-Ni alloy may not be of roughly constant composition as in the Ni-Si case; this possibly being due to the lower rate of diffusion of Ni in Ge compared to Si.

Evidence for a 2-phase system is further supported by the two recrystallization temperatures (~450° and 650°) measured by differential scanning calorimetry (DSC) on a single composition, $x \sim 0.1$ (see figure 7.12 [101]). From the Ni-edge EXAFS

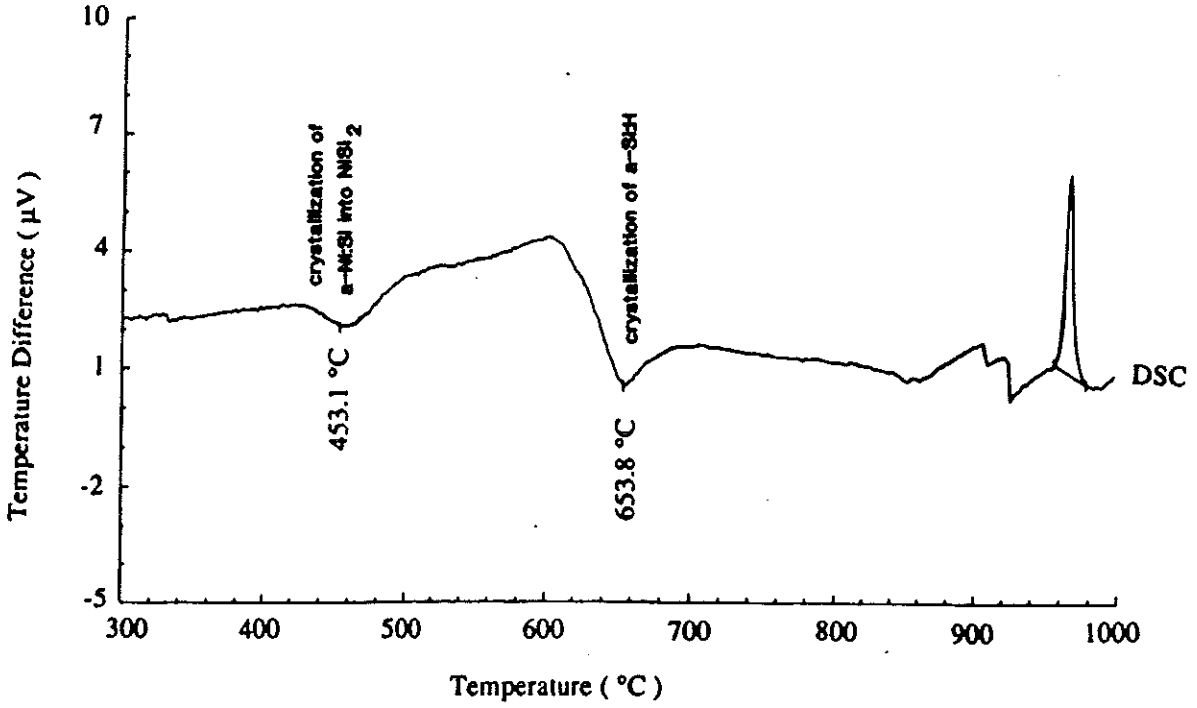

Figure 7.12: Differential scanning calorimetry scan of a-$Si_{0.9}Ni_{0.1}$:H.

results it was observed that the ratio of Si:Ni in the amorphous clusters is approximately 2:1; indeed, X-ray diffraction on a laboratory source is consistent with the lower temperature DSC transition being associated with the formation of crystalline $NiSi_2$ having a fluorite structure. Furthermore, the recrystallization temperature of 650° is known to correspond to the crystallization of a-Si:H [102].

The formation of amorphous phases of Ni:Si has also been observed on deposition of thin layers of Ni onto crystalline Si [103, 104], where the interface with Si is actually replaced by a nickel silicide layer. The annealing of thick (>200$\AA$) layers of Ni on Si(111) has been found to result in the initial growth of Ni_2Si, followed by NiSi above

300°, and finally the formation of $NiSi_2$ at around 750° and above [104, 105, 106]. However, reaction of thin (<30Å) layers of Ni showed the temperature of formation of the $NiSi_2$ phase to be approximately 450° [105] and this appears to be the behaviour observed in this completely amorphous Si:Ni system. Room temperature deposition of Ni on Si limited to a few monolayers has also been found to result in a disordered layer exhibiting SRO similar to that associated with the $NiSi_2$ lattice [105, 107]. In all cases the Ni is determined as being the diffusive species and it has been postulated [108] that the high mobility of the interface can be achieved by transforming Si atoms at the interface from covalent to metallic bonding. Similar results to those referenced above are obtained when a-Si substrates are used; however, in this case annealing of 200Å thick layers of Ni resulted in the presence of metallic Ni in addition to the crystalline Ni_2Si and NiSi [109].

The crystalline phases of the Ni-Si system are described as intermetallics and are known to have properties close to those of metals *e.g.* metallic lustre, conductivity and hardness [90]. The conductivity of c-$NiSi_2$ thin-films is reported to be of the order of $10^4\Omega^{-1}cm^{-1}$ [110]. Although this is much lower than reported for bulk $NiSi_2$, it is still much higher than the $10^2\Omega^{-1}cm^{-1}$ conductivity determined for an x=0.53 sample of a-$Si_{1-x}Ni_x$:H [89]. Raman scattering results from a-$NiSi_2$ [111] report high reflectance indicative of metallic or semimetallic character. Optical reflectivity measurements on a-$Si_{1-x}Ni_x$:H in the UV and visible ranges [89] show a large increase in absorption with the addition of even small amounts of Ni, and dc conductivity results on this system show a dramatic increase in conductivity in the same composition range.

Thus the a-Si:Ni:H system is perceived as consisting of a semiconducting a-Si medium containing amorphous Ni:Si clusters of a somewhat higher conductivity. In this structural arrangement, some of the Si in the sample is contributing to the regions

of greater conductivity. Therefore, the conductivity of a larger volume fraction of the sample will be enhanced than would be estimated from a naive use of Ni content, and hence it is possible that an MIT may occur at a lower Ni concentration than would otherwise be expected. If the composition of the clusters is taken as approximately that of $NiSi_2$, then a sample containing 5at.% Ni would have roughly 15% of all atoms residing within these clusters and therefore contributing to an increased conductivity. Hence, aggregation of the dopant into cluster regions in the sample does not preclude the occurrence of a transition at the expected concentration of metal-like material and it may be contended that an Anderson transition may occur in this a-Si:H/a-Si:Ni system at a composition containing as little as 5at.% Ni. However, the conclusions of other optical and electronic work [85, 89] that there is no MIT for x <0.25 suggests that this is not the case and that the Ni-Si clusters are only weakly conducting. It should also be noted that the inhomogeneity of the samples may, in fact, result in a difference between the metal concentrations at which the MIT is observed by conductivity and optical measurements. This is because the dc current will preferentially seek out any paths of higher conductivity between the electrodes.

7.7 Conclusion

From the structural study of this a-$Si_{1-x}Ni_x$:H system it is concluded that the samples prepared contain two amorphous phases: one being a modified semiconducting a-Si:H network, while the other contains both silicon and nickel atoms and is thought to be of higher conductivity. Evidence for such a two-phase system has also been reported for a-$Ge_{1-x}Mo_x$ alloys [112].

These results indicate that the assumption that the metal-insulator transitions observed in a-Si:M systems (where M = transition metal) are of Anderson type is not

as well founded as previously thought. Indeed, the evidence for an inhomogeneous structure suggests that the application of classical percolation theory, where conduction occurs via the percolation of electrons along interconnecting regions of enhanced conductivity, may be more appropriate. It is apparent, therefore, that a knowledge of the structure of a semiconducting:metal system is a necessary prerequisite for a successful description of the conduction mechanism to be made. Comparison with the electronic [113] and structural [81, 82] properties observed in a-Ge:Ni alloys indicate that it would be interesting to extend these studies to higher Ni concentrations.

Chapter 8

Amorphous Silicon:Tin:Hydrogen Thin-Films and the effects of Deuteration

8.1 Introduction

Hydrogenated amorphous silicon-based group IV alloys began to receive a great deal of interest at around the beginning of this decade due to their potential application in inexpensive, multijunction photovoltaic devices. Whilst the other members of this group of elements show low solid solubility in c-Si, it was found possible to incorporate large concentrations of them in a-Si(:H). The addition of such elements into silicon allows the optical band-gaps of these materials to be altered systematically with dopant concentration — carbon raises the band-gap while germanium and tin lower it.

Optimization of device structures requires materials with band-gaps around 1.4eV.

While this band-gap reduction could be achieved with approximately 50at.% Ge, the photoelectronic properties of these highly-doped alloys was found to decrease significantly relative to a-Si:H [114, 115]. Substantially smaller concentrations (<10%) of the near-zero band-gap element, tin, were found to reduce the a-Si:H gap to the 1.4eV range [116], and this prompted much work on the photoelectronic properties of this system prepared by a variety of techniques [117, 118, 119, 120, 121, 122]. Despite these extensive optical and electronic studies, less attention has been focussed on the structural variation of a-Si:Sn(:H) with increasing Sn content; although some structural conclusions have been drawn from infra-red spectroscopy [119, 121], and limited electron [123] and X-ray [124, 125] diffraction; while the Sn sites have been probed by ^{119}Sn Mössbauer spectroscopy [119, 123].

Unfortunately, the photoelectronic properties of a-Si:Sn:H have been found to degrade with increasing dopant concentration [117, 119, 121], and furthermore thin-films of this material are thermally unstable, crystallizing at temperatures as low as 300°C depending on sample preparation conditions [126]. Hence, the material never realized its hoped-for potential in energy conversion devices.

However, the surge of interest in the a-Si:Sn:H system did produce some interesting, if less marketable, results. While the optical band-gap was found to decrease monotonically with increasing Sn concentration [121, 122], the dark dc conductivity did not increase as much as would be expected on the basis of a conduction mechanism with an activation energy close to one half of the optical gap [119, 121, 127]. Indeed, the dark conductivity has been found by some workers to show a minimum at an optical gap corresponding to a value of ~1.7eV [117, 120] indicating a change from n- to p-type conduction at the corresponding Sn concentration (<5at.%). The suppressed increase of dc dark conductivity, along with its temperature dependence,

lead all these authors to the conclusion that the conduction mechanism changes from extended state to localized state hopping. While some of the films studied were prepared by rf glow-discharge of $SnCl_4$ or $Sn(CH_3)_4$ and may therefore have contained substantial quantities of Cl or C, others were deposited by sputtering techniques, indicating that the transition was inherently due to dopant defect states. Similar changes in the conductivity mechanism have been noted for analogous systems such as a-Si:C:H [128] and a-Si:Ge:H [120].

For sputtered films, the onset of this transition is suggested to occur anywhere between 1at.% [121] and 20at.% Sn [119, 129] depending on preparation conditions (*e.g.* sputtering pressure, hydrogen incorporation, Ar:H ratio *etc.*) [119]. It is this change in conduction mechanism that is responsible for the degradation of the photoelectronic properties of the films, and is attributed to a change in the way the Sn atoms are incorporated into the a-Si network. It has been suggested that the transition is a result of the inclusion of Sn atoms into non-tetrahedral bonding states *e.g.* divalent Sn atoms [121] and the production of Sn dangling bonds. Sn is known to show a preference for bonding in a divalent rather than tetravalent state as is evident from the properties of pure Sn — the semiconducting, low temperature phase (α-Sn) having a diamond-like structure whereas the high temperature, metallic phase (β-Sn) shows sixfold coordination.

^{119}Sn Mössbauer spectroscopy was used by Williamson and Deb [124] to probe the Sn configurations, and revealed Sn atoms to be incorporated in at least four distinct sites — substitutional (covalent) Sn, Sn^{4+}, Sn^{2+} and crystalline β-Sn precipitates. However, lowering the sputtering pressure ($\sim$5.3mbar as opposed to $\sim$27mbar) and using rf rather than dc sputtering was found to eliminate incorporation in the latter three sites. More recent Mössbauer studies on co-evaporated a-Si:Sn performed by

Vergnat et al. [123] detected only the substitutional site, with every Sn atom tending to be selectively surrounded by Si atoms in almost perfect tetrahedral units. The substitution of Sn for Si in a TRN was also indicated by the latter author's electron diffraction studies. X-ray diffraction investigations have clearly shown the precipitation of β-Sn clusters in some films. However, both sets of authors conclude that these can be eliminated by variations in preparation conditions such as those mentioned above. A similar effect has been found for reductions in substrate temperature, and it has been suggested that lowering the substrate temperature to <220°C reduces the mobility of Sn atom on the surface of the growing film, giving them sufficient time to bond tetrahedrally in the alloys. If this is the case it is possible that, under the correct preparation conditions, Sn will mainly enter the a-Si:H matrix substitutionally [125].

Lin et al. [130] compared dc dark conductivity experimental results with calculations of the electronic properties of fourfold-, threefold- and twofold-coordinated Sn atoms in a-Si:Sn:H alloy films. They found qualitative agreement with the idea of tetrahedral Sn incorporation at low metal concentrations, changing to a significant fraction of divalent sites and an overall increase in the total number of dangling bonds with increasing Sn. Infra-red absorption results, which should indicate the presence of any Sn-H covalent bonds, has reported variable findings. Girginoudi et al. [127] and von Roedern et al. [120] both confirm the presence of a Sn-H vibration, whilst Williamson et al. [119] and Parsons et al. [121] report no evidence for Sn-H bonds. However, this latter result may be due to the preferential attachment of H to Si [131]. Since the amount of H in the system is clearly dependent on the preparation conditions, this again emphasizes that only samples prepared under identical conditions can be compared directly.

A further interesting feature of the a-$Si_{1-x}Sn_x$:H alloy is that, in contrast to

transition metal systems such as a-$Si_{1-x}Ni_x$:H (Chapter 7), this system is not expected to show a sharp, Anderson-type MIT. The monotonically decreasing optical band-gap (E_g) has been extrapolated to E_g=0 for values of x between 0.31 and 0.46 [119, 121, 122] using various methods; the higher values being those corrected to account for decreasing hydrogen content with increasing Sn. It is interesting to note that for a tetrahedrally coordinated structure the site percolation threshold occurs at x=0.43 [18].

In order to obtain detailed information about the local environment of both the Sn and Si sites, the chemically specific EXAFS technique has been used to investigate the microstructure of device quality, plasma deposited a-$Si_{1-x}Sn_x$:H thin-films.

During the course of the Si-edge investigations, a comparison was made of the Si environments of a-Si:H and a-Si:D. Hydrogenation during deposition of amorphous, tetrahedrally-coordinated semiconducting thin-films has become an accepted means for reducing the density of defect-related states in the gap. However using neutron diffraction experiments, the partial radial distribution functions for a-Si:H may only be derived by using the technique of isotopic substitution [132] of deuterium for hydrogen. Of fundamental importance in this approach is the assumption that deuteration does not alter the sample's structure. This assumption, although reasonable, is impossible to test with neutrons and thus previous comparisons between a-Si:H and a-Si:D have been confined to IR and Raman spectroscopy [133]. The insensitivity of X-rays to hydrogen makes EXAFS a suitable technique for such a direct structural comparison. Initial investigations into the local environment around argon that may have been incorporated during sample deposition have also been made.

8.2 Sample Preparation and Characterization

Thin-films of a-$Si_{1-x}Sn_x$:H and a-Si:D were prepared by rf reactive sputtering (Chapter 4). The deposition parameters were very similar to those given in Table 4.1. In the case of a-Si:Sn:H, the composition of the films was varied by altering the number of 99.99% pure Sn pieces placed on the target. Neither SAED-TEM nor SEM measurements indicated clusters of β-Sn or any other form of crystallinity in any of the films. Talysurf measurements again found all films to be in the 1–2μm thickness range after 8 hours of deposition onto unheated substrates.

Initial sample compositions, as determined by EPMA immediately after deposition, indicated that Sn contents varied in the range $0< x <0.36$ for the metal containing films. This composition range would have included one, if not both, of the possible important transitions (extended state $\rightarrow$ localized state conduction and $E_g \rightarrow 0$); however, lack of the application of the ZAF correction (section 4.2.1) to these results rendered them unreliable, and a later application of the more direct $^4He^+$ Rutherford backscattering technique found the actual range to be $0< x <0.18$. The SEM results also indicated the presence of Ar in all of the films. This was not observed in the RBS plots and hence desorption of Ar was assumed to occur with time.

Initial dc dark conductivity measurements on the films prepared for this study were performed in a parallel study at the University of Leicester [88]. These appeared to show $T^{-1/4}$ dependence below room temperature, indicative of variable range hopping, and T^{-1} dependent localized state conduction for the majority of samples above room temperature. This is in qualitative agreement with the results of others [134, 135]. The dependence of room temperature dark conductivity on Sn concentration showed good qualitative agreement with that of Girginoudi et al. [127], as did the variation

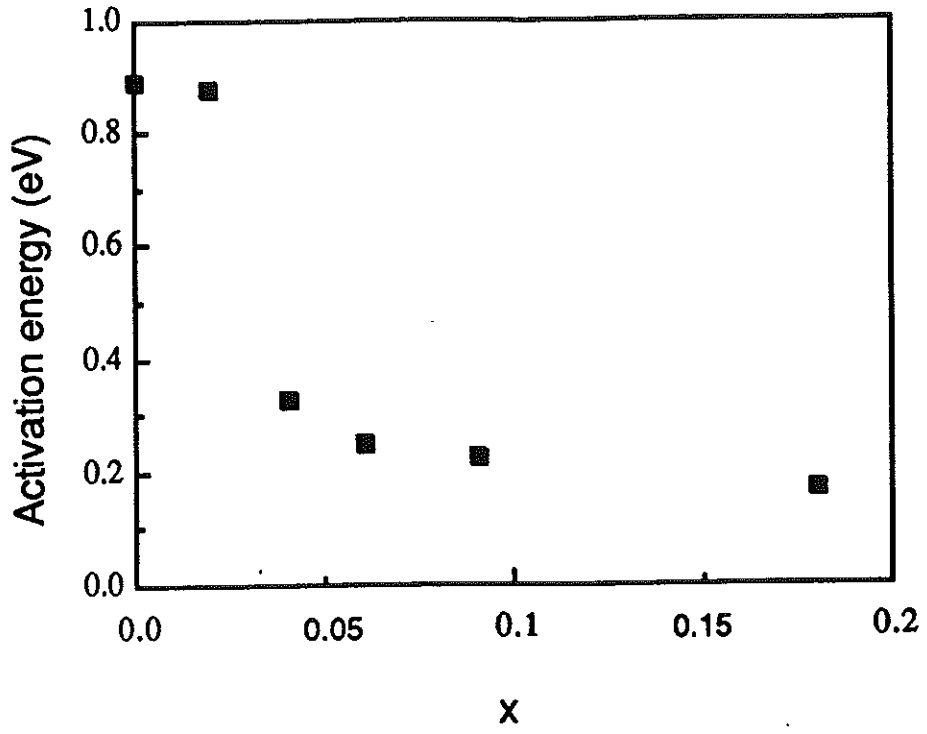

Figure 8.1: Variation of activation energy with Sn content for a-Si:Sn:H

of activation energy with x (figure 8.1 [88]). From this figure, the 0.9eV activation energy (typical for undoped a-Si:H alloys) indicates that for values of x up to $\sim$0.03, the conduction mechanism is of free carrier type. A transition from extended to localized state conduction, and a correspondingly large decrease in activation energy to around 0.2eV (typical for heavily doped a-Si:H alloys [4]) appears to occur above this metal concentration. In addition, relatively low crystallization temperatures were discovered for all films; between $\sim$140 and 170°C, decreasing with increasing Sn content. Further work and additional optical studies are currently in progress on 'in-house' samples at the University of Leicester.

Room temperature infra-red absorption measurements for the a-Si:Sn:H system

were performed on a Mattson Instruments Alpha Centauir FTIR spectrophotometer in the wavelength range 480 – 2500cm^{-1}. Spectra for the a-Si:H/D comparison were taken using the spectrophotometer described in Chapter 7. All samples were deposited on 0.5mm thick c-Si substrates, highly polished on both sides, and all spectra taken immediately after deposition confirmed that none of the films were contaminated with either oxygen or nitrogen.

IR spectra for a-Si:Sn:H are shown in figure 8.2 for the wavenumber range 1500 – 2500cm^{-1}. The full spectral range is not shown since, on the single beam instrument used, the presence of the high intensity c-Si absorption peak at 613cm^{-1}, due to the substrate, reduces the relative intensity of the weaker Si-H stretch shown ~2060 – 2080cm^{-1}. There appears to be no systematic shift in wavenumber nor variation in intensity with increasing Sn. This latter fact suggests that the number of Si-H bonds is not altered appreciably in this concentration range. The most important aspect of these spectra is the lack of any Sn-H features, expected ~1700 – 2000cm^{-1} [119, 120, 121, 127]. This is in disagreement with the results of von Roedern et al. [120] and Girginoudi [127] who reported a Sn-H vibration (though only for samples above x=0.1 in the latter case). The former author used a glow-discharge technique which may produce films radically different in structure to those used in this study; whilst the samples studied by Girginoudi et al. were prepared by rf sputtering, but in an Ar-24%H_2 atmosphere. No evidence of Sn-H bonding was found by Williamson et al. [119] or Parsons et al. [121] who both prepared samples by rf sputtering, the former using an Ar-10%H_2 atmosphere. However, these latter authors suggest that this may be due to a strong preference for the hydrogen to bond to the Si rather than the Sn in the absence of sufficient H_2 to saturate all the dangling bonds in the system. A preference ratio of up to 12:1 for Si-H bonds compared to Sn-H bonds has

been reported by von Roedern et al. [120].

ESR results [126] showed signals due to both Si and Sn dangling bonds for some films, but only those due to Si in others, depending on preparation conditions such as substrate temperature and hydrogen content.

Figure 8.3 shows the a-Si:H and a-Si:D spectra, vertically offset for clarity. In the a-Si:H spectrum, the Si–H stretching vibrational mode (A) at around 2000cm^{-1} and the Si–H out of phase bending mode (B) at 650–600cm^{-1} are clearly visible, but the weak in-phase bending mode that should occur around 485cm^{-1} is not observed. The range 1700–800cm^{-1} shows interference fringes due to the thin-film nature of the samples. There is little evidence of doubly or triply bonded hydrogen (SiH_2, SiH_3 groups) which would produce stretching frequencies around 100cm^{-1} above those observed and introduce scissor-bending modes in the 900–840cm^{-1} region, though these have been observed by others [136].

For the a-Si:D spectrum, the stretching mode (A) is shifted to a lower frequency of around 1460cm^{-1} *i.e.* reduced by a factor roughly equivalent to the square root of the mass ratio of D:H. The bending vibration is shifted by a smaller factor and displays two modes (B and C); the higher frequency mode at around 500cm^{-1} (C) being the in-phase vibration (where the Si-atom displacement is greater than that of the D-atom) and the out of phase mode above 400cm^{-1} (B), which corresponds to the only observed Si–H bending mode, occurring at the lower frequency— the reverse of the Si:H case. Comparison of the spectra indicates that there is no hydrogen contamination in a-Si:D, and vice versa. Unfortunately, it is not possible to perform a reliable compositional analysis using this technique but a qualitative comparison of absorption intensities suggests that the amounts of hydrogen and deuterium incorporated are roughly similar. This would be expected for samples prepared at the same

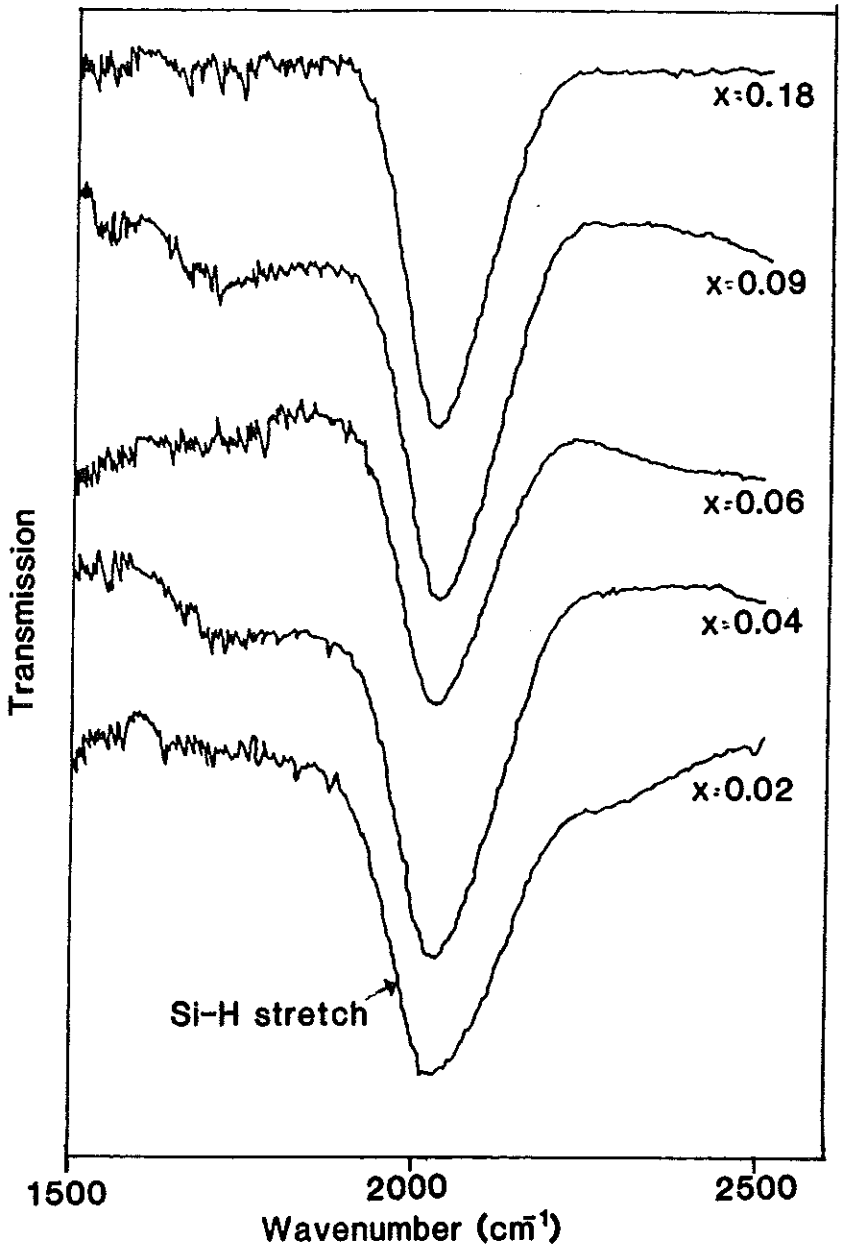

Figure 8.2: IR absorption spectra of some a-$Si_{1-x}Sn_x$:H samples illustrating the Si-H stretching mode (spectra vertically offset for clarity).

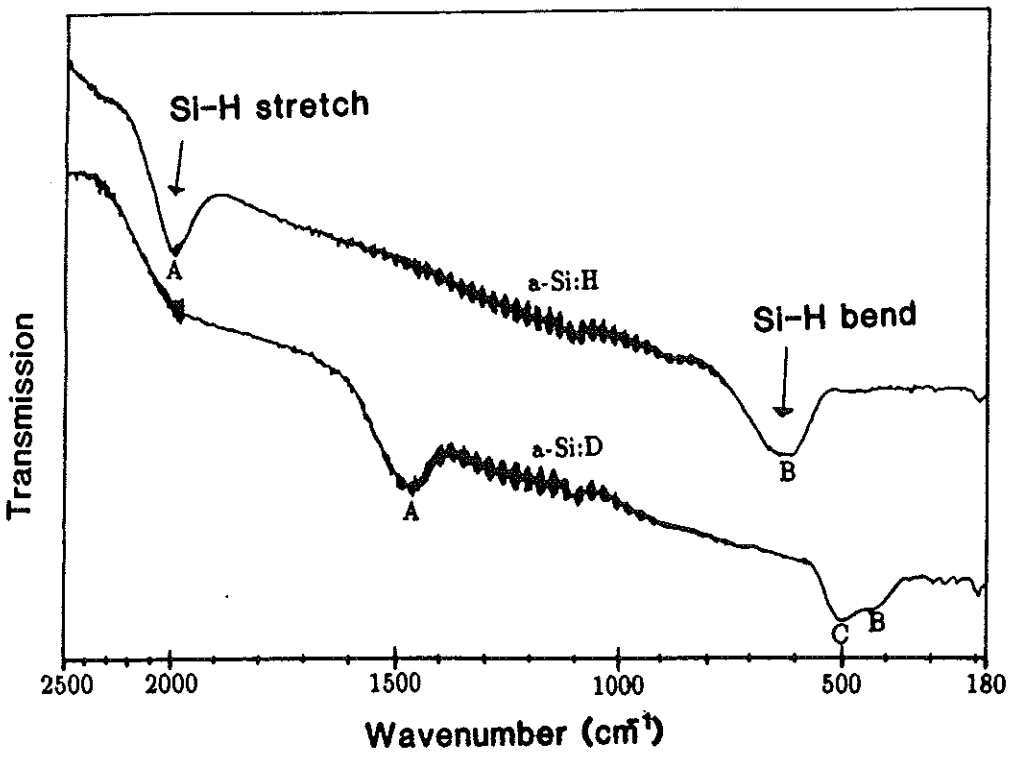

Figure 8.3: IR absorption spectra of a-Si:H and a-Si:D (note: x-axis in decreasing wavenumber).

substrate temperature [129]. Other work, based on hydrogen evolution studies [137] suggests a bonded hydrogen concentration of around 15at%.

8.3 EXAFS Results and Interpretation

Extended X-ray absorption fine structure results for both the Si and Sn K-edges of a-$Si_{1-x}Sn_x$:H were taken for samples in the composition range $0< x <0.18$ using beamlines 3.4 and 9.2 of the SRS. The former beamline was also used for the study of the local structures of a-Si:H and a-Si:D, and for the investigation of the EXAFS

associated with the argon K-edge of any Ar that may have been incorporated during the sputtering process.

All Si and Ar K-edge data were collected by the electron drain current method using 1–2μm thick samples deposited on stainless steel substrates. The k^3-weighted Si K-edge EXAFS functions and radial distribution functions (RDFs) are shown in figures 8.4 and 8.5 respectively. Over the composition range studied ($0< x <0.18$) the phase and amplitude of the EXAFS signal remains approximately constant and suggests that the structure is dominated by the a-Si TRN. All the RDFs show a single peak at 2.35$\AA$, characteristic of a-Si. There is little evidence apparent in the RDFs for the existence of Si-Sn correlations except for a small shoulder that is present on the high r side of the main RDF peak for the x=0.18 sample.

Results from the fitting of the theoretical Si K-edge EXAFS function to the experimental data are shown in Table 8.1 and support the qualitative assertions above. Errors indicated in the table are those taken from the limit of significance of correlation maps such as those shown in figure 8.6. Phaseshift corrections, as described in Chapter 7, were applied and again the the amplitude factor (AFAC) was fixed at 0.7 for this edge. The energy offset ($E0$) was found to vary between 1.12 and 4.34eV, while the electron mean free path factor (VPI) ranged from -2.82 to -4.29eV.

The Si-edge data for the samples with x <0.07 is best interpreted in terms of a single shell of approximately 4 Si atoms at an interatomic distance of 2.35$\AA$. The Si-Si coordination number of the x=0.09 sample appears to have decreased, although there is little evidence of Si-Sn correlations. However, the x=0.18 sample begins to show the presence of Sn atoms at a distance of 2.61$\AA$ together with Si atoms at 2.35$\AA$, retaining a total coordination of 4.

Sn K-edge experiments were performed in transmission using stacked samples

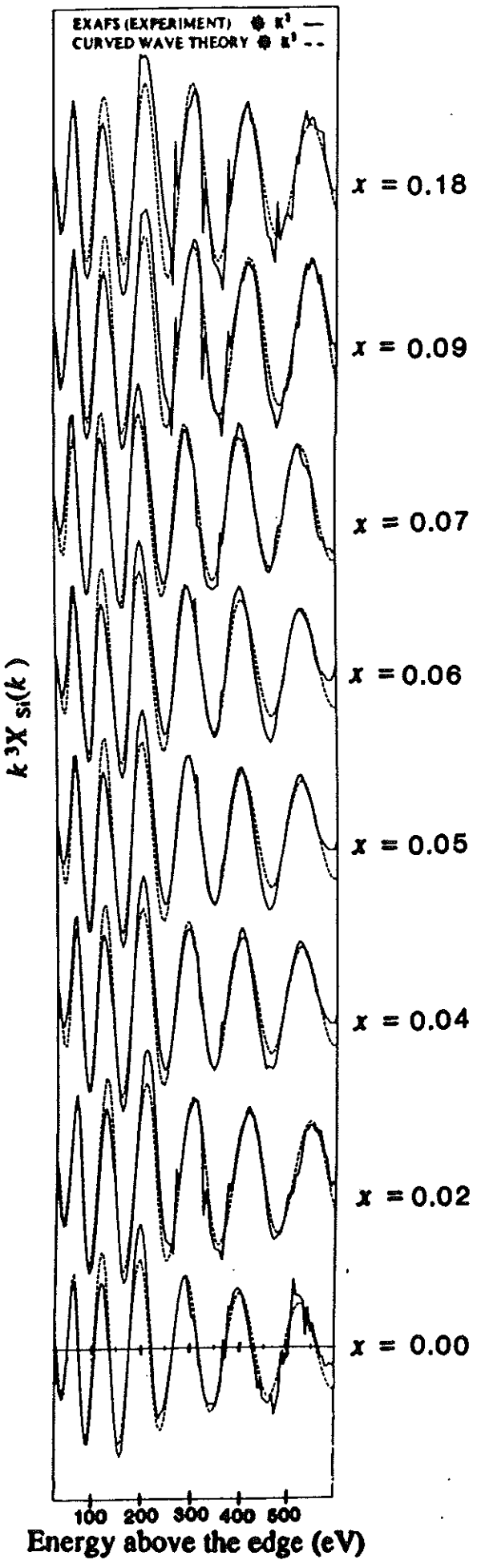

Figure 8.4: Silicon K-edge EXAFS spectra for a-$Si_{1-x}Sn_x$:H.

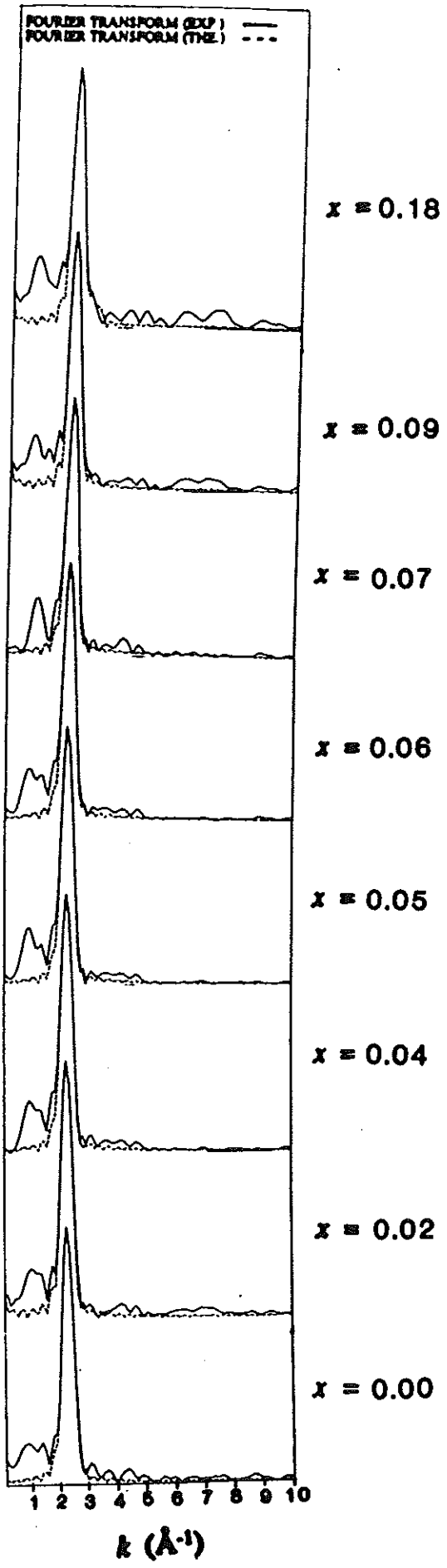

Figure 8.5: Silicon K-edge Fourier transforms for a-$Si_{1-x}Sn_x$:H.

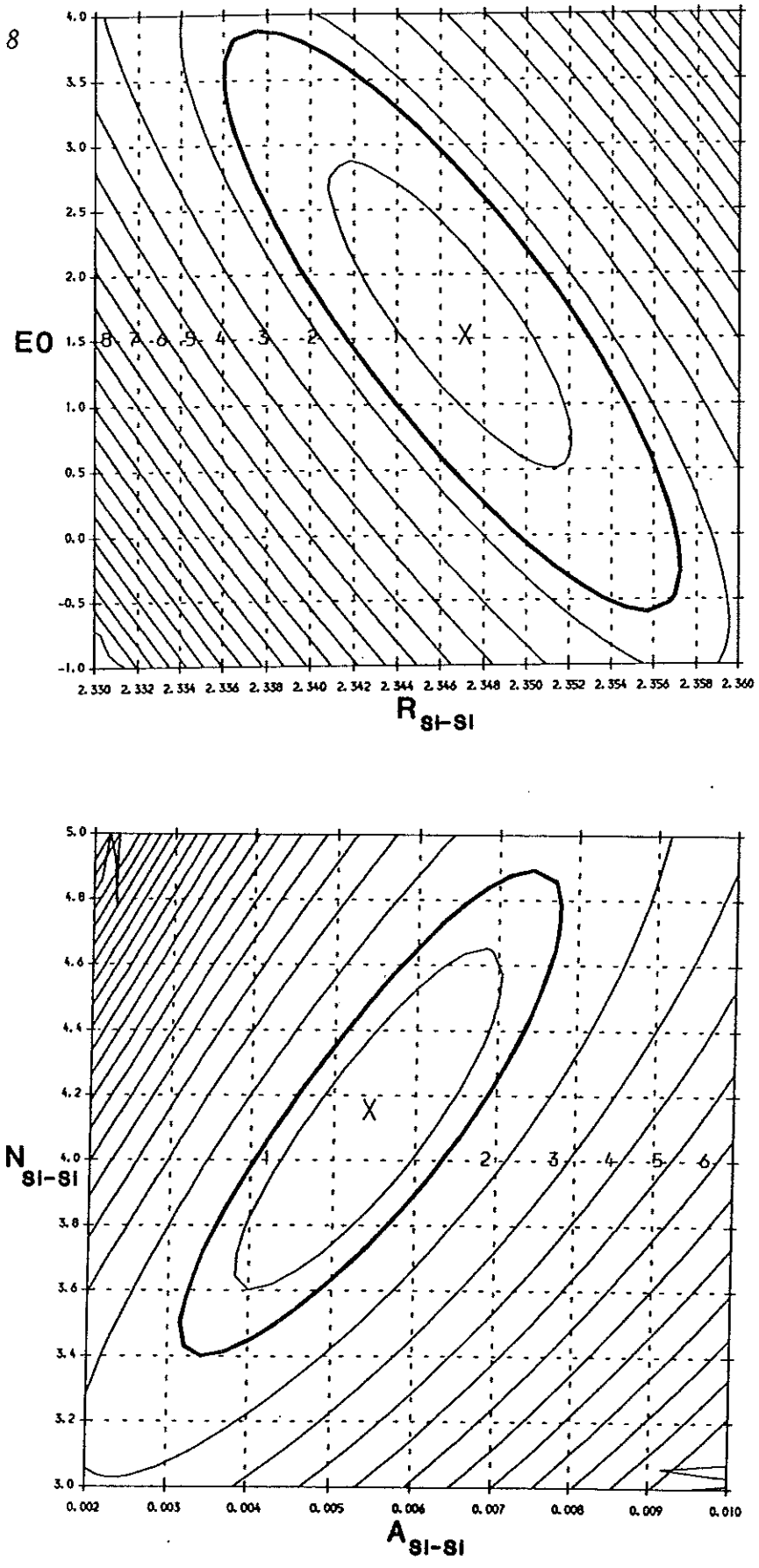

Figure 8.6: Contour map for Si K-edge first shell (x=0.06) showing correlation between R & $E0$ and A & N.

Table 8.1 Silicon K-edge EXAFS results for a-$Si_{1-x}Sn_x$:H

AFAC=0.7

x	$E0$ (eV)	VPI (eV)	N_{Si-Si} (± 0.8)	R_{Si-Si} ($\pm 0.01\AA$)	A_{Si-Si} ($\pm 0.002\AA^2$)	N_{Si-Sn} (± 0.5)	R_{Si-Sn} ($\pm 0.02\AA$)	A_{Si-Sn} ($\pm 0.005\AA^2$)
0.00	2.82	-3.31	4.1	2.34	0.006			
0.02	4.34	-2.82	4.0	2.34	0.006			
0.04	1.73	-4.21	4.2	2.35	0.005			
0.05	1.84	-4.17	4.3	2.35	0.005			
0.06	1.63	-4.29	4.0	2.35	0.005			
0.07	1.12	-4.12	3.8	2.35	0.004			
0.09	3.78	-3.91	3.1	2.34	0.004			
0.18	3.75	-3.41	2.9	2.35	0.004	0.6	2.61	0.015

deposited on polypropylene substrates. A standard sample of β-Sn foil was measured, but no phaseshift correction was found necessary.

The k^2-weighted EXAFS functions and RDFs obtained from the Sn K-edge experiments are shown figures 8.7 and 8.8 respectively. In this case, k^2 was used a weighting factor, rather than the more usual k^3, to prevent exaggeration of the statistical errors present at higher energies. During data collection, beamline 9.2 was fitted with a Si(220) double crystal monochromator. Unfortunately, at the Sn K-edge this monochromator is at the limit of its range, producing only low intensity. Consequently, this produced rather noisy spectra with only a relatively short usable data range. This resulted in difficult background subtraction and very noisy RDFs, especially at low real-space distances. However, it was possible to distinguish between real and spurious peaks in the RDFs by changing the range over which the Fourier transform was performed. The base peak observed at $\sim 1\AA$ in some of the Fourier transforms is an artifact of these background subtraction problems; but since its position clearly indicates its unphysical nature, it was preferred not to Fourier filter spectra to remove such peaks. As a consequence, this noise results in slightly larger errors on parameters obtained from the best fits, as estimated from the correlation maps (figure 8.9).

These best fit parameters are shown in Table 8.2 for the 0 – 12at.% Sn range studied at the Sn-edge. Values of $E0$ vary quite considerably from 0 to 6.64eV, while the VPI term ranges from -3.46 to -5.45eV around the value of the standard sample of -5.00eV. AFAC for this edge was fixed at the β-Sn value of 0.55. The results of interatomic distance (R), coordination number (N) and Debye-Waller factor (A) do not vary considerably within the errors, suggesting that over the whole composition range studied, Sn atoms are tetrahedrally coordinated to Si atoms. The Si-Sn interatomic

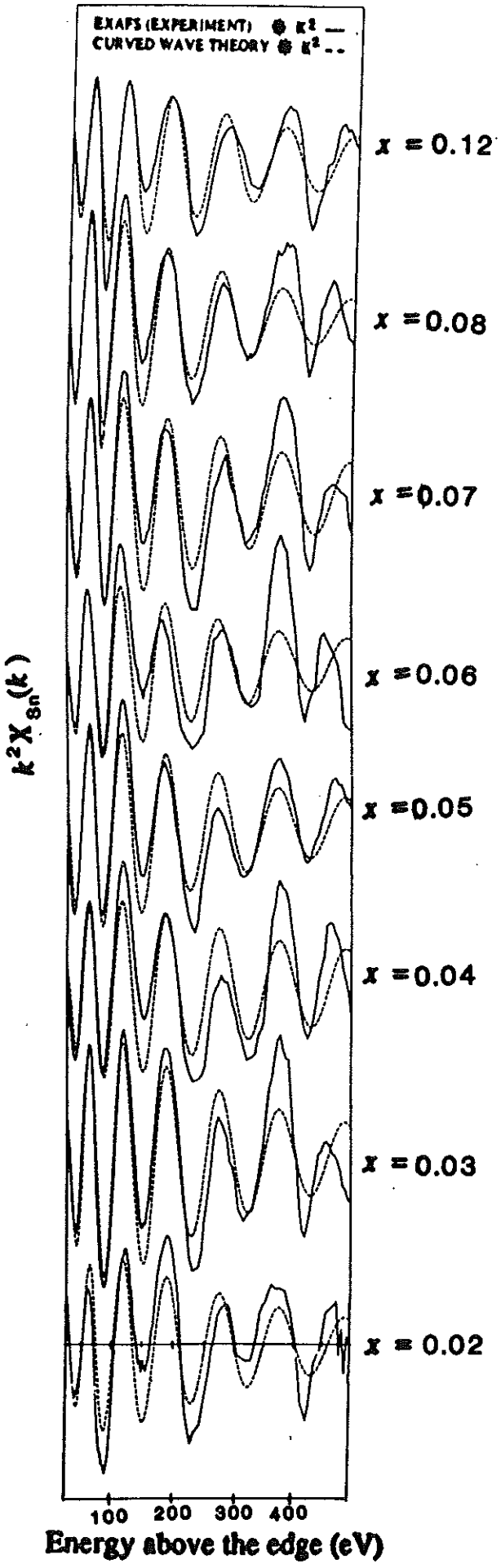

Figure 8.7: Sn K-edge EXAFS spectra for a-$Si_{1-x}Sn_x$:H.

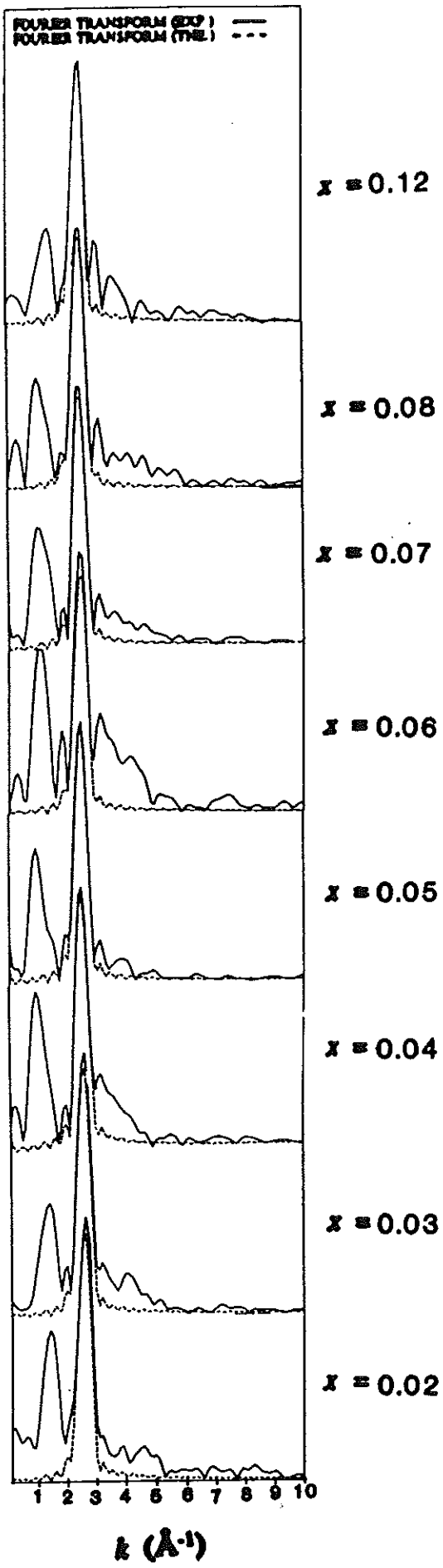

Figure 8.8: Sn K-edge Fourier transforms for a-$Si_{1-x}Sn_x$:H.

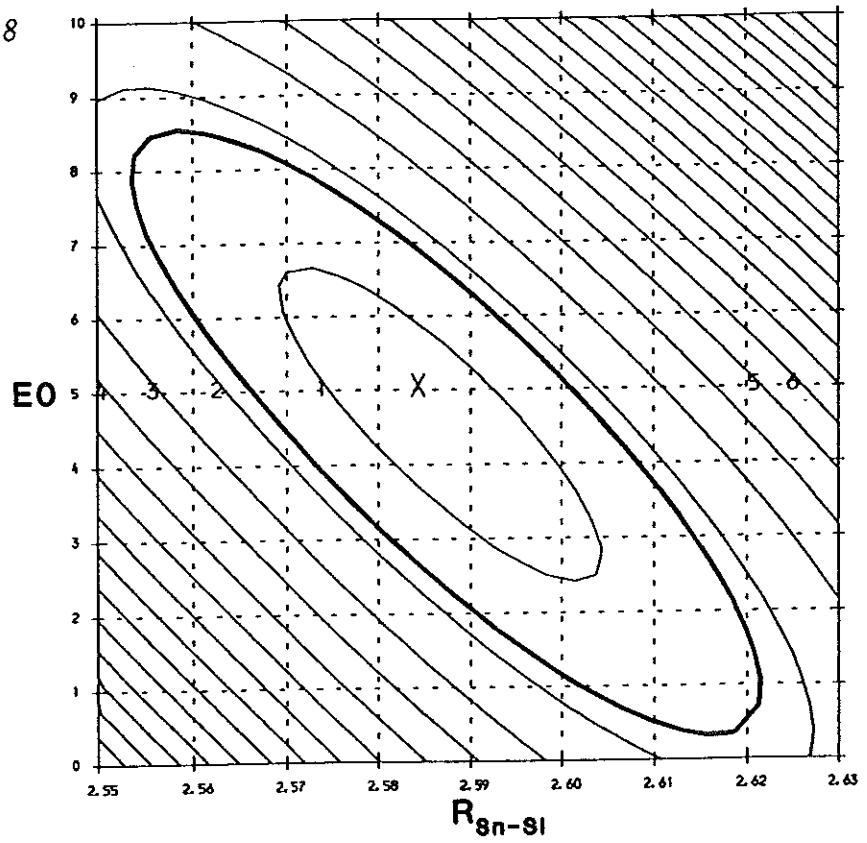

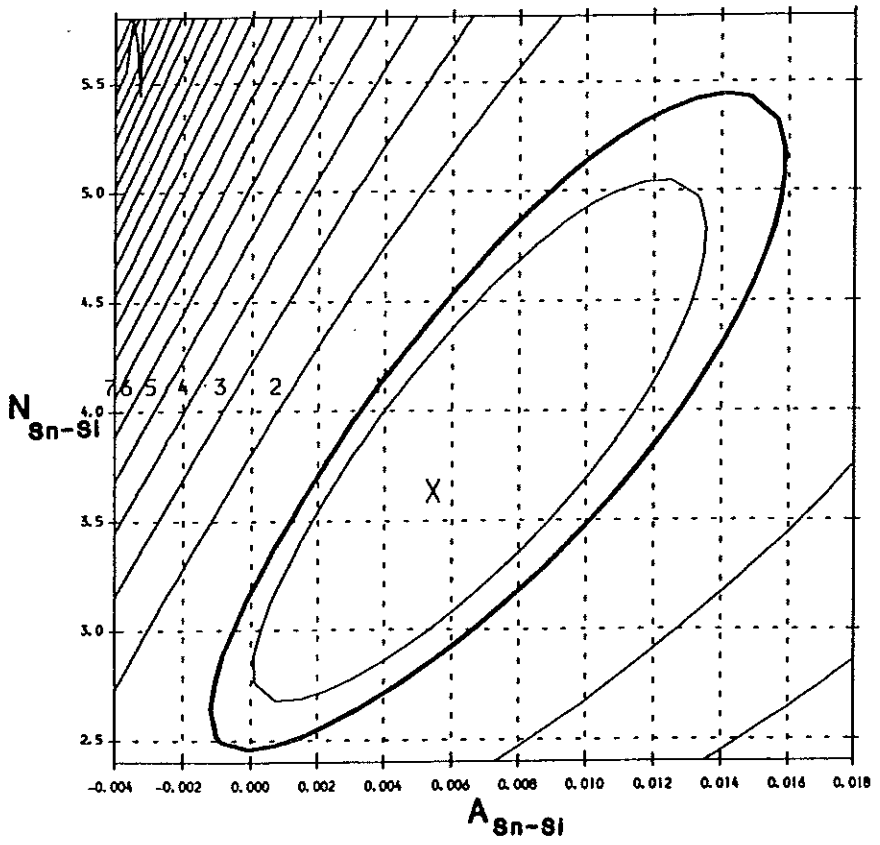

Figure 8.9: Contour map for Sn K-edge first shell (x=0.06) showing correlation between R & $E0$ and A & N.

Table 8.2 Tin K-edge EXAFS results for a-$Si_{1-x}Sn_x$:H

AFAC=0.55

x	$E0$ (eV)	VPI (eV)	N_{Sn-Si} ($\pm$1.5)	R_{Sn-Si} ($\pm$0.03Å)	A_{Sn-Si} ($\pm$0.008Å^2)
0.02	0.00	-5.05	3.3	2.60	0.008
0.03	1.24	-5.00	4.2	2.59	0.008
0.04	2.55	-4.89	3.5	2.60	0.009
0.05	4.62	-3.46	3.3	2.61	0.007
0.06	4.38	-4.31	4.2	2.59	0.007
0.07	1.42	-4.14	3.6	2.59	0.005
0.08	6.46	-4.01	4.7	2.59	0.009
0.12	3.16	-5.45	3.9	2.60	0.008

distance suggested by the Sn-edge results (2.59Å) agrees with that obtained from the Si-edge data of x=0.18 (2.61Å) within experimental error. There is no evidence of Sn-Sn correlations from the data. As Sn scatters electrons much more strongly than Si due to its much larger atomic number, the presence of sizeable clusters of Sn would be expected to feature strongly in the EXAFS spectra and it can be safely concluded that the Sn atoms do not form such clusters.

For the a-Si:H/D comparison, the 'best' values of VPI=-3.31eV and AFAC=0.7 were returned from fitting to the first shell of the c-Si standard. These values were then used in the amorphous samples' fits. The value of $E0$ for the fits was allowed to

vary and ranged between 0 and 3eV. The values of the other variable shell parameters are given in Table 8.3 with errors taken from the relevant contour maps (figure 8.10).

Table 8.3: Silicon K-edge First Shell EXAFS Results

	$N_{Si-Si}(\pm 1.0)$	$R_{Si-Si}(\pm 0.01\AA)$	A_{Si-Si} ($\AA^2$)
c-Si	4.0*	2.35*	0.002(+0.003,-0.002)
a-Si:H	4.1	2.34	0.006(+0.003,-0.002)
a-Si:D	3.4	2.35	0.002(+0.002,-0.002)

*the first shell coordination number and distance are **input** parameters and therefore fixed.

From Table 8.3, three points are evident:

1. Within the statistical errors, the first Si-Si interatomic distance is the same for the amorphous hydrogenated and deuterated samples as for c-Si, at $2.35\pm0.01\AA$.

2. There is no significant difference between the average coordination of the samples – although the Si-Si coordination in a-Si:H and a-Si:D must necessarily be reduced below four (to around 3.4 in the case of 15% hydrogen or deuterium content) because of the covalent bonding of silicon to the hydrogen/deuterium.

3. The mean squared deviation in near-neighbour distances ($\sigma^2 = A/2$) estimated from the fits are comparable for a-Si:D and c-Si, but the corresponding value for a-Si:H appears to be somewhat larger.

This third point will be discussed more fully in section 8.4.

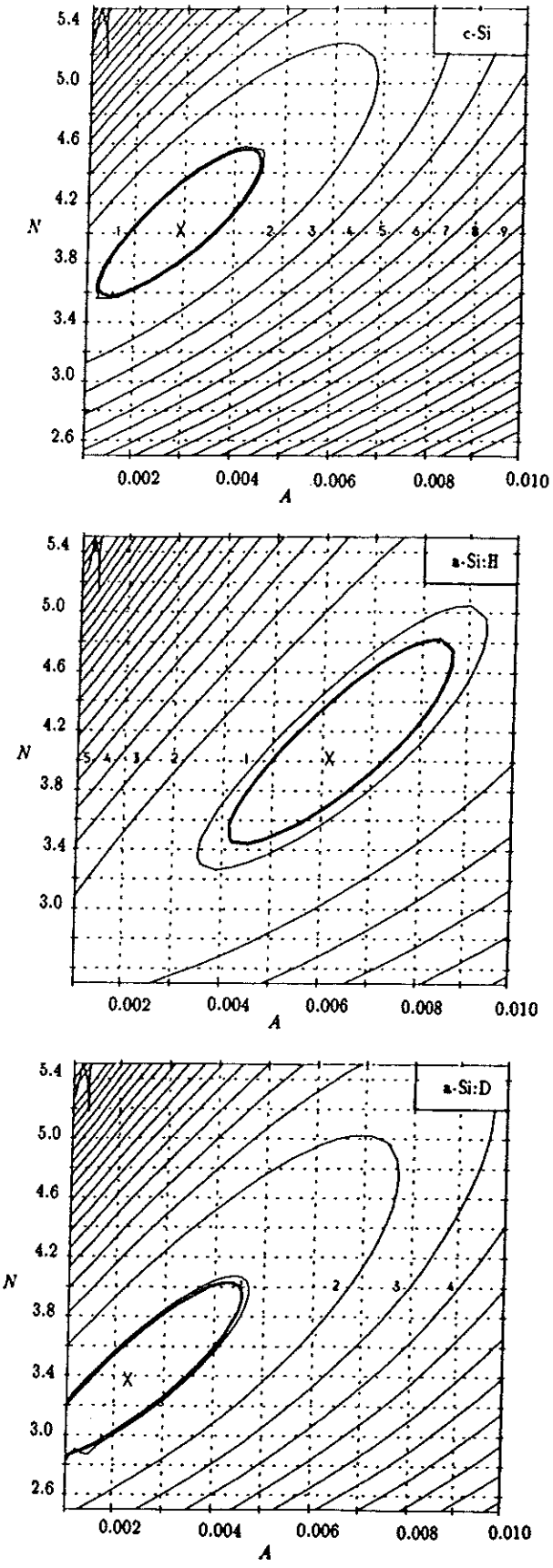

Figure 8.10: Contour maps for Si K-edge first shell of c-Si, a-Si:H and a-Si:D over the same parameter ranges, showing correlation between N & A.

During this comparison the importance of phaseshift modifications from standard samples (especially on beamline 3.4) was highlighted experimentally. Fitting to an uncorrected a-Si:D spectrum produced significantly different Si-Si distances to those previously obtained for a-Si:H. Both samples were subsequently studied again during a different experimental run, producing almost identical EXAFS phases to each other but both different to their previously obtained counterparts. These systematic phase differences can clearly be seen in the background subtracted data shown in figure 8.11. Consequently, empirical phaseshift refinements, calculated by fitting to standard sample spectra taken during the same experimental run, were applied (where necessary) to calculated phaseshifts.

The nature of the sputtering process, using in this case an Ar/H(D) plasma, makes it inevitable that some argon will be incorporated into the deposited amorphous films. The assumption is generally made that the argon resides at random sites within the a-Si:H matrix. No direct structural measurements have been made, however, to verify this assumption. Ar K-edge data were collected from beamline 3.4 by the electron drain current method, using Ge(111) monochromator crystals. Although a clearly defined Ar K-edge is observed (see figure 8.12), the statistical accuracy of the data was too poor to allow a detailed analysis. However, the EXAFS oscillations are weak and are attenuated very rapidly beyond the edge and this observation alone is sufficient to provide a clear indication of a highly disordered argon environment. It should be noted that other workers in the area have failed to detect the presence of argon at all [112].

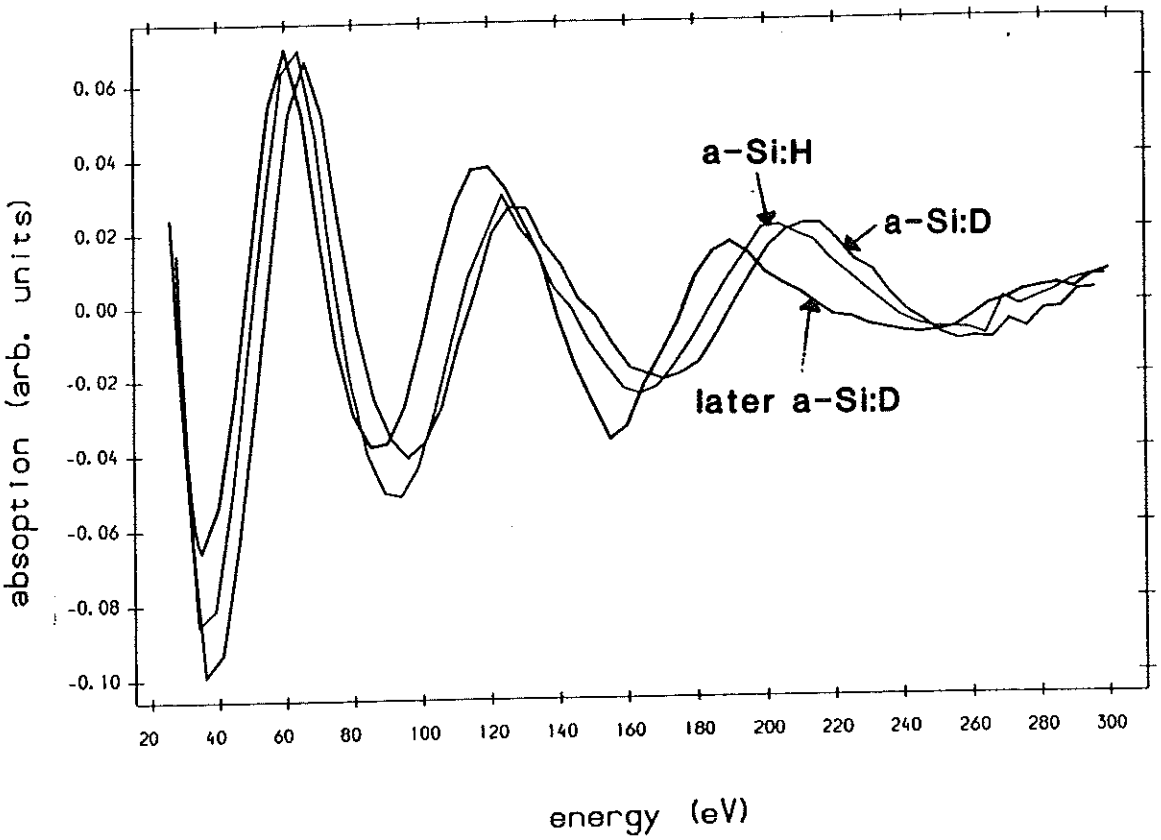

Figure 8.11: Comparison of the Si K-edge EXAFS phases of a-Si:H and a-Si:D taken at different times on beamline 3.4.

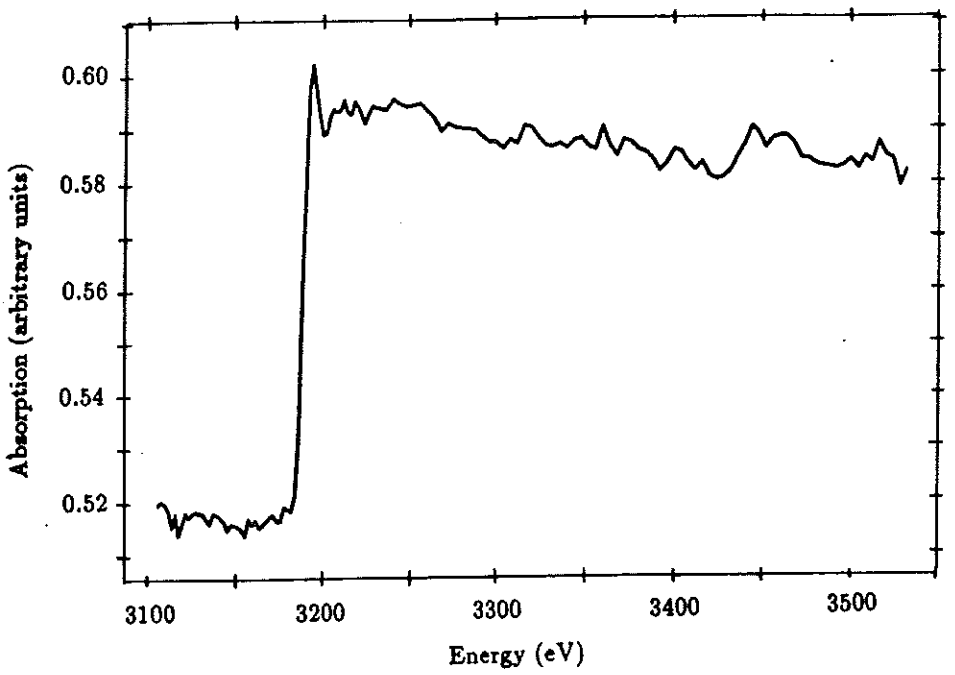

Figure 8.12: Raw Argon K-edge EXAFS spectrum.

8.4 Discussion

EXAFS results on the a-$Si_{1-x}Sn_x$:H system indicate that Sn atoms are substitutionally incorporated into the host a-Si:H network in the composition range $0< x <0.18$. This is in agreement with the preferential tetrahedral coordination of Si atoms to each Sn atom observed by Vergnat et al. [123] in co-evaporated samples. It should also be noted that there was no evidence of interstitial Sn incorporation as reported by Weyer et al. [138] from ion implantation studies. No significant contribution from Sn-Sn correlations was observed in this low Sn concentration range, although smaller contributions may have been obscured by the poor quality of the data. The lack of β-Sn crystallites corroborates the fact that a transition to metallic conduction was not observed by conductivity measurements. At least some of the Sn atoms would need to be incorporated in a metallic form for such an MIT to occur. The formation of β-Sn clusters has been observed by others to begin anywhere between 22at.% Sn [119] and 55at.% Sn [123]. Furthermore, there is no evidence for the formation of silicide-like regions of the form observed in Chapter 7 for a-SiNi:H. Rather, the system appears to be completely homogeneous and the Si-Sn interatomic distances returned by the fits agree within errors with with that suggested by a naive addition of the Si (1.18$\AA$) and Sn (1.40$\AA$) covalent atomic radii. The lack of evidence for Si-Sn correlations for x <0.09 in the Si-edge EXAFS results is not surprising since the results represent a structural average over the whole sample. Assuming the substitutional inclusion of Sn atoms, the structure would be expected to be dominated by Si-Si interactions for low levels of doping. In this mechanism, it is necessary for there to be ~25at.% Sn in order that each Si could be bonded to a Sn atom; the Si-Si partial coordination decreasing as the Si-Sn coordination increases.

The lack of di- or tri-valently bonded Sn appears to be supported by the IR results

where no Sn-H bonds were observed. Since conductivity measurements performed on these samples suggest an extended to localized state conduction transition (explained by the non-tetrahedral incorporation of Sn) at ~3at.% in agreement with others [117, 120, 121, 127], there appears to be some contradiction between results. However, the optical result has already provided the possible explanation that in the absence of sufficient H_2 to saturate all dangling bonds in the system, hydrogen will preferentially bond to the Si sites. Furthermore, other workers [117] have suggested that only a small percentage of the Sn atoms need to be incorporated in a non-tetrahedral fashion to cause the transition; the majority of the remaining Sn being incorporated substitutionally. If this is the case, then the average structure determined by EXAFS is unlikely to observe this small proportion. It can be noted that the existence of two, inequivalent Sn sites has also been observed for the growth of Sn on Si(100) [139], changing from mainly divalent to predominantly tetravalent bonding configurations with increasing coverage.

The interatomic distances and coordination numbers returned from the comparison of a-Si:H and a-Si:D are, as expected, very similar. However, there appears to be a relatively large difference in the mean squared deviation of near neighbour distances (σ^2).

This result is a little surprising since EXAFS contains significant information only on local, first-neighbour environments: the spread in bondlengths in a-Si:H is very small ($\sim 1\%$) and vibrational disorder in a covalently bonded system is unlikely to be affected strongly by the small local mass change associated with hydrogen – deuterium isotopic substitution. In fact, thermal vibrations in the amorphous sample are of about the same order as for the crystal (as can be seen from comparison of a-Si:D and c-Si). The difference in σ^2 can be investigated further by taking a point

by point ratio of background subtracted spectra. The ratio (r), of the two spectra (a and b) is given by:

$$r = \alpha \exp(-2\triangle\sigma^2 k^2) \tag{28}$$

where α = constant involving coordination numbers

$\triangle\sigma^2$ = difference in mean squared deviations in near-neighbour separations.

Hence, the $\triangle\sigma^2$ term can be obtained from the gradient of the ratio plotted as a function of energy. The errors on the ratio of coordination numbers are large and have not, therefore, been investigated. Although only providing *relative* results, this method is useful for gauging if differences indicated by the fitting of the EXAFS data are indeed significant, since it uses the raw, background subtracted data and is therefore less susceptible to the uncertainties that can arise from curve-fitting. Performing this ratioing on combinations of our three samples and fitting a least squares straight line to the data we obtained the results shown in Table 8.4.

Table 8.4 Results obtained from ratioing of background subtracted spectra

a/b	$\triangle\sigma^2$ ($\AA^2$)
a-Si:H/c-Si	$2.7(\pm 0.7) \times 10^{-3}$
a-Si:D/c-Si	$0.2(\pm 0.05) \times 10^{-3}$

These differences indicate that there is, after all, a slight difference between the mean squared deviations in bond-length of a-Si:H and a-Si:D. Since the value of the $\triangle\sigma^2$ term for a-Si:H is comparable to those for the metal containing samples, it appears that it is the low value returned for the deuterated sample that is uncharacteristic. This reduction in the bond-length variation indicates that there is less static disorder in the a-Si:D sample; but since the total electron yield measurement only probes the top 50 - 100$\AA$, this may be only a surface effect.

8.5 Conclusion

The structural study of the a-$Si_{1-x}Sn_x$:H system concludes that the majority of the Sn atoms enter the a-Si:H TRN in a substitutional manner in the $0< x <0.18$ composition range; Si-Si and Si-Sn bondlengths being those expected for a covalently bonded system. Electrical conductivity measurements indicate the possibility of the incorporation of some Sn in non-tetrahedral site causing a transition from extended to localized state conduction at ~3at.% Sn. Since it is difficult to prepare samples of accurate composition in this region by plasma deposition techniques, it would be useful to alter the preparation conditions to produce this transition at a higher metal content as indicated by others [119, 124]. Such films could then be studied over the transition more easily by a variety of methods. Due to the possible low percentage of Sn atoms directly responsible for the transition, EXAFS alone is not ideally suited to a structural study of such a system since it can only return the parameters of an average performed over the whole sample. Clearly it would have been advantageous to have performed a more comprehensive photoelectronic study on this system and to have extended the composition range investigated.

The X-ray based study of both a-Si:H and a-Si:D confirms that the average first shell interatomic distance and the total coordination number in a-Si:H are the same as those in c-Si; and this does not change upon isotopic substitution of the hydrogen, for samples prepared under identical conditions. The presence of Ar in the samples, incorporated during film deposition, has also been confirmed and it is clear that the Ar atoms occupy random sites in the amorphous network.

Chapter 9

Amorphous Germanium:Gold Thin-Films

9.1 Introduction

The equilibrium diagram of the Ge-Au alloy system is known to show a deep eutectic at around 27at.% Ge [140], but it is impossible to make crystalline alloys of Ge and Au over a wider composition range due to phase separation. However, amorphous alloys offer the unique possibility to study the properties of such immiscible solid species since it has been found possible to prepare $Ge_{1-x}Au_x$ alloys in an amorphous state around the eutectic value ($0.6< x <0.8$) [141] and below 20at.% Au content [142, 143, 144].

The a-Ge:Au system is also known to exhibit a metal-insulator transition with increasing gold content, and this has been the motivation behind most of the experimental work performed on the material to date. Impurities such as Au are known

to produce deep, localized states in the c-Ge band-gap and investigations on similar systems indicated that this was also the case in a-Ge [145], suggesting that any MIT could be expected at relatively high metal concentrations (*i.e.* 10 – 30at.% Au) [15]. The metal-insulator transition in both amorphous and polycrystalline films of flash-evaporated $Ge_{1-x}Au_x$ was studied by Dodson et al. [142] who determined the critical value of x to be above 0.18 for the polycrystalline samples, but somewhat lower ($\sim$0.12) for purely amorphous films. Later work from the same laboratory [143] concluded that the conductivity mechanism changed from variable range hopping to metallic over this transition. Furthermore, the work also suggests some migration of the gold at room temperature and the formation of some metastable, crystalline phase above 24at.% Au. This migration is not unfeasible considering the high diffusivity of Au in other c-semiconductors such as silicon, where the diffusion is generally ascribed to the motion of interstitial gold [146]. Further electronic studies [144] suggested that the conductivity is very sensitive to gold clustering and percolation conduction may occur along Au-rich links. X-ray diffraction spectra also reveal that films with x <0.19 are relatively thermally stable at room temperature and there is little evidence of crystallite growth with successive annealing.

It is the thermal stability, and in particular the fractal crystallization of the amorphous Ge/polycrystalline Au (a-Ge/p-Au) system, that provides most of the remaining electronic data, and the majority of the structural data available for the Ge:Au system. TEM work on evaporated a-Ge/p-Au films, intermixed at the interface by Si ion bombardment [147], indicated the composition of the interface region to be roughly $Au_{60}Ge_{40}$ before annealing. This and other work [148, 149] suggests that the crystallization temperature of a-Ge is markedly decreased in the presence of Au. Electron diffraction work on co-evaporated, high Au content (60–80at.% Au) samples

annealed at room temperature [141] found evidence for both a-Ge covalent bonds and large crystallites of a tetragonal phase alloy below 65at.% Au. This metastable alloy was observed to be identical to that reported for the melt-quenched alloy of approximate composition $Au_{60}Ge_{40}$ [140].

a-Si:Au

While relatively little work has been performed on the a-Ge:Au system, its group IV counterpart, a-Si:Au, has been extensively studied; though, as for a-Ge:Au, most of these investigations have centred around the MIT (generally reported at around 14at.% Au in a-Si:Au at low temperatures [150, 151, 152]). All of these authors report conductivity via variable range hopping in the insulating regime, and whilst some [151, 153] have suggested that the transition is of Anderson-type, others [150] have speculated that, conductivity may take place along quasi one-dimensional Au channels. Huber and von Allmen [154] consider both points of view, but cannot decide whether a transition of Anderson or percolation type is relevant for the a-Si:Au system on the evidence available.

Nishida et al. [152] also investigated their samples by electron microscopy and observed that above 30at.% Au the films contained microcrystallites of gold, whilst below 21at.% Au the films were homogeneous in the length scale of a few hundred $\AA$ and showed a TRN of Si atoms. This had been the conclusion of Kishimoto and Morigaki [155] whose optical studies determined that 30at.% Au was also the composition at which the optical band-gap finally disappeared. The difference between the MIT as determined by conductivity measurements ($\sim$14at.% Au) and optical measurements ($\sim$30at.% Au) was discussed by Hauser et al. [156] who attributed this discrepancy

to the inhomogeneity of the samples and the different ways in which the averaging occurs in the two cases — the dc current preferentially seeking out the higher conductivity paths, whilst the averaging is more uniform in the optical measurements. This would tend to suggest structural inhomogeneity occurring well below 30at.% Au and conduction via a percolation mechanism as previously considered. Crystallization studies show that for $0.2< x <0.7$, a-$Si_{1-x}Au_x$ films crystallize to c-Si and a metastable c-Si:Au alloy, while below $x \sim 0.2$ the first crystallization stage produces c-Si and possibly an amorphous Si:Au phase [157], the presence of the Au lowering the a-Si crystallization temperature. Density measurements from the same laboratory [158] leads to the suggestion of a homogeneous alloy of a-Si with interstitial Au atoms for $x <0.1$. However, even on the a-Si:Au system there are no known direct structural observations in this low gold region.

Evidently it would be beneficial to the full understanding of both optical and electronic transport phenomena to obtain direct information on the structural changes accompanying their respective transitions. Accordingly, EXAFS experiments have been performed to probe the local environments of both the Ge and Au atoms in a series of a-$Ge_{1-x}Au_x$ samples over the composition range $0< x <0.37$, where such transitions might be expected to occur.

9.2 Sample Preparation and Characterization

Thin-film samples of a-$Ge_{1-x}Au_x$ were prepared by rf co-sputtering onto unheated polypropylene substrates of thickness 0.02mm. The deposition parameters used were similar to those presented in Table 4.1, except that the films were not hydrogenated to aid qualitative comparison with previous work on this system. Gold concentration

was altered by varying the number of 99.99% pure Au pieces on a c-Ge target. Electron microprobe analysis was unable to provide the sample compositions accurately due to the similar energies of the Ge K and Au L_3 X-ray lines (11.1 and 11.9keV respectively), although compositional trends were apparent and consistent with those taken from the amount of gold placed on the target; hence concentration values were determined by Rutherford backscattering. However, scanning electron microscopy investigations did establish that there were no large Au clusters. No direct probe for crystallinity was applied immediately after deposition, but work on a-$Si_{1-x}Au_x$ [159] had indicated that sputtered amorphous films with x <0.87 were stable at room temperature. Indeed, it was concluded that films prepared by this technique are more stable than those produced by splat-quenching; this increased stability being attributed to the incorporation of ~1at.% Ar during deposition. Compositional analysis performed on the films used in the work presented here revealed low proportions of Ar in all the samples.

Immediately after deposition, all films had a shiny, silver coloured appearance (like a-Ge itself); but after several months (and before any of the main experimental work could be carried out) the samples were observed to develop a yellowish-brown hue. This, according to Hauser and Tauc [159] is direct evidence of crystallinity. For their samples, all in the high gold content region (x >0.5), crystallization lead to X-ray diffraction spectra showing peaks characteristic of c-Au. Limited XRD experiments performed on some of the samples reported on in this chapter [160, 161], using the Cu K_α radiation from a laboratory source, showed small Bragg peaks, consistent with the presence of Au clusters, only for x >0.21. More pronounced Bragg peaks evident in the XRD spectra of these higher Au content samples are consistent with the tetragonal (γ), metastable $Au_{60}Ge_{40}$ crystalline phase (see Figure 9.1). It should be

noted that even theses peaks are still relatively small, though clearly distinguishable from the diffuse scatter. None of the $x \leq 0.21$ samples appeared to show characteristic c-Au peaks, but all showed some very low intensity, sharp features superimposed on the diffuse scatter, indicative of a fraction of crystallinity at all compositions. The pure Ge film was found to remain wholly amorphous with time.

9.3 EXAFS Results and Interpretation

Extended X-ray absorption fine structure measurements were made at both the Ge K- and Au L_3-edges of a-$Ge_{1-x}Au_x$ over the composition range $0 < x < 0.37$ using beamline 7.1 of the SRS. All experiments were performed in transmission; the optimal ratio of post to pre-edge absorption being achieved by stacking several samples together.

The Ge K-edge k^3-weighted EXAFS functions and corresponding radial distribution functions are shown in figures 9.2 and 9.3, where it can be seen that the phase of the functions remains fairly constant over the whole composition range. However, the radial distribution functions show a slight reduction in amplitude with increasing Au content; though this may be due, in part, to the gradual increase in sample absorption as the metal proportion rises. All the RDFs show a single peak at 2.45$\AA$, characteristic of a-Ge, and there is no evidence of Ge-Au correlations in any of the plots.

A summary of the results obtained from theoretical fits to the Ge K-edge experimental data is given in Table 9.1. The value of AFAC was fixed at the value of 0.73 obtained from analysis of the a-Ge sample. The parameters VPI and $E0$ were allowed to float freely. However, VPI was found to remain roughly constant at the

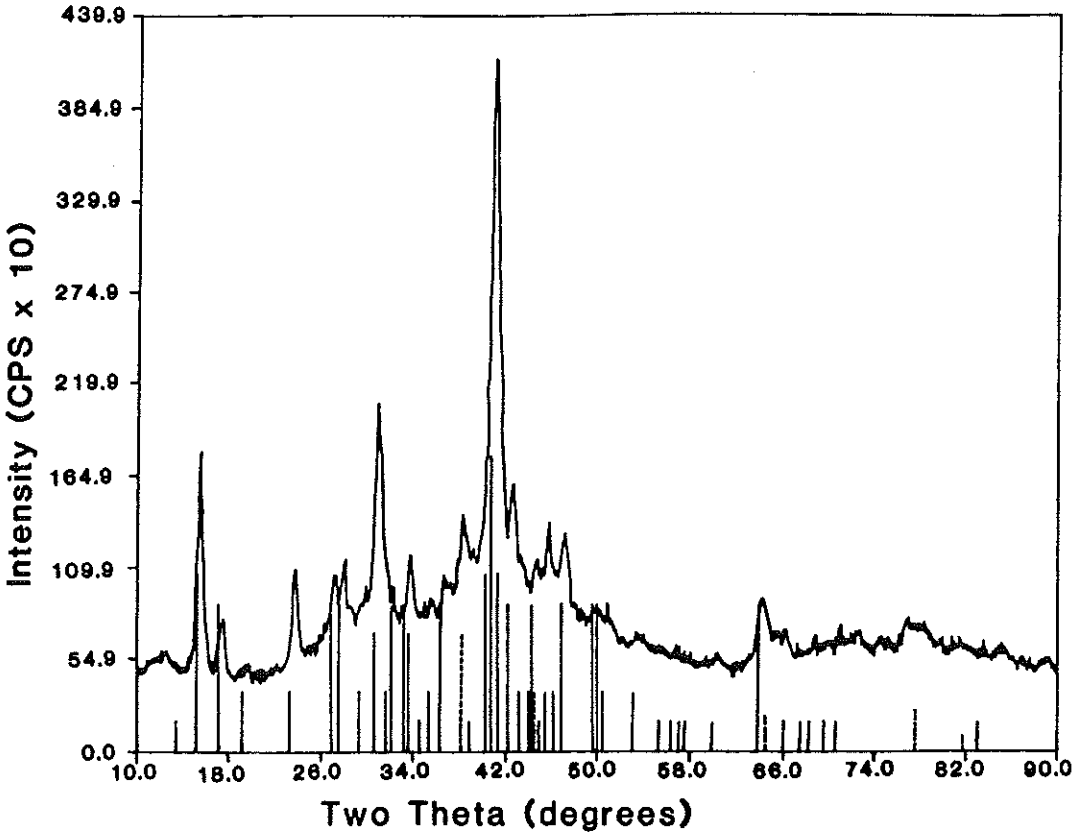

Figure 9.1: X-ray diffraction spectrum [160] of x=0.33 sample. The γ-$Au_{60}Ge_{40}$ lines (unbroken) [140] and c-Au lines (dashed) are shown for comparison.

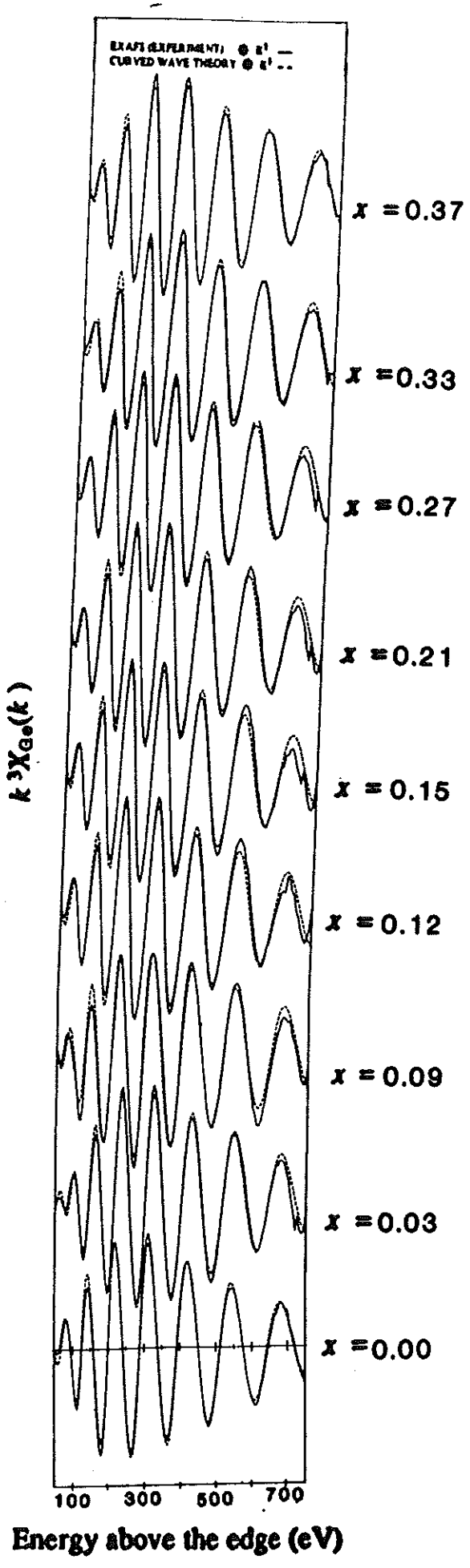

Figure 9.2: Ge K-edge EXAFS spectra for a-$Ge_{1-x}Au_x$.

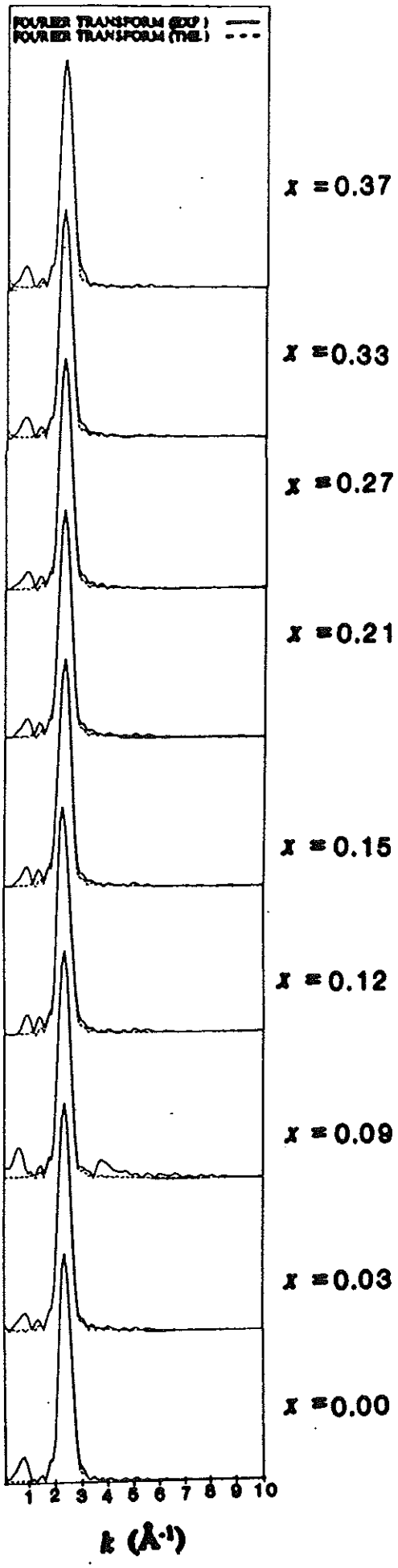

Figure 9.3: Ge K-edge Fourier transforms for a-$Ge_{1-x}Au_x$.

a-Ge sample value of -1.6eV while $E0$ varied between 5.4 and 7.9eV for the Au containing samples. The a-Ge standard sample was also used to verify the theoretically calculated Ge scattering phaseshifts. Errors indicated in the table are, once again, those taken from the 5% line of significance of correlation maps such as those in figure 9.4. The parameters presented in Table 9.1 reinforce the conclusions drawn from the experimental spectra that the Ge-Ge coordination is dominant, with an interatomic distance of 2.45$\AA$ returned for all values of x. Whilst no Au is apparent at any composition, the Ge-Ge coordination appears to decrease slightly as x increases, although it does not differ substantially from four, indicating the presence of an a-Ge TRN over the whole alloy range.

The k^3-weighted EXAFS functions and RDFs for the Au L_3-edge are presented in figures 9.5 and 9.6. These plots clearly indicate a change in the local environment of the Au atoms taking place as their concentration in the system is increased. Au-Ge and Au-Au peaks are clearly visible in the RDFs at approximately 2.60 and 2.84$\AA$. It can be seen from figure 9.6 that as the proportion of Au in the sample is increased, the relative sizes of the Au-Ge and Au-Au peaks in the RDFs changes, the Au-Au peak becoming more prominent. The change of structure is also reflected in the change of both phase and amplitude of the EXAFS functions. The low R peaks in the RDFs are caused by background subtraction errors and high frequency noise in the experimental spectra. These, and other, spurious peaks were distinguished from physically meaningful peaks in the RDFs by changing the range over which the Fourier transform was performed.

The results obtained from the the Au L_3-edge experimental data are summarized in Table 9.2. For this edge , AFAC was fixed at the value of 0.4 obtained from a standard sample of c-Au which was also used to check the accuracy of the calculated

Table 9.1 Germanium K-edge EXAFS results for a-$Ge_{1-x}Au_x$

AFAC=0.73

VPI=-1.6eV

x	$E0$ (eV)	N_{Ge-Ge} (± 0.5)	R_{Ge-Ge} (± 0.005Å)	A_{Ge-Ge} (± 0.001Å^2)
0.00	10.1	4.1	2.45	0.012
0.03	7.9	4.3	2.46	0.012
0.09	7.1	4.1	2.45	0.011
0.12	6.7	3.8	2.45	0.011
0.15	6.6	3.7	2.45	0.013
0.21	5.4	3.8	2.46	0.014
0.27	7.1	3.8	2.46	0.014
0.33	6.7	3.8	2.46	0.011
0.37	7.1	3.3	2.45	0.013

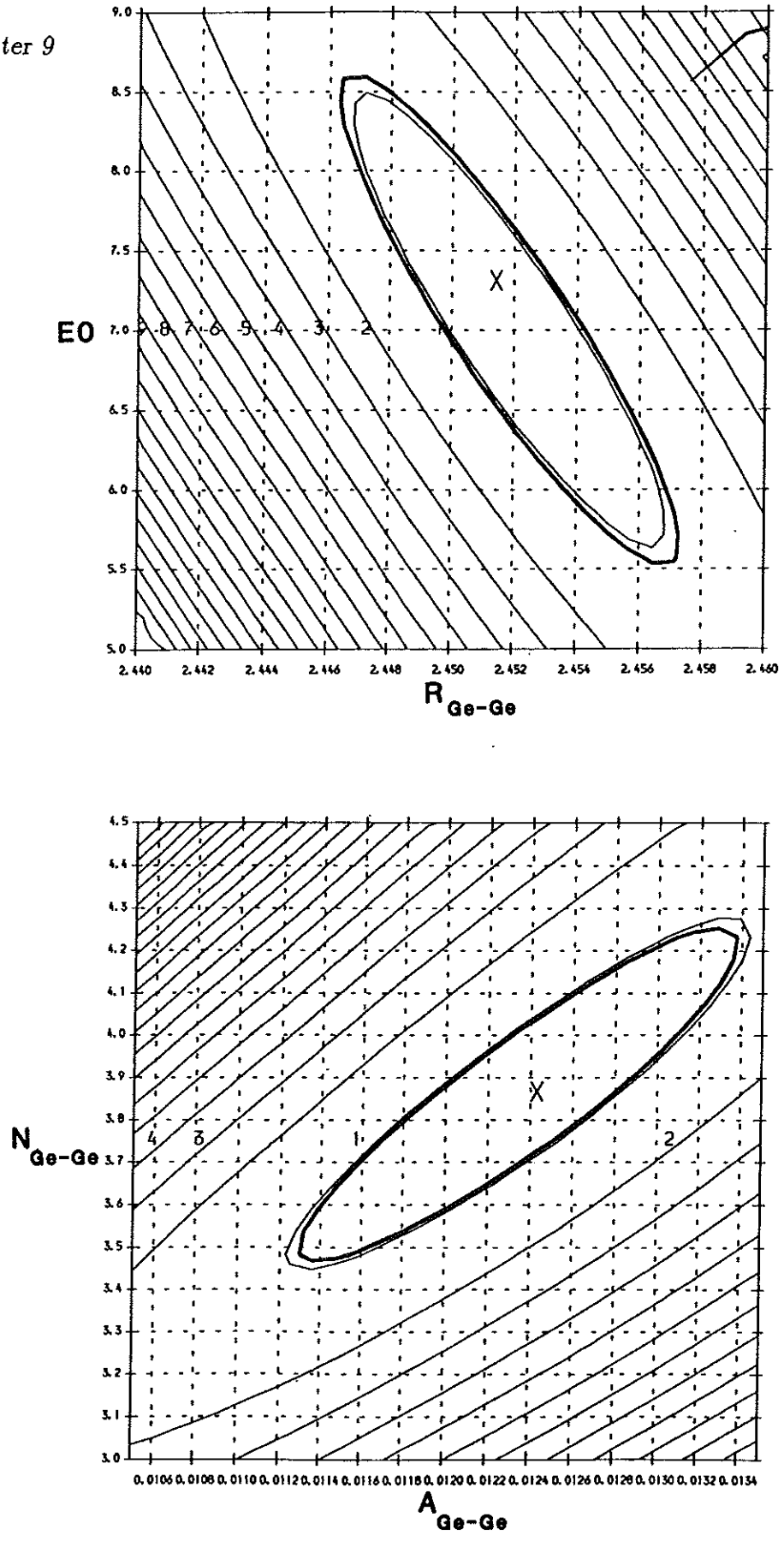

Figure 9.4: Contour maps for Ge K-edge first shell (x=0.15) showing correlation between R & $E0$ and A & N.

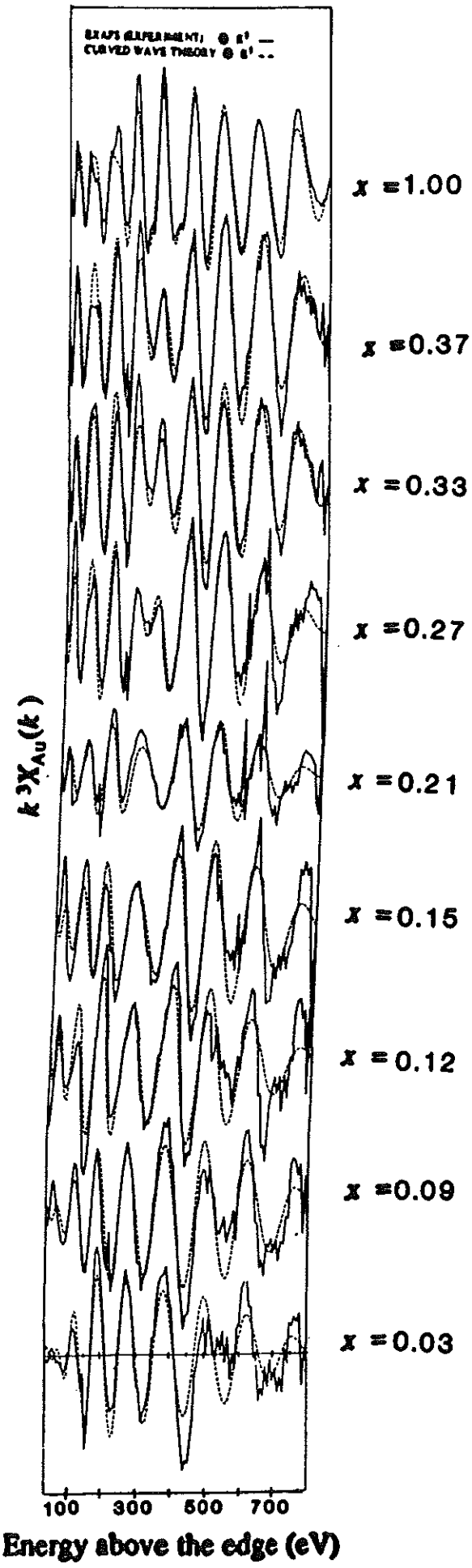

Figure 9.5: Au L_3-edge EXAFS spectra for a-$Ge_{1-x}Au_x$.

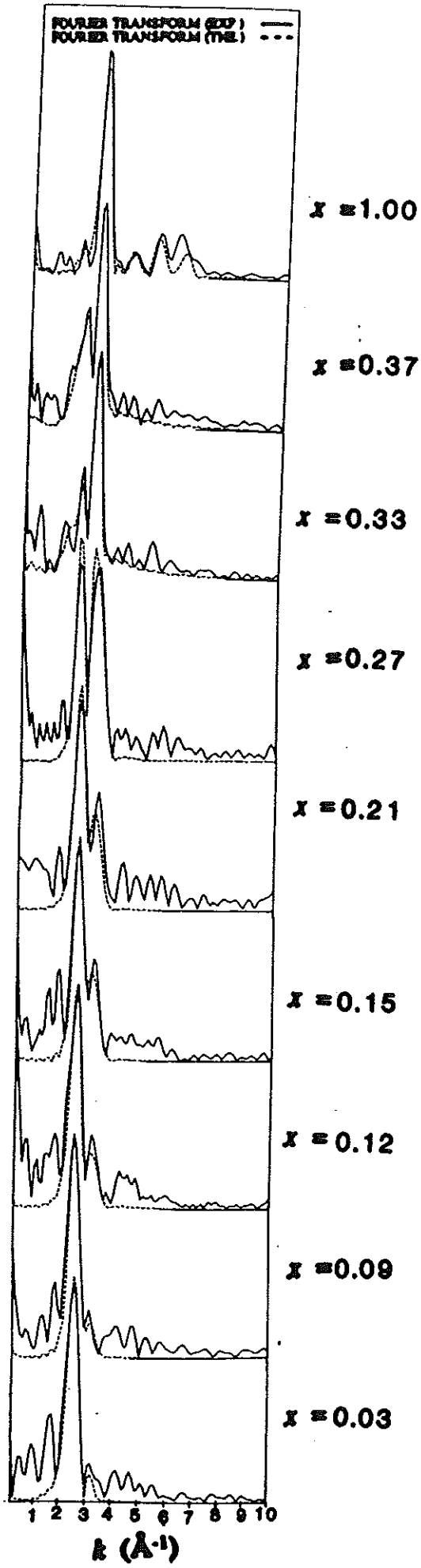

Figure 9.6: Au L_3-edge Fourier transforms for a-$Ge_{1-x}Au_x$.

Au scattering phaseshifts. Whilst the value of $E0$ varied quite considerably from 0.2 to 12.3eV, VPI remained close to the -3.7eV value obtained from the standard foil. The decision as to whether or not to fit another shell to the data was taken using the criteria of Joyner et al. [72]. Figure 9.7 shows examples of the correlation maps used to determine the errors quoted in Table 9.2. The parameters in this table indicate that for $x \leq 0.21$ the Au-Ge and Au-Au coordination numbers are similar and do not vary appreciably with composition. The Au-Ge (2.59$\AA$) and Au-Au (2.84$\AA$) interatomic distances are also independent of composition in this range. However, the observation of Au-Au correlations, even in the sample containing as little as 3at.% Au, indicates that the Au atoms must be aggregating in some way; the low Au-Au coordination number and its similarity to the Au-Ge coordination number suggesting formation of regions of a Au:Ge alloy. For samples with $x > 0.21$ the Au-Au coordination number is increased, as are both the Au-Au and Au-Ge interatomic spacings. In particular, the Au-Au interatomic distance is seen to approach the value of 2.88$\AA$ observed in bulk gold, suggesting the metallic clustering of these atoms in the more metallic films.

9.4 Discussion

The lack of any evidence for the presence of Ge-Au correlations and the fact that the Ge K-edge EXAFS spectra do not vary with composition and can be modelled very well using only the structural parameters of a-Ge indicates that the a-Ge TRN persists over the whole alloy range investigated. However, the Au-edge results indicate the formation of a Au:Ge alloy. The conclusion that the system is comprised of an a-Ge matrix containing an intermetallic alloy is consistent with the observations on a-$Si_{1-x}Ni_x$:H (Chapter 7) and a-$Ge_{1-x}Mo_x$ [112], but while these systems appear to have been totally amorphous at low metal concentrations, there is evidence of partial

Table 9.2 Gold L_3-edge EXAFS results for a-$Ge_{1-x}Au_x$

AFAC=0.4

VPI=-3.7eV

x	$E0$ (eV)	N_{Au-Ge} (± 1.0)	N_{Au-Au} (± 1.0)	R_{Au-Ge} ($\pm 0.02\AA$)	R_{Au-Au} ($\pm 0.02\AA$)	A_{Au-Ge} ($\pm 0.005\AA^2$)	A_{Au-Au} ($\pm 0.005\AA^2$)
0.03	0.2	1.3	1.0	2.58	2.84	0.010	0.017
0.09	8.6	2.1	1.8	2.59	2.84	0.018	0.018
0.12	8.1	2.4	2.2	2.59	2.84	0.015	0.023
0.15	8.0	1.3	2.2	2.59	2.84	0.010	0.016
0.21	9.7	2.4	2.6	2.59	2.84	0.016	0.015
0.27	12.3	1.9	5.6	2.59	2.85	0.015	0.020
0.33	10.7	3.4	5.1	2.62	2.86	0.015	0.022
0.37	10.1	1.3	4.9	2.62	2.86	0.012	0.017
1.00	14.4	-	12.2	-	2.88	-	0.014

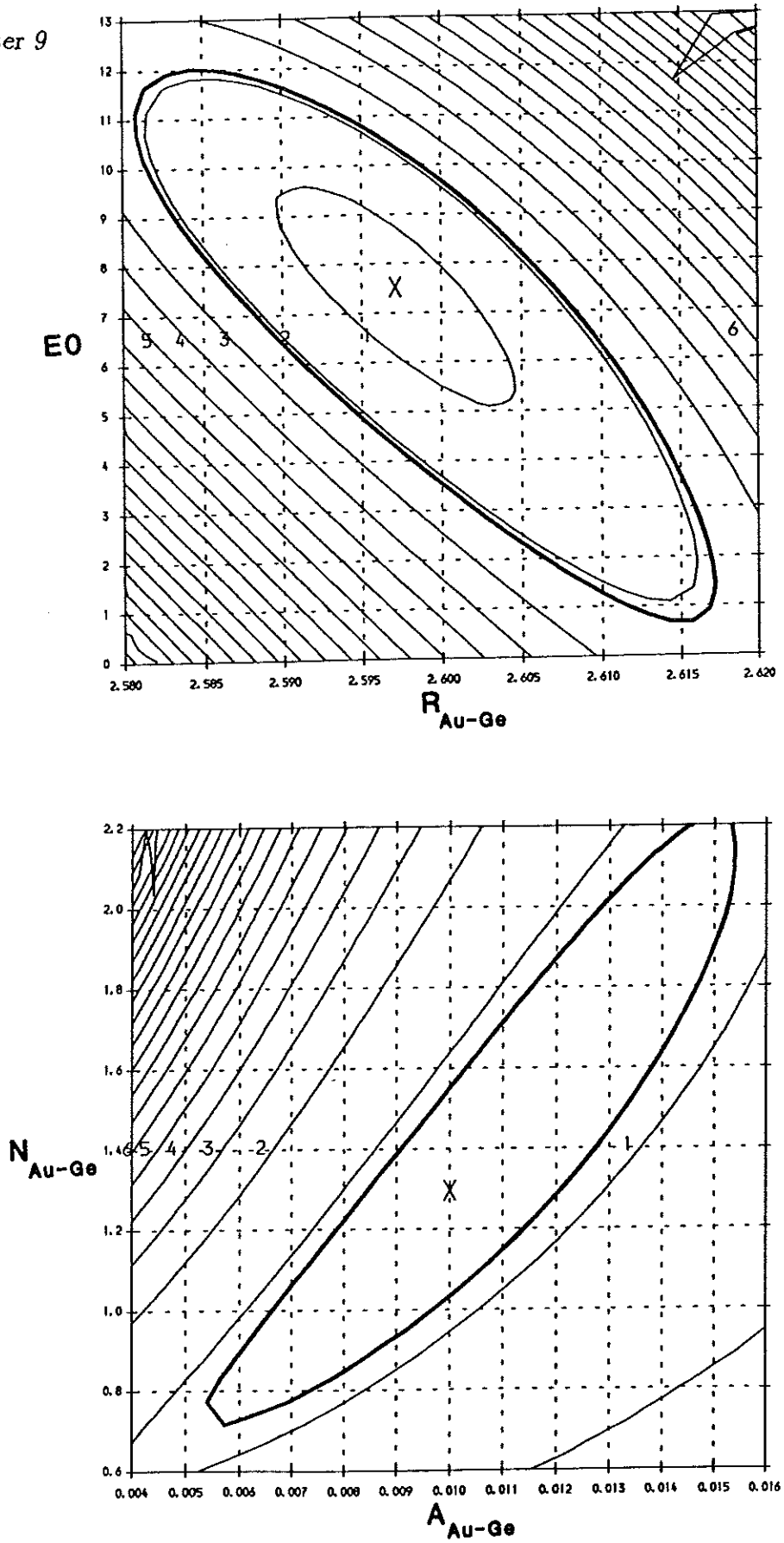

Figure 9.7: Contour maps for Au L_3-edge first shell (x=0.15) showing correlation between R & $E0$ and A & N.

crystallinity in all the Au containing samples. It is probable that the samples were completely amorphous on deposition, but became partially crystalline on annealing at room temperature for several months as is supported by the gradual change in colouration observed for the films. Since Osofsky found evaporated samples within this composition range to be thermally stable at room temperature [144], this suggests that it is more likely to be the deposition technique and parameters used rather than the mere incorporation of argon that enhances thermal stability. Below x=0.21 the fraction of crystallinity is very small and the majority of scattering is still diffuse. This makes it very difficult to determine the nature of the crystallinity, but peak positions do not correspond to c-Au. It should also be noted that there was no evidence of c-Ge in any of the films' XRD spectra and EXAFS results indicate the existence of a-Ge even at x=0.37. This suggests that the Au:Ge alloy formed is less stable than the a-Ge TRN in the presence of Au, as opposed to the case of a-Si:Au where, below x=0.2, the first crystallization stage produced c-Si [157]. The presence of a-Ge at compositions up to 37at.% Au can be contrasted with the case of a-Ge:Mo [112] where all indications of tetrahedral a-Ge (*i.e.* Ge-Ge correlations) disappear at about 23at.% Mo.

The presence of Au-Au correlations at all compositons indicates that a homogeneous system does not exist for the Ge:Au alloy, even at x <0.1 as suggested for a-$Si_{1-x}Au_x$ [158]. The contraction of the interatomic spacings from those expected by a simple addition of atomic radii (Au-Ge:2.66$\AA$ and Au-Au:2.88$\AA$) suggests the existence of strong interatomic interactions. To summarize, it is postulated that, in the composition range $x \leq$0.21, the samples consist of regions of a Au:Ge alloy surrounded by an a-Ge TRN.

For samples with x >0.21, the Au-edge EXAFS data are indicative of the formation of small (explaining the comparatively low Au-Au coordination numbers) clusters of Au. Indeed, in this composition region, XRD spectra (*e.g.* figure 9.1) show small Bragg peaks consistent with this conclusion. Furthermore, other Bragg peaks on the spectra correspond well to those produced by the metastable γ-$Au_{60}Ge_{40}$ alloy as observed by others [140, 147, 141]. These results corroborate the suggestion of a metastable c-phase at high Au content made by Dodson et al. [142] and are also similar to those of Nishida et al. on a-Si:Au who observed c-Au above 30at.% Au [152]. The apparent elongation of the Au-Ge bond lengths may be explained by considering the fact that EXAFS measurements are an average over the whole sample. If a sizeable proportion of the incorporated Au takes the form of small clusters of c-Au embedded in but not bonded to a-Ge and the remaining amount is included as an Au:Ge alloy,when the metallic clusters appear then the non-bonding Au-Ge distance will start to contribute to the measured Au-Ge distance. Since the observed Au-Ge distance appears to increase, the distance between Au atoms on the outside of the Au clusters and Ge atoms in the remaining TRN must be greater than the Au-Ge bond lngth in the alloy regions. Hence, in the higher composition range (0.21< x <0.37) it is concluded that the samples consist of an a-Ge TRN surrounding small clusters of Au and also regions of a Au:Ge alloy whose crystalline phase appears to correspond to γ-$Au_{60}Ge_{40}$.

These conclusions have obvious consequences for the interpretation of the MIT that occurs in this system. For such a 2 (or possibly 3) phase system it is more appropriate to apply percolation theory rather than the Anderson delocalization approach. A further consequence of the presence of regions of a Au:Ge alloy is that some Ge atoms will actually be contributing to the overall volume fraction having a relatively high conductivity (using the reasonable assumption that that the Au:Ge regions are of higher conductivity the a-Ge). Thus the MIT may be expected to occur at a lower gold concentration than it would for a truly homogeneous system.

9.5 Conclusion

Incorporation of Au into a-Ge leads to a local reordering of the TRN. Au atoms do not occupy substitutional or interstitial sites but form cluster-like regions of a Au:Ge alloy that is embedded in the persisting a-Ge TRN. At higher metal concentrations small clusters of Au are also formed. The crystalline phase of the alloy corresponds to γ-$Au_{60}Ge_{40}$. The a-Ge TRN persists throughout.

Although no drastic structural changes are apparent at the critical concentrations corresponding to the MIT reported by Dodson et al. [142] (x=0.12 for amorphous films and x=0.18 for microcrystalline samples), it is possible that the MIT in Dodson's flash evaporated samples does not occur at the same value as that in the sputtered samples reported on here. In this respect, it would have been useful to have performed electronic and optical studies on the sputtered films to determine the position of the MIT and the corresponding concentration at which the optical band-gap disappears. However, conclusions drawn from structural work on the a-Ge:Au system suggest that the conductivity of this extremely complex system may be best interpreted using percolation theory.

Chapter 10

Summary

10.1 Summary of Experimental Results

(a) a-Si:Ni:H

It is concluded that the a-Si:Ni:H samples prepared in this study contain two amorphous phases. One is a modified semiconducting a-Si:H network while the other is an amorphous alloy containing both Si and Ni atoms.

(b) a-Si:Sn:H

The structural study of the a-Si:Sn:H system has shown that the majority of the Sn atoms enter the a-Si:H TRN in a substitutional manner for compositions below 18at.% Sn.

The EXAFS investigation of both a-Si:H and a-Si:D films determined these samples to be structurally identical. Initial argon K-edge EXAFS indicated that any of

this gas incorporated into the semiconducting matrix occupies random sites.

(c) a-Ge:Au

The Ge:Au samples studied show a marked similarity to the a-Si:Ni:H system. A modified a-Ge matrix exists at all compositions investigated (0–37at.% Au) and the Au is incorporated into this matrix as regions of a Au:Ge alloy. However, these intermetallic regions are partially crystalline and, for Au concentrations above 21at.%, small metallic clusters also exist.

10.2 General Conclusions

The behaviour of the transition metal Ni or the near-noble metal Au on incorporation into an amorphous, semiconducting tetrahedral random network such as a-Si or a-Ge appears to be fundamentally different to the inclusion of the group IV metal Sn. Since the nature of the dopant atom incorporation has direct consequences for the electronic properties of the alloy material, it is clear from these results that a knowledge of the structure of a semiconducting:metal system is a necessary prerequisite for the successful interpretation of such properties. However, as outlined in Chapters 7 – 9, much work has been published under the assumption that the metal incorporation in such alloys is random (substitutional or interstitial), irrespective of its position in the periodic table. It is hoped that by identifying the way in which different impurity atoms are included in the semiconducting TRN, this work will help to further the understanding of the electronic properties of these and other such alloys. In particular,

the conclusion of a heterogeneous system for the two transition metal alloys studied indicates that the assumption of an Anderson-type MIT for such systems is not as soundly based as was previously thought and suggests that classical percolation theory may prove more applicable to the transition.

A more general point that has been highlighted during this work is the importance of sample preparation conditions on the resulting properties of thin-film alloys. In addition to varying deposition rates, which will influence the growth and structure of the films, samples prepared by some techniques (glow-discharge for instance) may include sizeable amounts of impurity elements, while vapour deposition is unable to incorporate reactive gases, such as hydrogen, in films. In the sputtering technique alone it is possible to significantly alter the physical and electronic properties of samples by variation of such parameters as sputtering gas pressure and substrate temperature, as well as those mentioned above. This underlines the need to perform any parallel studies only on samples made under identical conditions if a direct comparison is to be made between results.

The chemically specific nature of the EXAFS technique makes it a useful tool for the study of the local structure of amorphous semiconductor:metal alloys since the absorption edges can be investigated independently. This is especially important in samples with a low dopant concentration. However, this work has also verified the importance of the collection of standard sample data. In common with other microstructural probes, the return of *average* values of the system's parameters complicates the interpretation of results for complex systems such as Ge:Au and important bonding information may be obscured. In this respect, it is most advantageous to perform complementary structural studies such as powder X-ray diffraction, neutron scattering, infra-red absorption, nuclear magnetic resonance, Mössbauer and Raman

spectroscopy. Unfortunately, some of these techniques suffer form the disadvantage of requiring large quantities of powdered sample which would be difficult to prepare using the type of equipment employed in this work. Hence, a further advantage of using EXAFS for this type of study is its suitability to thin-films on substrates by virtue of the adaptability of its detection methods.

Another method that shows considerable promise for the structural investigation of thin-film samples is flat plate X-ray diffraction at grazing incidence. Recently, some of the samples prepared in this work were used to explore the potential of this new technique for studying the structure of amorphous thin-films. This work was carried out on beamline 9.1 at the SRS using an a-Si:Ni:H film deposited on c-Si and an a-Si:Sn:H sample on glass. Both films were 1–2μm thick. While the diffraction patterns showed clear trends as a function of the incident angle, it was not clear if there was any contribution from substrate scattering, or to what degree substrate curvature or surface roughness (*e.g.* pinholes) were affecting the data. Further analysis is in progress and future experiments are planned.

In addition to supporting structural studies, it would have been useful to have obtained more comprehensive electronic and optical results if a more detailed explanation of the processes involved in the conduction mechanism and any MIT were to be discussed. Due to differences that may be caused by errors in sample composition estimates, or in preparation conditions as previously mentioned, it is highly desirable that the entire study should be performed on identically prepared and characterized samples as far as is possible.

For the a-Si:Ni:H system, it is clear that the studies need to be extended to higher Ni concentrations to confirm whether or not a MIT exists in the 20–40at.% Ni region. It would also be interesting to observe the structural rearrangements in this range,

e.g. the concentration at which the a-Si TRN finally disappears and the possible aggregation and/or crystallization of the embedded a-Si:Ni clusters, for comparison with the a-Ge:Au and a-Ge:Mo [112] systems.

As well as more comprehensive photoelectronic studies and the possibility of increasing the concentration range for the a-Si:Sn:H samples, it is clear that a supporting technique, such as ^{119}Mössbauer spectroscopy, that can distinguish between the various bonding states of the Sn atoms could usefully be employed in a complementary study.

The complex structural nature of the a-Ge:Au samples indicates that more investigations are required on this system to clarify the structural picture. In addition to the parallel electronic results that could complement structural data, greater atomic-scale investigations are also necessary to define completely the intrinsic complexities of this system. In this respect, flat plate X-ray diffraction would be an extremely useful tool. Powder X-ray diffraction, performed on thin-film samples deposited on polypropylene and rolled into a tube, did not produce high quality spectra and it would be beneficial to perform high resolution X-ray diffraction on all samples. Keeping the samples below room temperature might have reduced or delayed any crystallization, but it would then have also been necessary to keep the samples cool during EXAFS measurements to avoid the possibility of kinetic reaction. (Although it may then have been the case that the samples remained wholly amorphous, and therefore structurally less complex, it is, of course, the room temperature properties of such systems that are sought for their device application). Further information on the bonding changes in Ge:Au could be obtained from X-ray absorption near edge structure (XANES) data, as the L_3 near edge spectra of 5d transition metals are dominated by a strong white line due to 2p→5d transitions. The integrated area of the white line feature should

be proportional to the number of holes in the 5d orbital *i.e.* the number of available final states. Since Au is an extremely electronegative metal, it tends to demand a charge transfer to the Au sites when alloyed in any way. Hence, any change in the number of holes caused by bond formation of the Au atoms should be indicated in the XANES spectra.

Finally, such extended and supported structural studies could also be applied to other important semiconductor:metal systems, such as a-Si:Au, which have not received the attention of direct structural measurement.

Bibliography

[1] Y. Hamakawa, editor. *Amorphous semiconductors:Technologies and devices.* (North-Holland, Amsterdam), 1982.

[2] S.R. Ovshinsky and D. Adler. Progress in the science and application of amorphous materials. *J. Non-Cryst. Sol.*, 90:229, 1987.

[3] S.R. Elliott. The structure of amorphous hydrogenated silicon and its alloys:a review. *Advances in Physics*, 38:1, 1989.

[4] W.E. Spear and P.G. LeComber. Substitutional doping of amorphous silicon. *Sol. State Commun.*, 17:1193, 1975.

[5] N.F. Mott. The basis of the electron theory of metals, with special reference to the transition metals. *Proc. Phys. Soc.*, 62A:416, 1949.

[6] P.W. Anderson. Absence of diffusion in certain random lattices. *Phys. Rev.*, 109:1492, 1958.

[7] N.F. Mott. *Metal-insulator transitions.* (Taylor and Francis, New York), 1974.

[8] L.R. Friedman and D.P. Tunstall, editors. *The metal non-metal transition in disordered systems.* (SUSSP, Edinburgh), 1978.

[9] H. Fritzsche and D. Adler, editors. *Localization and metal-insulator transitions.* (Plenum Press, New York), 1985.

[10] E. Abrahams, P.W. Anderson, D.C. Licciardello, and T.V. Ramakrishnan. Scaling theory of localization:absence of quantum diffusion in two dimensions. *Phys. Rev. Lett.*, 42:673, 1979.

[11] W.L. McMillan. Scaling theory of the metal-insulator transition in amorphous materials. *Phys. Rev. B*, 24:2739, 1981.

[12] T. Shimizu, M. Kumeda, I. Watanabe, and Y. Noumi. ESR of transition metals in a-Si. *J. Non-Cryst. Sol.*, 35/36:645, 1980.

[13] P.K. Shufflebotham, H.C. Card, and A. Thanailakis. A review of amorphous silicon alloys. *J. Non-Cryst. Sol.*, 92:183, 1987.

[14] J. Sonntag. Disordered electronic systems:concentration dependence of the dc conductivity in amorphous transition-metal-metalloid alloys (metallic regime). *Phys. Rev. B*, 40:3661, 1989.

[15] K. Morigaki. Metal-insulator transitions in amorphous semiconductors. *Phil. Mag. B*, 42:979, 1980.

[16] R. Zallen and H. Scher. Percolation on a continuum and the localization-delocalization transition in amorphous semiconductors. *Phys. Rev. B*, 4:4471, 1971.

[17] W.H. Zachariasen. The atomic arrangement in glass. *J. Am. Chem. Soc.*, 54:3841, 1932.

[18] R. Zallen. *The Physics of Amorphous Solids.* (Willy-Interscience, New York), 1983.

[19] N.E. Cusack. *The Physics of Structurally Disordered Matter.* (IOP Publishing, Bristol), 1987.

[20] J.D. Bernal. The geometry of the structure of liquids. In T.J. Hughel, editor, *Liquids: Structure, Properties, Solid Interactions*, (Elsevier, Amsterdam), 1965.

[21] P.J. Flory. *Principles of Polymer Chemistry.* (Cornell University Press, Ithaca, New York), 1953.

[22] S.R. Elliott. *Physics of Amorphous Materials.* (Longman, London), 1983.

[23] R.V. Kruzelecky, D. Racansky, S. Zukotynski, Y.C. Koo, and J.M. Perz. The effect of preparation conditions on the morphology of low-temperature silicon films. *J. Non-Cryst. Sol.*, 104:237, 1988.

[24] J. L. Vossen and W. Kern, editors. *Thin Film Processes.* (Academic Press, New York), 1978.

[25] B.T. Kolomiets. Glassy semiconductors. In *Proceedings of the International Conference on Semiconductor Physics*, Czechoslovak Acadamy of Sciences, 1960.

[26] D. Weaire and M.F. Thorpe. Electronic properties of an amorphous solid. *Phys. Rev. B*, 4:2508, 1971.

[27] N.F. Mott and E.A. Davis. *Electronic processes in non-crystalline materials.* (Clarendon Press, Oxford), 1971.

[28] M.H. Cohen, H. Fritzsche, and S.R. Ovshinsky. Simple band model for amorphous semiconducting alloys. *Phys. Rev. Lett.*, 22:1065, 1969.

[29] E.A. Davis and N.F. Mott. Conductivity in non-crystalline systems. *Phil. Mag.*, 22:903, 1970.

[30] N. Piggins. *A study of the optical and electronic properties of amorphous silicon nitride.* PhD thesis, University of Leicester, 1988.

[31] P. Nagels. *Amorphous Semiconductors*, chapter 5. Volume 36 of *Topics in Applied Physics*, (Springer-Verlag, Berlin), 1979.

[32] N.F. Mott. Conduction in glasses containing transition metal ions. *J. Non-Cryst. Sol.*, 1:1, 1968.

[33] S. Kirkpatrick. Percolation and conduction. *Reviews of Modern Physics*, 45:574, 1973.

[34] H. Scher and R. Zallen. Critical density in percolation processes. *J. Chem. Phys.*, 53:3759, 1970.

[35] M.H. Cohen, J. Jortner, and I. Webman. Electrical transport and optical properties of inhomogeneous media. In J.C. Garland and D.B. Tanners, editors, *AIP Conference Proceedings Number 40*, page 63, American Institute of Physics, 1978.

[36] K. L. Chopra and I. Kaur. *Thin Film Device Applications.* (Plenum Press, New York), 1983.

[37] J. Macneil. *The electrical and optical properties of amorphous films of Si:Au and Si:Cu.* PhD thesis, University of Leicester, 1985.

[38] H. Fricke. The K-characteristic absorption frequencies for the chemical elements magnesium to chromium. *Phys. Rev.*, 16:202, 1920.

[39] G. Hertz. Über die absorptionsgrenzen in der L-series. *Z .Phys.*, 3:19, 1920.

[40] B.B. Ray. Merhfachabsorption und sekundäre K-absorptionsgrenze im röntgengebiet. *Z. Phys.*, 55:119, 1929.

[41] B. Kievet and G.A. Lindsay. Fine structure in the X-ray absorption spectra of the K series elements calcium to gallium. *Phys. Rev.*, 36:648, 1930.

[42] R. de L. Kronig. Zur theorie der feinstruktur in den röntgenabsorptionsspektren. *Z. Phys.*, 70:317, 1931.

[43] R. de L. Kronig. Zur theorie der feinstruktur in den röntgenabsorptionsspektren iii. *Z. Phys.*, 75:468, 1932.

[44] D.E. Sayers, E.A. Stern, and F.W. Lytle. New technique for investigating noncrystalline structures: Fourier analysis of the extended X-ray absorption fine structure. *Phys. Rev. Lett.*, 27:1204, 1971.

[45] B.M. Kincaid and P. Eisenberger. Synchrotron radiation studies of the K-edge photoabsorption spectra of Kr, Br_2 and $GeCl_4$. *Phys. Rev. Lett.*, 34:1361, 1975.

[46] S.H. Hunter. Chapter 11. In B.K. Teo and D.C. Joy, editors, *EXAFS Spectroscopy*, page 163, (Plenum Press, New York), 1981.

[47] R. Manaila and D. Macovei. EXAFS in amorphous materials. *J. Non-Cryst. Sol.*, 90:383, 1987.

[48] W. Blau, E. Zschech, and J. Bergmann. EXAFS investigation of SRO in amorphous solids. *Nuclear Instruments and Methods in Physics Research A*, 261:166, 1987.

[49] E.D. Crozier, J.J. Rehr, and R. Ingalls. Chapter 9. In D.C. Koningsberger and R. Prins, editors, *X-ray Absorption*, page 373, (Wiley-Interscience, New York), 1988.

[50] G.S. Cargill III. Capabilities and limitations of EXAFS for amorphous alloys. *J. Non-Cryst. Sol.*, 61/62:261, 1984.

[51] S.J. Gurman. Review: EXAFS studies in materials science. *J. Mat. Sci.*, 17:1541, 1982.

[52] G.N. Greaves. X-ray absorption spectroscopy. 1988. SERC Daresbury Laboratory report DL/SCI/P616E.

[53] E.A. Stern. Theory of extended X-ray absorption fine structure. *Phys. Rev. B*, 10:3027, 1974.

[54] S.J. Gurman and J.B. Pendry. Extraction of crystal parameters from EXAFS spectra. *Sol. State Commun.*, 20:287, 1976.

[55] Keski-Rahkomen and M.O. Krause. Volume 14. In *Atomic Data Nucl. Data Tables*, page 140, 1974.

[56] T.A. Carlson. *Photoelectron and Auger Spectroscopy.* (Plenum Press, New York), 1975.

[57] D. Lu and J.J. Rehr. Inelastic processes in extended X-ray absorption fine structure. *Phys. Rev. B*, 37:6126, 1988.

[58] P.J. Durham, J.B. Pendry, and C.H. Hodges. Calculation of X-ray absorption near edge structure, XANES. *Comput. Phys. Commun.*, 25:193, 1982.

[59] P.J. Durham. Chapter 2. In D.C. Koningsberger and R. Prins, editors, *X-ray Absorption*, page 53, (Wiley-Interscience, New York), 1988.

[60] P.A. Lee and J.B. Pendry. Theory of extended X-ray absorption fine structure. *Phys. Rev. B*, 11:2795, 1975.

[61] C.A. Ashley and S. Doniach. Theory of extended X-ray absorption edge fine structure (EXAFS) in crystalline solids. *Phys. Rev. B*, 11:1279, 1975.

[62] S.J. Gurman. Structural information in X-ray absorption fine structure. In S.S. Hasnain, editor, *Biophysics and Synchrotron Radiation*, (Ellis-Horwood, Chichester), 1990. To be published.

[63] J.J. Rehr, R.C. Albers, C.R. Natoli, and E.A. Stern. Spherical wave corrections in XAFS. *J. Physique Colloq. C8*, 47:31, 1986.

[64] C.R. Natoli and M. Benfatto. A unifying scheme of interpretation of X-ray absorption spectra based on the multiple scattering theory. *J. Physique Colloq. C8*, 47:11, 1986.

[65] A.G. McKale, B.W. Veal, A.P. Paulikas, S.K. Chan, and G.S. Knapp. Improved ab initio calculations of amplitude and phase functions for extended X-ray absorption fine structure spectroscopy. *J. Am. Chem. Soc.*, 110:3763, 1988.

[66] S.J. Gurman. The small-atom approximation in EXAFS and surface EXAFS. *J. Phys. C*, 21:3699, 1988.

[67] N. Binsted, S.J. Gurman, and J.W. Campbell. Excurv88 program. 1988. SERC Daresbury Laboratory.

[68] S.J. Gurman, N. Binsted, and I.Ross. A rapid, exact curved-wave theory for EXAFS calculations. *J. Phys. C.*, 17:143, 1984.

[69] T.M. Hayes and J.B. Boyce. Extended X-ray absorption fine structure spectroscopy. *Sol. State Phys.*, 37:173, 1983.

[70] B.K. Teo and P.A. Lee. Ab initio calculations of amplitude and phase functions for extended X-ray absorption fine structure spectroscopy. *J. Am. Chem. Soc.*, 101:2815, 1979.

[71] C. Morrel, J.T.M. Baines, J.C. Campbell, G.P. Diakun, B.R. Dobson, G.N. Greaves, and S.S. Hasnain, editors. *Daresbury EXAFS users' manual*, 1988.

[72] R.W. Joyner, K.J. Martin, and P. Meehan. Some applications of statistical tests in analysis of EXAFS and SEXAFS data. *J. Phys. C*, 20:4005, 1987.

[73] F.R. Elder, A.M. Gurewitsch, R.V. Langmuir, and H.L. Pollock. A 70-MeV Synchrotron. *J. Appl. Phys.*, 18:810, 1947.

[74] C.D. Garner and S.S. Hasnain. 1981. EXAFS for inorganic systems. DL/SCI/R17.

[75] S.M. Heald. Chapter 3. In D.C. Koningsberger and R. Prins, editors, *X-ray Absorption*, page 87, (Wiley-Interscience, New York), 1988.

[76] P.A. Lee, P.H. Citrin, P. Eisenberger, and B.M. Kincaid. Extended X-ray Absorption Fine Structure: Its strengths and limitations as a structural tool. *Reviews of Modern Physics*, 53(4):769, 1981.

[77] W.J. Veigele. Photon cross sections from 0.1keV to1MeV for elements z=1 to z=94. In *Atomic Data Tables Volume 5*, page 51, 1973.

[78] D.C. Koningsberger and R. Prins, editors. *X-ray Absorption.* (Wiley-Interscience, New York), 1988.

[79] J. Jaklevic, J.A. Kirby, M.P. Klein, and A.S. Robertson. Fluorescence detection EXAFS: Sensitivity enhancement for dilute species and thin films. *Sol. State Commun.*, 23:679, 1977.

[80] S.S. Hasnain, P.D. Quinn, G.P. Diakun, E.M. Wardell, and C.D. Garner. Fluorescence EXAFS at the SRS: Increased sensitivity for dilute samples. *J. Phys. E: Sci. Instrum.*, 17:40, 1984.

[81] K. Yamada, Y. Endoh, Y. Ishikawa, and N. Watanabe. Neutron diffraction studies of atomic structures of amorphous Fe-Ge and Ni-Ge. *J. Phys. Soc. Jap.*, 48:922, 1980.

[82] H. Oyanagi, K. Tsuji, S. Hosoya, S. Minomura, and T. Fukamachi. EXAFS study on the structure of amorphous Ge-Ni alloys. *J. Non-Cryst. Sol.*, 35/36:555, 1980.

[83] M. M. Collver. Metastable impurity bands: Conduction in $Si_{1-x}Co_x$ and $Si_{1-x}Ni_x$ alloy films. *Sol. State Commun.*, 23:333, 1977.

[84] T. Shimizu, M. Kumeda, I. Watanabe, and Y. Noumi. Effects of transition metal additives on amorphous silicon. *Phil. Mag. B*, 44:159, 1981.

[85] N.A. Rogachev, V. Šmíd, J.J. Mareš, and J. Krištofik. Amorphous nickel slilicides prepared by magnetron co-sputtering. *J. Non-Cryst. Sol.*, 97/98:955, 1987.

[86] E.R. Weber. Diffusion of Ni in Si. 1987. EMIS Datareview series RN=17858.

[87] R.D. Thompson, D. Gupta, and K.N. Tu. Low-temperature diffusion and solubility of Ni in p-doped Czochralski-grown Si. *Phys. Rev. B*, 33:2636, 1985.

[88] M.I. Manssor and E.A. Davis. 1988. Private communication.

[89] E.A. Davis, S.C. Bayliss, R. Asal, and M. Manssor. Free-carrier behaviour in a-$Si_{1-y}Ni_y$:H. 1990. To be published in the proceedings of ICALS, J. Non-Cryst. Sol.

[90] A.V. Dvurechenskii, V.A. Dravin, I.A. Ryazantsev, A.Kh. Antonenko, and I.G. Landochkin. Transport phenomena in amorphous silicon doped by ion implantation of 3d metals. *Phys. Stat. Sol. A*, 95:635, 1986.

[91] H.S. Derbyshire. *Preparation and properties of amorphous cadmium-silicon-arsenic thin films.* PhD thesis, University of Leicester, 1987.

[92] B.A. Weinstein and G.J. Piermarini. Raman scattering and phonon dispersion in Si and GaP at very high pressure. *Phys. Rev. B*, 12:1172, 1975.

[93] R. Weil, I. Abdulhalim, R. Beserman, M. Janai, and B. Pratt. Comparison of strain in glow-discharge a-Si:F and a-Si:H. *J. Non-Cryst. Sol.*, 77/78:261, 1985.

[94] R. Tsu, J.G. Hernandez, and F.H. Pollak. Determination of energy barrier for structural relaxation in a-Si and a-Ge by Raman scattering. *J. Non-Cryst. Sol*, 66:109, 1984.

[95] W.B. Pearson. *Handbook of lattice spacings and structures of metals and alloys.* (Pergamon, New York), 1958.

[96] W.B. Pearson. *The crystal chemistry and physics of metals and alloys.* (Wiley, New York), 1972.

[97] K. Toman. The structure of NiSi. *Acta Cryst.*, 4:462, 1951.

[98] K. Toman. The structure of Ni_2Si. *Acta Cryst.*, 5:329, 1952.

[99] R.W.G. Wyckoff. *Crystal structures.* Volume 1, (Wiley Interscience, New York), 1963.

[100] E.G. Rochow. *The chemistry of silicon.* (Pergamon press), 1973.

[101] S.C. Bayliss. 1988. Private communication.

[102] J.D. Joannopoulas and G. Lucovsky, editors. *The physics of hydrogenated amorphous silicon 1.* Volume 55 of *Topics in Applied Physics*, (Springer-Verlag, Berlin), 1984.

[103] P.J. Grunthaner and F.J. Grunthaner. Metal/silicon interface formation: The Ni/Si and Pd/Si systems. *J. Vac. Sci. Technol.*, 19:649, 1981.

[104] J.G. Clabes. LEED investigations of the interaction of Pd and Ni with different Si(111) surfaces. *Surface Science*, 145:87, 1984.

[105] R.T. Tung, J.M. Gibson, and J.M. Poate. Formation of ultrathin single-crystal silicide films on Si: Surface and interfacial stabilization of Si-$NiSi_2$ epitaxial structures. *Phys. Rev. Lett.*, 50:429, 1983.

[106] R.B. Jackman. Structure of the Ni/Si interface. 1987. EMIS Datareview series RN=16109.

[107] F. Comin, J.E. Rowe, and P.H. Citrin. Structure and nucleation mechanism of nickel silicide on Si(111) derived from surface extended X-ray absorption fine structure. *Phys. Rev. Lett.*, 51:2402, 1983.

[108] K.N. Tu. Selective growth of metal-rich silicides of near-noble metals. *Appl. Phys. Lett.*, 27:221, 1975.

[109] M.O. Aboelfotoh, H.M. Tawancy, and F.M. d'Heurle. Transmission electron microscope study of the formation of Ni_2Si and NiSi on amorphous silicon. *Appl. Phys. Lett.*, 50:1453, 1987.

[110] R.E. Harper. Resistivity of $NiSi_2$. 1987. EMIS Datareview series RN=15714.

[111] L. Koudelka, N. Lustig, and J.S. Lannin. Raman scattering of Ni and Cr amorphous disilicides. *Sol. State Commun.*, 63:163, 1987.

[112] J.B. Kortright and A. Bienenstock. X-ray structural study of amorphous Mo-Ge films. *Phys. Rev. B*, 37:2979, 1988.

[113] K.Tamura, J. Fukushima, H. Endo, S. Minomura, O. Shimomura, and K. Asaumi. Effects of pressure on the electronic properties of amorphous Ge and its alloys. In *Proceedings of the second international conference on the properties of liquid metals, Tokyo, 1972*, page 301, (Taylor and Francis, London), 1973.

[114] B. von Roedern, D.K. Paul, J. Blake, R.W. Collins, G. Moddel, and W. Paul. Optical absorption, photoconductivity and photoluminescence of glow-discharge amorphous $Si_{1-x}Ge_x$ alloys. *Phys. Rev. B*, 25:7678, 1982.

[115] S.Z. Weisz, M. Gomez, J.A. Muir, O. Resto, R. Perez, Y. Goldstein, and B. Abeles. Reactively sputtered a-Si_xGe_{1-x}:H alloys with compositional gradient in plane of film. *Appl. Phys. Lett.*, 44:634, 1984.

[116] C. Verié, J.F. Rochette, and J.P. Rebouillat. New amorphous alloy semiconductors: a-$Si_{1-x}Sn_x$. *J. de Physique Colloq. 4*, 42(10):667, 1981.

[117] A.H. Mahan, D.L. Williamson, and A. Madan. Properties of amorphous silicon tin alloys produced using the radio frequency glow discharge technique. *Appl. Phys. Lett.*, 44:220, 1984.

[118] H. Itozaki, N. Fujita, T. Igarashi, and H. Hitotsuyanagi. Amorphous $Si_{1-x}Sn_x$:H by sputter assisted CVD. *J. Non-Cryst. Sol.*, 59/60:589, 1983.

[119] D.L. Williamson, R.C. Kerns, and S.K. Deb. Properties of amorphous hydrogenated silicon-tin alloys prepared by radio frequency sputtering. *J. Appl. Phys.*, 55:2816, 1984.

[120] B. von Roedern, A.H. Mahan, R. Könenkamp, D.L. Williamson, A. Sanchez, and A. Madan. Material properties of glow-discharge a-Si:Sn:H alloys. *J. Non-Cryst. Sol.*, 66:13, 1984.

[121] G.N. Parsons, J.W. Cook, Jr., G. Lucovsky, S.Y. Lin, and M.J. Mantini. Deposition of a-Si:Sn:H alloy films by reactive magnetron sputtering from separate Si and Sn targets. *J. Vac. Sci. Technol. A*, 4:470, 1986.

[122] A. Mohamedi, M.L. Thèye, M. Vergnat, G. Marchal, and M. Piecuch. Optical studies of bonding in coevaporated amorphous silicon-tin alloys. *Phys. Rev. B*, 39:3711, 1989.

[123] M. Vergnat, M. Piecuch, G. Marchal, and M. Gerl. Structure and short-range order of vapour-deposited $Si_{1-x}Sn_x$ amorphous alloys. *Phil. Mag. B*, 51:327, 1985.

[124] D.L. Williamson and S.K. Deb. Mössbauer spectroscopy of amorphous silicon-tin-hydrogen alloys. *J. Appl. Phys.*, 54:2588, 1983.

[125] Zhang Fangqing, He Deyan, and Chen Guanghua. Influence of substrate temperature on the structure of sputtered a-$Si_{1-x}Sn_x$:H alloys. *Chin. Phys. Lett.*, 3:245, 1986.

[126] A. Morimoto, T. Kataoka, and T. Shimizu. Annealing studies on hydrogenated amorphous silicon-tin films. *Jap. J. Appl. Phys.*, 24:1122, 1985.

[127] D. Girginoudi, N. Georgoulas, and A. Thanailakis. Optical and electronic properties of sputtered hydrogenated amorphous silicon-tin alloys. *J. Appl. Phys.*, 66:354, 1989.

[128] D.A. Anderson and W.E. Spear. Photoconductivity and recombination in doped amorphous silicon. *Phil. Mag.*, 36:695, 1977.

[129] M. Vergnat, G. Marchal, and M. Piecuch. Preparation of hydrogenated amorphous silicon tin alloys. *Revue Phys. Appl.*, 22:1803, 1987.

[130] S.Y. Lin, G. Lucovsky, S. Guha, and J.S. Payson. Electronic structure of divalent effects in tetrahedrally bonded amorphous materials. *Mat. Res. Soc. Symp. Proc.*, 70:107, 1986.

[131] W. Paul, D.K. Paul, B. von Roedern, J. Blake, and S. Oguz. Preferential attachment of H in amorphous hydrogenated binary semiconductors and consequent inferior reduction of pseudogap state density. *Phys. Rev. Lett.*, 46:1016, 1981.

[132] R. Bellissent, A. Chenevas-Paule, P. Chieux, and A. Menelle. A-Si:H short range order by neutron scattering. *J. Non-Cryst. Sol.*, 77/78:213, 1985.

[133] M.H. Brodsky, M. Cardona, and J.J. Cuomo. Infrared and Raman spectra of the silicon-hydrogen bonds in amorphous silicon prepared by glow discharge and sputtering. *Phys. Rev. B*, 16:3556, 1977.

[134] N. Maloufi, A. Audouard, M. Piecuch, and G. Marchal. DC conductivity mechanisms in amorphous group-IV semiconductors. *Phys. Rev. Lett.*, 56:2307, 1986.

[135] N. Maloufi, A. Audouard, M. Piecuch, M. Vergnat, G. Marchal, and M. Gerl. Experimental study of the dc conductivity mechanisms in amorphous Si_xSn_{1-x} alloys. *Phys. Rev. B*, 37:8867, 1988.

[136] G. Lucovsky, J. Yang, S.S. Chao, J.E. Tyler, and W. Czubatyj. Vibrational properties of deuterated a-Si alloys. *J. Non-Cryst. Sol.*, 59/60:609, 1983.

[137] W. Beyer. Hydrogen incorporation in amorphous silicon and processes of its release. In D. Adler and H. Fritzsche, editors, *Tetrahedrally-bonded amorphous semiconductors*, page 129, (Plenum Press, New York), 1985.

[138] G. Weyer, S. Damgaard, J.W. Petersen, and J. Heinemeier. Comparison of impurity defect structures formed by ion implantations in amorphous and crystalline silicon. *Nucl. Inst. and Methods*, 199:441, 1982.

[139] D.H. Rich, T. Miller, A. Samsavar, H.F. Lin, and T.C. Chiang. Adsorption and growth of Sn on Si(100) from synchrotron photoemission studies. *Phys. Rev. B*, 37:10221, 1988.

[140] T.R. Anantharaman, Huey-Lin Luo, and W. Klement, Jr. Nonequilibrium structures in gold-germanium alloys. *Transactions of the metallurgical society of AIME*, 233:2014, 1965.

[141] M.L. Theye, N. Nguyen Van, and S. Fisson. Validity of the free-electron model for Ag-Ge and Au-Ge amorphous metallic alloys. *Phil. Mag. B*, 47:31, 1983.

[142] B.W. Dodson, W.L. McMillan, and J.M. Mochel. Metal-insulator transition in disordered germanium-gold alloys. *Phys. Rev. Lett.*, 46:46, 1981.

[143] W.L. McMillan and J. Mochel. Electron tunneling experiments on amorphous $Ge_{1-x}Au_x$. *Phys. Rev. Lett.*, 46:556, 1981.

[144] M. Osofsky, H. Tardy, M. LaMadrid, and J.M. Mochel. DC conductivity of strong and weak electron spin-orbit scattering materials near the metal-insulator transition. *Phys. Rev. B*, 32:2101, 1985.

[145] J.J. Hauser. Localized and nonlocalized impurity states in amorphous germanium. *Sol. State Commun.*, 13:1451, 1973.

[146] E.R. Weber. Diffusion of Au in Si. 1988. EMIS Datareview series RN=17886.

[147] Hou Jian-guo and Wu Zi-qin. Temperature dependence of fractal formation in ion-implanted a-Ge/Au bilayer thin films. *Phys. Rev. B*, 40:1008, 1989.

[148] Zheng Xin and Wu Zi-Qin. Fractal crystallization in a-Ge/Au/a-Ge sandwich after annealing. *Sol. State Commun.*, 70:587, 1989.

[149] Zheng Xin and Wu Zi-Qin. Fractal patterns in annealed sandwich Au/a-Ge/Au. *Sol. State Commun.*, 70:991, 1989.

[150] J.J. Hauser. Electrical conductivity in amorphous Si(O or H)-Au films. *Sol. State Commun.*, 34:321, 1980.

[151] J. Mcneil and E.A. Davis. Study of the metal-insulator transition in amorphous Si:Au:H alloys. *J. Non-Cryst. Sol.*, 59/60:145, 1983.

[152] N. Nishida, T. Furubayashi, M. Yamaguchi, K. Morigaki, and H. Ishimoto. Metal-insulator transition in the amorphous $Si_{1-x}Au_x$ system with a strong spin-orbit interaction. *Sol. State Electronics*, 28:81, 1985.

[153] N. Kishimoto and K. Morigaki. Metal-nonmetal transition in amorphous Si-Au system at low temperatures: Measurement of electrical conductivity and thermoelectric power. *J. Phys. Soc. Jap.*, 46:846, 1979.

[154] E. Huber and M. von Allmen. Optical properties of laser-melt-quenched Au-Si alloys. *Phys. Rev. B*, 28:2979, 1983.

[155] N. Kishimoto and K. Morigaki. Optical absorption and infrared photoconductivity in amorphous Si-Au system. *J. Phys. Soc. Jap.*, 46:497, 1979.

[156] E. Hauser, J. Tauc, and J.J. Hauser. Infrared absorption spectra of amorphous silicon with gold. *Sol. State Commun.*, 32:385, 1979.

[157] G. Marchal, Ph. Mangin, and Chr. Janot. Crystallization of Au_xSi_{1-x} amorphous alloys. *Phil. Mag. B*, 42:81, 1980.

[158] Ph. Mangin, G. Marchal, C. Mourey, and Chr. Janot. Physical studies of Au_xSi_{1-x} amorphous alloys. *Phys. Rev. B*, 21:3047, 1980.

[159] J.J. Hauser and J. Tauc. Electrical properties of binary amorphous alloys. *Phys. Rev. B*, 17:3371, 1978.

[160] G. Bushnell-Wye. 1988. Private communication.

[161] K. O'Reilly. 1988. Private communication.

Appendix

Publications resulting from this work:

An investigation of the structure of amorphous Si_{1-x}:Ni_x through the metal–insulator transition.
A.M. Edwards, M.C. Fairbanks, A. Singh, R.J. Newport and S.J. Gurman.
Proceedings of the 5th International Conference on X-Ray Absorption Fine Structure, Seattle,
August 1988.
Physica B 158 600 - 601 (1989).

Structural studies of amorphous Si:Ni:H.
A.M. Edwards, M.C. Fairbanks, R.J. Newport, S.J. Gurman and E.A. Davis.
Journal of Non-Crystalline Solids, in press, Nov 1989.

Structural comparison of amorphous Si:H and Si:D.
A.M. Edwards, M.C. Fairbanks, R.J. Newport and S.J. Gurman.
Accepted for publication by Solid State Communications, Sept 1989.

Structural studies of amorphous Ge:Au alloys.
A.M. Edwards, M.C. Fairbanks and R.J. Newport.
Accepted for publication by Phil. Mag., Nov 1989.

Structural studies of amorphous semiconductor-metal alloys.
A.M. Edwards, M.C. Fairbanks, R.J. Newport and S.J. Gurman.
Proceedings of the 11th International Vacuum Congress and 7th International Conference on Solid Surfaces, Köln,
September 1989.
To be published in Vacuum.

The structure of a-$Si_{1-x}Sn_x$:H thin-films.
A.M. Edwards, M.C. Fairbanks and R.J. Newport. In preparation, Nov 1989.

Other publications:

The structure of Ce-Si-O amorphous thin films.
A. Singh, A.M. Edwards, S.J. Gurman, E.A. Davis and M.C. Fairbanks.
Proceedings of the 5th International Conference on X-Ray Absorption Fine Structure, Seattle,
August 1988.
Physica B 158 533 - 534 (1989).

The ionisity and structure of amorphous Si:N:H.
S.C. Bayliss, S.J. Gurman, A.M. Edwards and E.A. Davis.
In preparation, Nov 1989.